Contributions of Glacial Isostatic Adjustment to the Earth's Static Gravity Field and Horizontal Crustal Motions

Reusen, J.M.

DOI
10.4233/uuid:9e0a6a89-97d9-4c75-8b41-518649a18770

Publication date
2025

Document Version
Final published version

Citation (APA)
Reusen, J. M. (2025). *Contributions of Glacial Isostatic Adjustment to the Earth's Static Gravity Field and Horizontal Crustal Motions*. [Dissertation (TU Delft), Delft University of Technology]. https://doi.org/10.4233/uuid:9e0a6a89-97d9-4c75-8b41-518649a18770

Contributions of Glacial Isostatic Adjustment to the Earth's Static Gravity Field and Horizontal Crustal Motions

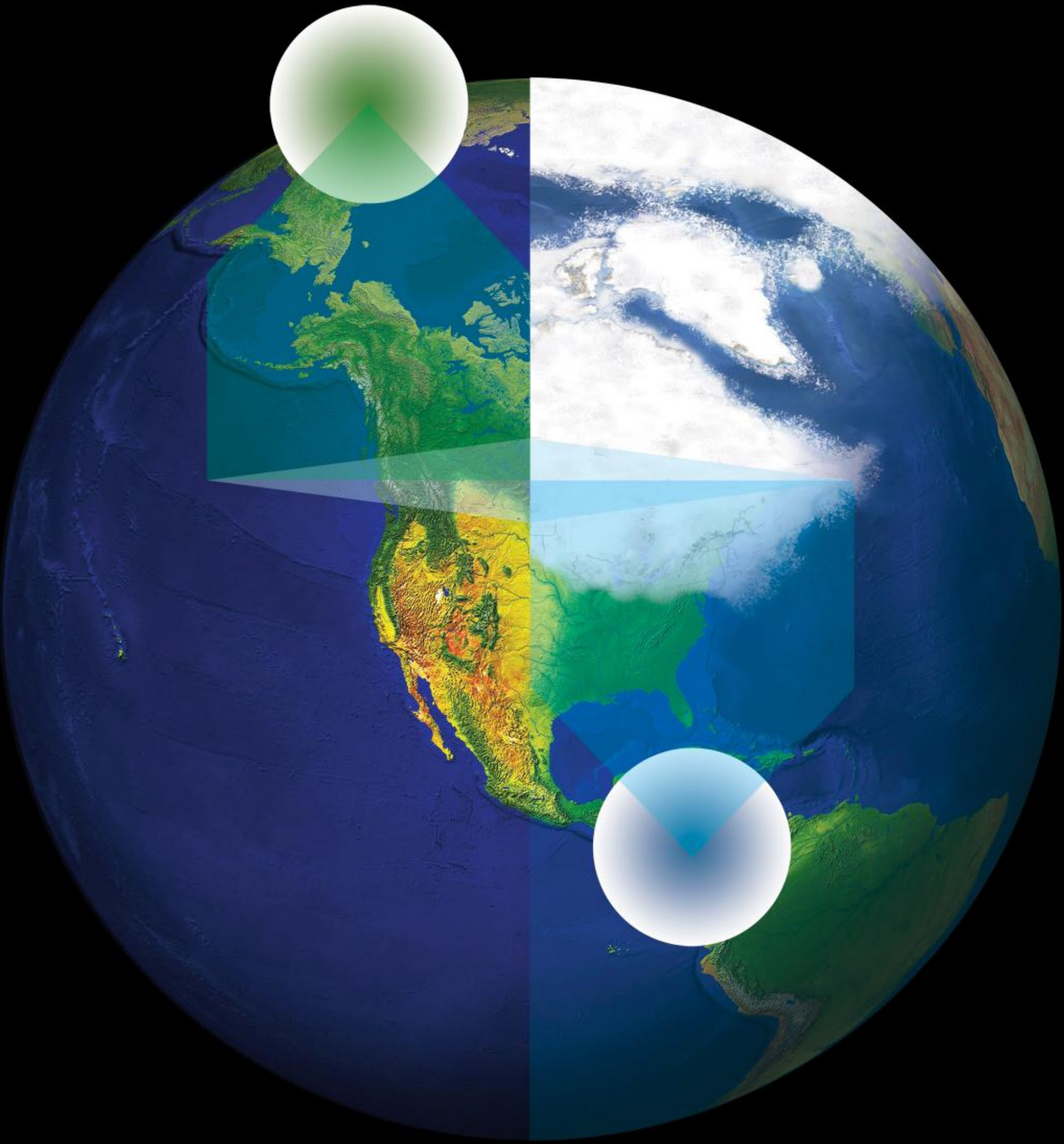

Jesse Reusen

CONTRIBUTIONS OF GLACIAL ISOSTATIC ADJUSTMENT TO THE EARTH'S STATIC GRAVITY FIELD AND HORIZONTAL CRUSTAL MOTIONS

CONTRIBUTIONS OF GLACIAL ISOSTATIC ADJUSTMENT TO THE EARTH'S STATIC GRAVITY FIELD AND HORIZONTAL CRUSTAL MOTIONS

Proefschrift

ter verkrijging van de graad van doctor
aan de Technische Universiteit Delft,
op gezag van de Rector Magnificus Prof. dr. ir. T.H.J.J. van der Hagen,
voorzitter van het College voor Promoties,
in het openbaar te verdedigen op

maandag 1 December 2025 om 15:00 uur

door

Jesse Milan REUSEN

Master of Science in Climate Physics,
Utrecht University, Nederland,

geboren te Arnhem, Nederland.

Dit proefschrift is goedgekeurd door de promotoren.

Samenstelling promotiecommissie:

Rector Magnificus,	voorzitter
Prof. dr. L.L.A. Vermeersen,	Technische Universiteit Delft, promotor
Dr. ir. W. van der Wal,	Technische Universiteit Delft, promotor
Dr. ir. B.C. Root,	Technische Universiteit Delft, copromotor
Onafhankelijke leden:	
Prof. dr. ir. R.C. Alderliesten,	Technische Universiteit Delft
Dr. R.E.M. Riva,	Technische Universiteit Delft
Dr. R.M.A. Govers,	Universiteit Utrecht
Prof. dr. J.T. Freymueller,	Michigan State University, USA
Prof. dr. ir. P.N.A.M. Visser,	Technische Universiteit Delft, reservelid

This publication was financially supported by the User Support Programme Space Research, a program of the Netherlands Organization for Scientific Research, under project number ALW.GO.2017.035.

The work has been performed in the framework of the project "3D Earth - A Dynamic Living Planet" funded by ESA as a Support to Science Element (STSE).

Keywords: Glacial Isostatic Adjustment, North America, static gravity, horizontal motion, compressibility

Printed by: ProefschriftMaken

Front & Back: Jan Sterenborg

ISBN 978-94-6534-014-2

Kindness begins with the understanding that we all struggle.
Charles Glassman

CONTENTS

SUMMARY

In the past, the Earth has been subject to various ice sheet growth and melt events. The ice exerts a pressure on the Earth's surface, depressing the ground below it. Whenever the ice melts, the Earth responds by raising its surface level again. This process is called postglacial rebound. Glacial Isostatic Adjustment (GIA) is considered to be a broader and more general term, namely the solid Earth response to land ice and surface water redistribution following continental ice growth or melt, which thus includes postglacial rebound.

Today, uplift of up to 13 mm a^{-1} is recorded around the Hudson Bay area in North America, due to the last ice sheets that have melted roughly between eighteen and six thousand years ago. Even higher uplift rates of 30 mm a^{-1} have been recorded in Southeast Alaska as a response to ice melt that only started 250 years ago. Part of the reason why these uplift rates differ is due to the underlying mantle viscosity. Mantle viscosity determines how fast material in the Earth's mantle is allowed to flow. A high mantle viscosity implies a mantle in which flow is slow, and a low mantle viscosity implies a weak mantle in which flow occurs easily. The viscosity of the mantle below Hudson Bay is expected to be around the global average value of 10^{21} Pa s, while the mantle viscosity in Southeast Alaska is expected to be a few orders of magnitude lower. GIA research is performed to infer structural parameters such as its mantle viscosity. Moreover, with more knowledge of GIA we are able to more accurately correct measurements for the effect of GIA. The goal of this thesis is to improve the numerical model setups, contributing to these two goals.

In the static gravity field, measured by satellites, GIA is observed as negative anomalies in previously glaciated regions where rebound of the land is not complete yet. At these locations, the surface of the Earth is lower than its equilibrium height resulting in a local mass deficit responsible for a negative anomaly in the gravity field. However, it is difficult to attribute an observed negative anomaly directly to GIA, because satellites measure the aggregate of dynamic processes and density inhomogeneities of all layers on Earth.

A negative gravity anomaly of about 50 mGal is observed over Hudson Bay. The location of this anomaly bears resemblance to the region covered by the Laurentide Ice sheet roughly 26 thousand years ago, when the Laurentide ice sheet extent was at its maximum. Some studies suggested a negligible contribution of GIA to this gravity anomaly, others suggested that more than half of the observed gravity anomaly can be explained by GIA. However, these studies computed the gravity field by a linear addition of results from models for the Crust-Lithosphere-Asthenosphere (CLA), GIA, and mantle convection. In Chapter 3, I combine models for CLA, GIA, and mantle convection by adding the forces of GIA and mantle convection to the force balance of the CLA model. Using this integrated approach, I find that at least 60% of the observed anomaly can be attributed to

GIA. Such a large contribution of GIA requires a lower mantle viscosity of more than 10^{22} Pa s, higher than found by several earlier studies. Such a high value for the lower mantle viscosity implies that the lower mantle in this region is stiff and that the response of the lower mantle to ice melt is slow. The simulated gravity field was found to be relatively insensitive to the value of the upper mantle viscosity. This is expected due to the large size of the Laurentide ice sheet, and because I only investigated the long-wavelengths of the gravity field.

Next, I decided to focus on the horizontal surface motion due to GIA, which affects Global Navigation Satellite Systems (GNSS) measurements of ice melt and tectonics. Horizontal surface motion due to GIA is the net effect of opposing motions in the lithosphere and the mantle. During unloading, the Earth rebounds with outward lithosphere flexure and inwards mantle flow. Whether outward lithosphere flexure or inward mantle flow dominates is determined by the mantle viscosity and the size of the load. For a highly viscous mantle, relaxation in response to ice mass changes that occurred several thousand years ago is not finished, leading to significant inwards mantle flow. On the other hand, if the mantle is weak with a low viscosity, mantle flow is small and outward lithosphere flexure dominates. This complicates interpretations of observed horizontal surface motion, which is reflected in the disagreement between past modelling studies on the contribution of GIA to observed horizontal surface motion in Hudson Bay. While some model studies suggest that GIA in this area leads to horizontal surface motion pointing outward from the former load, other studies found a GIA contribution to horizontal surface motion of several mm a^{-1} that is directed towards the former load.

I analysed horizontal GIA motion due to a circular disk load, which is representative for an ice sheet but with a sharp decrease in ice height at the ice edge. Such a simple ice sheet configuration is used here to better understand the underlying processes and resulting horizontal surface motion. I focused on two approximations: 1) approximating horizontal deformation of GIA using Cartesian models rather than spherical models, and 2) approximating compressible Earths as incompressible in GIA models.

With Cartesian models, ice melt and growth in smaller-scale regions such as Alaska, Iceland or Patagonia can be studied with a higher resolution and a relatively short computation time. For vertical deformation, neglecting sphericity can be compensated by also neglecting self-gravity, which makes Cartesian models applicable for simulating GIA uplift of ice sheets up to the size of the Fennoscandian ice sheet. However, I find that such compensation does not occur for horizontal deformation. I find that Cartesian models are only applicable for simulating GIA due to ice sheets smaller than 200 km in radius when the error due to the approximation becomes significant compared to the error in measurement of horizontal velocities.

Compressibility refers to the dilatation or compression of individual elements in a GIA model. Compressibility significantly changes the horizontal motion of GIA. However, compressibility is hard to implement, especially in finite-element models that are used to analyse 3D Earth structure variations. Several models therefore resort to the assumption of incompressibility or material compressibility.

I studied the approximation of compressibility for horizontal GIA deformation using 1) incompressible models, 2) material compressible models, and 3) compressible models. Material compressible models have a Poisson ratio below 0.5, but do not adjust the buoyancy force for the change in density due to compression. Models that correctly simulate compressibility both allow for material compression and also adjust the buoyancy force accordingly. I find that the error made by assuming material compressibility is independent of the size of the employed ice sheet for horizontal motion. For ice sheets smaller than 200 km in radius, both compressible and material compressible models are reasonably accurate. Thus, (material) compressible Cartesian GIA models can be employed in studies that aim to investigate small-scale horizontal deformation of several mm/yr due to GIA in areas like Alaska, Iceland, or Patagonia.

I then adapted the compressible Cartesian GIA model for Southeast Alaska, a region characterised by complex tectonic motion and significant GIA which influences observations of horizontal motion in the area. GIA in Southeast Alaska is most prominent in Glacier Bay, an area that has experienced significant ice melt in the last 250 years. In Glacier Bay, vertical uplift of 30 mm a^{-1} and horizontal deformation up to 7 mm a^{-1} are recorded. Regional and global tomography studies show lateral variations in seismic velocities below Southeast Alaska, which translate to lateral viscosity variations under the assumption that the seismic velocity variations are caused by variations in temperature. Currently, it is unclear what the effect is of lateral viscosity variations on the horizontal motion due to GIA in Southeast Alaska. I do know that horizontal surface motions are very sensitive to lateral viscosity variations. From the numerical modelling in this dissertation, I indeed find a large spread in modelled horizontal motion using GIA models with plausible 3D viscosities. Values for the simulated horizontal motion are less than 1 mm a^{-1} using flowlaws that convert temperature to viscosity. However, when viscosities are calculated from seismic velocity anomalies through the assumption that these are solely caused by fluctuations in temperature, I find horizontal velocities up to 4 mm a^{-1}. This shows that a difference in simulated horizontal motion persists due to unknown lateral viscosity.

Last, I investigated the tectonic setting of Southeast Alaska. To do so, I corrected observed horizontal motions for the effect of GIA using a model with lateral viscosity. The tectonic setting of Southeast Alaska is complicated, with many documented faults. Previous studies have used tectonic block models to estimate plate velocities in the region. However, these studies have performed a GIA correction to the observed horizontal motions using an incompressible GIA model with a radially varying viscosity structure. I investigated if a more advanced 3D GIA model alters the obtained tectonic motion and the configuration of faults in the area. I found that using a GIA model with a 3D viscosity reduced the misfit of the tectonic block model to observations. However, this reduction is not found to be more important than the uncertainty in the location of the faults. In a future study, the best fault configuration and 3D viscosity should be found by varying the fault configuration of the tectonic block model simultaneously with the 3D viscosity in the GIA model.

This thesis presents improvements for modelling and applying the long-wavelength gravity field and horizontal motion signal due to GIA. Future studies could improve on the chapters presented in this thesis in several ways. First, the gravity field can be simulated by coupling more complicated mantle convection and GIA models to the crustal model, for example using models incorporating lateral viscosity variations. These improvements can be implemented in a study focusing on linking the observed gravity field to mantle convection or GIA in areas on Earth other than Hudson Bay. Similarly, the compressible Cartesian GIA model can be used to study horizontal motion in other small-scale areas like Iceland. However, compressible spherical GIA models are needed to simulate horizontal motion in larger areas.

SAMENVATTING

In het verleden is de aarde onderworpen aan periodes van ijsaangroei en ijssmelt. De ijskappen op aarde voeren een druk uit op het oppervlak, waarbij ze de grond eronder als het ware indrukken. Wanneer ijs smelt, reageert de aarde door terug te veren en het oppervlakte te verhogen. Dit proces heet postglaciale opheffing. Glaciale isostatische opheffing, *Engels: Glacial Isostatic Adjustment (GIA)*, wordt beschouwd als een meer algemene term, namelijk de reactie van de vaste aarde op een herverdeling van landijs en oppervlaktewater volgend op aangroei of smelt van landijs. Hier valt postglaciale opheffing onder.

Vandaag de dag wordt er een opheffing tot 13 mm per jaar gemeten nabij Hudson Bay in Noord Amerika, als reactie op het smelten van ijskappen in dit gebied tussen achttienduizend en zesduizend jaar geleden. Nog hogere snelheden zijn gemeten in Zuidoost Alaska, tot wel 30 mm per jaar, als reactie op ijssmelt die slechts 250 jaar geleden is begonnen. Een deel van het verschil tussen de gemeten waardes in Hudson Bay en Zuidoost Alaska kan verklaard worden door de viscositeit van de aardmantel. De viscositeit van de aardmantel bepaalt namelijk hoe snel materiaal in de mantel kan stromen. Een hoge waarde voor de viscositeit betekent dat materiaal in de aardmantel erg langzaam stroomt, terwijl een lagere waarde voor de viscositeit inhoudt dat het materiaal in de aardmantel juist makkelijk stroomt. De viscositeit van de mantel onder Hudson Bay wordt geschat op die van het gemiddelde op aarde, namelijk 10^{21} Pa s, terwijl de viscositeit van de mantel in Zuidoost Alaska enkele ordes van grootte kleiner wordt geschat. GIA onderzoek wordt uitgevoerd om erachter te komen wat de structuurparameters zijn van het binnenste van de aarde, zoals de viscositeit van de mantel. Met meer kennis van GIA kunnen metingen beter gecorrigeerd worden voor het effect ervan. Het doel van dit proefschrift is om de numerieke modelopzet van GIA onderzoek te verbeteren, waardoor het binnenste van de aarde nauwkeuriger gesimuleerd kan worden.

In het statische zwaartekrachtveld, gemeten door satellieten, is GIA zichtbaar als negatieve anomalieën in gebieden die voorheen bedekt zijn geweest met ijs en waar de opheffing van het land nog niet geëindigd is. Op deze locaties is het oppervlak van de aarde lager dan zijn evenwichtshoogte wat ervoor zorgt dat er lokaal een massa tekort is. Dit resulteert in een negatieve anomalie in het zwaartekrachtveld. Het blijft echter moeilijk om een waargenomen negatieve anomalie direct toe te schrijven aan het GIA proces, aangezien satellieten het resultaat meten van dynamische processen en dichtheidsverschillen in alle lagen van de aarde.

In Hudson Bay is een negatieve zwaartekrachtsanomalie waargenomen van ongeveer 50 mGal. De locatie van deze anomalie vertoont overeenkomsten met het gebied dat 26 duizend jaar geleden bedekt was met de Laurentide-ijskap, *Engels: Laurentide Ice Sheet*, toen deze op zijn grootst was. Sommige studies suggereren dat GIA een verwaarloosbare contributie levert aan deze gemeten zwaartekrachtsanomalie, terwijl andere studies suggereren dat meer dan de helft van de waargenomen zwaartekrachtsanomalie toegeschreven kan worden aan GIA. Deze studies berekenen echter het zwaartekrachtsveld door resultaten van modellen voor de korst-lithosfeer-asthenosfeer, *Engels: Crust-Lithosphere-Asthenosphere (CLA)*, GIA en mantelconvectie bij elkaar op te tellen. In hoofdstuk 3 combineer ik modellen voor de CLA, GIA en mantelconvectie door de krachten van GIA en mantelconvectie toe te voegen aan de krachtenbalans van het CLA model. Met deze geïntegreerde aanpak wordt 60% van de waargenomen anomalie verklaard door GIA. Een dergelijke grote contributie van GIA vereist dat de viscositeit van het diepere deel van de mantel groter is dan 10^{22} Pa s, hoger dan gevonden in verschillende eerdere studies. Deze hoge waarde voor de viscositeit van de diepere mantel betekent dat de diepere mantel in dit gebied stijf is en dat de reactie op ijssmelt hier langzaam gaat. Het gesimuleerde zwaartekrachtsveld is relatief ongevoelig voor de waarde van de viscositeit in het ondiepere deel van de mantel. Dit was ook verwacht vanwege de grootte van de Laurentide-ijskap en omdat alleen gekeken is naar de lange golflengtes van het zwaartekrachtsveld.

Hierna is onderzoek gedaan naar de bijdrage van GIA aan horizontale bewegingen van het oppervlak. Horizontale bewegingen horend bij het GIA proces beïnvloeden metingen van ijssmelt en plaattektoniek die zijn gedaan door wereldwijde satellietsystemen, *Engels: Global Navigation Satellite Systems (GNSS)*. De door GIA veroorzaakte horizontale beweging aan het oppervlak is het netto resultaat van tegengestelde bewegingen in de lithosfeer en de mantel. Tijdens periodes van ijssmelt veert het land terug met een naar buiten gerichte beweging in de lithosfeer en een naar binnen gerichte stroming van de mantel. Of de naar buiten gerichte beweging van de lithosfeer domineert of de naar binnen gerichte beweging van de mantel wordt bepaald door de viscositeit van de mantel en door de grootte van de ijsmassa. Voor een erg viskeuze mantel is de reactie van de mantel op ijssmelt van meerdere duizenden jaren geleden nog niet geëindigd. Aan de andere kant geldt dat de reactie van de mantel op ijssmelt al wel geëindigd is wanneer de viscositeit van de mantel relatief laag is. In dat geval domineert de naar buiten gerichte beweging van de lithosfeer en zal er aan het oppervlak een naar buiten gerichte beweging worden waargenomen. De beweging van het oppervlakte is dus het resultaat van twee tegengestelde processen en dit maakt het lastig om de waargenomen horizontale beweging aan het oppervlak te interpreteren. Dit blijkt ook uit de verschillende conclusies van modelstudies uit het verleden naar de bijdrage van GIA aan de waargenomen horizontale oppervlaktebeweging. Waar sommige modelstudies suggereren dat GIA in dit gebied leidt tot een naar buiten gerichte horizontale oppervlaktebeweging (gezien vanaf de voormalige ijsmassa), vinden andere studies een bijdrage van GIA aan de horizontale beweging van het oppervlak die enkele mm per jaar is en juist gericht naar de voormalige ijsmassa toe.

Als eerste is gekeken naar de horizontale GIA beweging ten gevolge van het afsmelten van een ijskap in de vorm van een cirkelvormige schijf, representatief voor een ijskap met een scherpe grens in de ijshoogte bij de ijsrand. Deze simpele configuratie voor een ijskap is gebruikt om een beter begrip te krijgen van de onderliggende processen en resulterende horizontal beweging van het oppervlak. Hierbij is gekeken naar twee benaderingen: 1) de benadering van horizontale GIA beweging met een Cartesiaans model in plaats van een bolvormig model, en 2) het benaderen van de compressibele aarde als incompressibel binnen GIA modellen. Deze twee benaderingen worden in de alinea's hieronder verder toegelicht.

Met Cartesiaanse modellen kunnen ijssmelt en aangroei in kleine gebieden als Alaska, IJsland of Patagonië worden onderzocht met een hoge resolutie en een relatief kleine rekentijd. Bij verticale GIA-gerelateerde bewegingen wordt het negeren van de bolvormigheid gecompenseerd door het negeren van zelf-zwaartekracht *Engels: self-gravity*. Hierdoor zijn Cartesiaanse modellen toepasbaar bij simulaties van verticale GIA-gerelateerde bewegingen wanneer de ijskap van de GIA simulatie niet groter is dan de voormalig ijskap in Fennoscandia, *Engels: Fennoscandian Ice Sheet*. Echter wordt er in dit proefschrift gevonden dat een dergelijke compensatie niet plaatsvindt voor horizontale GIA bewegingen. Op basis van het huidige verschil tussen metingen van horizontale bewegingen en modelresultaten zijn Cartesiaanse modellen slechts bruikbaar voor het simuleren van horizontale GIA-gerelateerde bewegingen wanneer de ijskap een straal van minder dan 200 km heeft.

Compressibiliteit wijst op de dilatatie of compressie van individuele elementen in een GIA model. Het GIA proces simuleren op een compressibele aarde geeft significante andere resultaten voor de horizontale GIA-gerelateerde bewegingen ten opzichte van simulaties op een incompressibele aarde. Echter is het lastig om compressibele aardes te simuleren, helemaal in modellen die gebaseerd zijn op de eindige elementen methode, *Engels: Finite Element Method (FEM)*, welke gebruikt worden om het effect van 3D variaties in structuur van de aarde te analyseren. De meeste modellen beschouwen daarom een incompressibele of materiaal-compressibele aarde, *Engels: material compressibility*.

Het effect van compressibiliteit is in dit proefschrift getest met behulp van 1) incompressibele modellen, 2) materiaal-compressibele modellen en 3) volledig compressibele modellen. Materiaal-compressibele modellen hebben een Poisson ratio van minder dan 0.5, maar in deze modellen wordt de opwaartse kracht, *Engels: buoyancy force*, niet aangepast voor de dichtheidsverandering door compressie. Volledig compressibele modellen staan compressie van het materiaal toe en passen daarnaast ook de opwaartse kracht aan. In dit proefschrift is gevonden dat de fout die gemaakt wordt door aan te nemen dat modellen materiaal-compressibel zijn voor horizontale beweging onafhankelijk is van de grootte van de ijskap. Wanneer ijskappen een straal van minder dan 200 km hebben, zijn zowel volledig compressibele als materiaal-compressibele modellen voldoende nauwkeurig. (Materiaal-)compressibele Cartesiaanse GIA modellen kunnen dus gebruikt worden in studies gericht op het analyseren van horizontale verplaatsingen van enkele mm per jaar op kleine schaal, bijvoorbeeld in regio's als Alaska, IJsland en Patagonië.

Het in dit proefschrift ontwikkelde compressibele Cartesiaanse GIA model is vervolgens gebruikt voor het analyseren van horizontale bewegingen in Zuidoost Alaska. Deze regio staat bekend om zijn complexe tektoniek en significante GIA die waarnemingen van horizontale bewegingen in het gebied beïnvloedt. GIA is in zuidoost Alaska het meest aanwezig in Glacier Bay, een gebied dat onderhevig is aan significante ijssmelt in de laatste

250 jaar. Hier zijn verticale opheffingssnelheden van 30 mm per jaar en horizontale bewegingen tot 7 mm per jaar geregistreerd. Regionale en globale tomografie studies laten zien dat er laterale verschillen aanwezig zijn in de seismische snelheden onder zuidoost Alaska. Deze vertalen zich naar laterale variaties in de viscositeit onder de aanname dat de variaties in seismische snelheden veroorzaakt worden door variaties in temperatuur. Op dit moment is het onduidelijk wat het effect is van laterale variaties in viscositeit op de horizontale GIA-gerelateerde beweging in zuidoost Alaska. Wel is bekend dat de horizontale oppervlaktebeweging erg gevoelig is voor laterale variaties van de viscositeit. Uit numerieke modellen in dit proefschrift wordt inderdaad een grote spreiding gevonden in de gemodelleerde horizontale beweging wanneer GIA modellen gebruikt worden met plausibele 3D viscositeiten. Waardes voor de gesimuleerde horizontale beweging zijn bijvoorbeeld minder dan 1 mm per jaar wanneer stromingswetten worden gebruikt voor de omrekening van temperatuur naar viscositeit. Echter, als de viscositeit wordt berekend met behulp van fluctuaties in seismische snelheden, met de aanname dat deze uitsluitend worden veroorzaakt door fluctuaties in de temperatuur, dan worden horizontale snelheden tot 4 mm per jaar gevonden in Glacier Bay. Dit laat zien dat er een verschil is in de gesimuleerde horizontale beweging door de onbekende viscositeit.

Als laatste is er in dit proefschrift gekeken naar het effect van GIA op de tektonische setting van zuidoost Alaska. De tektonische configuratie van zuidoost Alaska is gecompliceerd, met veel gedocumenteerde breuken. Eerdere studies hebben tektonische blokmodellen gebruikt om de plaatsnelheden in de regio te schatten. Echter hebben deze studies een GIA correctie toegepast op de waargenomen horizontale snelheden met een incompressibel GIA model met een viscositeitsstructuur die alleen radieel varieert. In hoofdstuk 5 is uitgezocht of een meer geavanceerd 3D GIA model de verkregen tektonische snelheden en de configuratie van de breuklijnen in zuidoost Alaska verandert. Hiervoor zijn de geobserveerde horizontale bewegingen gecorrigeerd met een GIA model dat laterale viscositeitsvariaties bevat. Een van de bevindingen is dat het gebruiken van een GIA model met laterale viscositeitsvariaties zorgt voor een betere overeenkomst tussen gemodelleerde tektonische snelheden en waarnemingen. Deze reductie is echter niet belangrijker dan de onzekerheid in de configuratie van de breuken. In een toekomstige studie zou de beste combinatie tussen 3D viscositeit en de configuratie van de breuken gevonden kunnen worden door de configuratie van de breuken samen met de 3D viscositeit in het GIA model te variëren.

Dit proefschrift presenteert verbeteringen voor het modelleren en toepassen van GIA in het langgolvige zwaartekrachtsveld en voor horizontale GIA-gerelateerde bewegingen. In toekomstige studies kunnen verbeteringen doorgevoerd worden op verschillende manieren. Ten eerste kan het zwaartekrachtsveld gesimuleerd worden door meer geavanceerde mantelconvectie en GIA modellen te koppelen aan het korst model, bijvoorbeeld door gebruiken te maken van modellen met laterale viscositeitsvariaties. Deze verbeteringen zouden geïmplementeerd kunnen worden in een studie die zich focust op het koppelen van het waargenomen zwaartekrachtsveld aan mantelconvectie of GIA in andere regio's op aarde dan Hudson Bay. Op een vergelijkbare manier zou het compressibele Cartesiaanse GIA model gebruikt kunnen worden om horizontale bewegingen te bestuderen in kleine gebieden als IJsland. Voor het simuleren van horizontale beweging in grotere gebieden zijn echter compressibele bolvormige GIA modellen nodig.

1

INTRODUCTION

1.1. INTRODUCTION TO GLACIAL ISOSTATIC ADJUSTMENT

The Earth has known many periods of extensive ice cover followed by ice melt. In the presence of ice sheets the Earth's surface directly below the ice sheet is depressed. The Earth rebounds when these ice sheets melt, a process known as Glacial Isostatic Adjustment (GIA). The rebound works via an elastic response and via a viscous response of the crust and mantle. The elastic response is instantaneous, and the viscous response covers decades to thousands of years after removal of the load. The characteristic timescale of the viscous response is determined by how fast the mantle material within the Earth is allowed to flow, which is in turn determined by its viscosity. Today, uplift of up to 13 mm a^{-1} is recorded around Hudson Bay (Figure 1.1), even though the last ice sheets have melted away between eighteen and six thousand years ago (e.g., *Kreemer et al.*, 2018; *Robin et al.*, 2020; *Simon et al.*, 2016). Other areas on Earth respond faster. In Southeast Alaska, for example, uplift rates of more than 30 mm a^{-1} are measured (*Hu and Freymueller*, 2019; *Larsen et al.*, 2005). The viscous response in this area is already significant for ice-melt that occurred 250 years ago, much more recent than the Late Pleistocene ice melt. This is due to the mantle viscosity in the region being a few order of magnitude lower than the global average.

In this thesis, I discuss the GIA in these two areas of North America. First, I investigate the large-scale area centred around Hudson Bay (Figure 1.1). This area was covered by the Laurentide ice sheet roughly 26,000 years ago when the extent of the Laurentide ice sheet was at its maximum (*Stokes*, 2017). The maximum ice thickness of the Laurentide ice sheet is estimated to be between 3,000 and 5,000 m (Figure 1.1, *Lambeck et al.*, 2017; *Peltier et al.*, 2015). Later, I focus on the small-scale region in Southeast Alaska. This region contains glaciers subject to significant ice loss since 1700 (*Larsen et al.*, 2005).

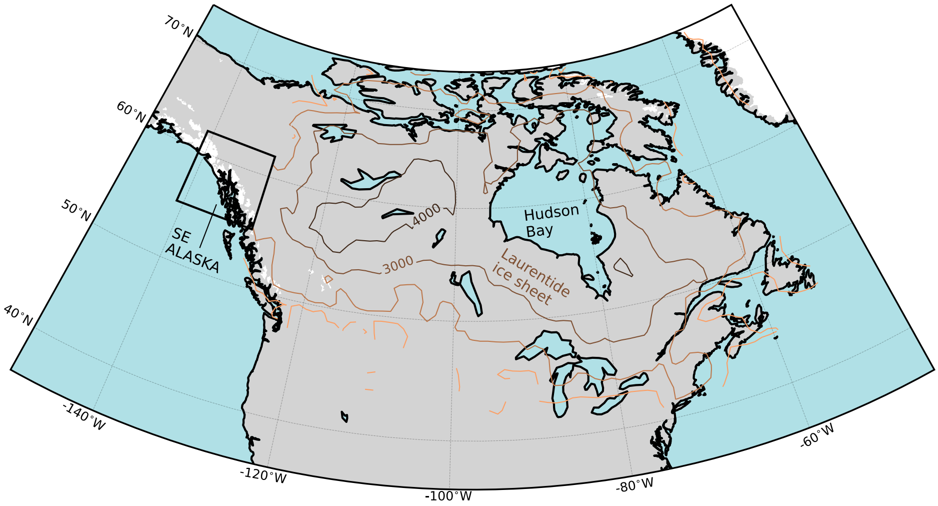

Figure 1.1: Geographic map of the study areas discussed in this thesis. The contour lines indicate the ice thickness of the Laurentide Ice sheet at LGM according to ice model ICE-6G (*Argus et al.*, 2014; *Peltier et al.*, 2015). Chapter 3 discusses the imprint of the deglaciation of the Laurentide ice sheet on the static gravity field. Glaciers that are present today are shown in white. Some of them are located in Southeast (SE) Alaska, which is the study area of Chapter 5.

.

1.2. GLACIAL ISOSTATIC ADJUSTMENT IN NORTH AMERICA

GIA studies in North America have analysed 1) records of relative sea level (RSL) (e.g., *Engelhart et al.*, 2011; *Roy and Peltier*, 2015), 2) Global Navigation Satellite Systems (GNSS) observations of vertical and horizontal crustal motions (e.g., *Sella et al.*, 2007), and 3) measurements of the (time-variable) gravity field (e.g., *Métivier et al.*, 2016; *Tamisiea et al.*, 2007). Records of paleo-sea level are used to calibrate and improve GIA models, which are used to correct the present-day sea level. However, along both the Atlantic and Pacific coasts 1D GIA models are not able to match paleo sea level observations in all locations simultaneously (*Engelhart et al.*, 2011; *Yousefi et al.*, 2018). GNSS observations of horizontal and vertical crustal motions are analysed by *Sella et al.* (2007), and compared to GIA model output. With their 1D GIA model, they were unable to fit both the horizontal and vertical GNNS motions with the same set of models. Observations of the time-variable gravity field by GRACE are used to calibrate the GIA model, and the calibrated model is then used to predict the effect of GIA on the static (non time-variable) gravity field (*Tamisiea et al.*, 2007). Another observable is J2-dot, which is the time derivative of the degree two zonal spherical harmonic of the Earth's gravitational potential, a measure of the oblateness of the Earth. The value of J2-dot is most sensitive to the viscosity of the deep lower mantle (<1600 km depth, *Lau et al.*, 2016), whereas observables like RSL are more sensitive to the viscosity of shallower layers in the mantle.

In this thesis, I focus on the static (non time-variable) gravity field and on horizontal

GIA-related motions. In the following section, I introduce these observables in more detail and exhibit an overview of existing modelling studies on gravity anomalies and horizontal motions in North America.

1.3. GLACIAL ISOSTATIC ADJUSTMENT OBSERVABLES

1.3.1. GRAVITY ANOMALIES

A gravity anomaly can be understood as the difference between the observed gravity, and that predicted by a theoretical model, usually the gravity field of a rotating ellipsoid. In Chapter 3, I use the free-air gravity anomaly. This is the gravity anomaly on the perturbed surface, corrected to the height of the geoid using the free-air correction (*Mitrovica and Peltier*, 1989). A gravity anomaly reveals locations of mass reduction or accumulation. One reason for a mass reduction can be the deflection caused by glaciations which have depressed the ground underneath and pushed mass deeper and outward, resulting in less mass at that location and a negative anomaly in the gravity field (*Root et al.*, 2015). However, the gravity field exhibits the result of the total mass, which is aggregated over depth. A negative anomaly is hence not necessarily related to GIA, but can also be related to other processes like mantle convection or to density anomalies in the crust or lithosphere. With models these effects can be disentangled and improve our understanding of the observed gravity anomalies.

The longer wavelengths of the static and temporal gravity field are imaged by satellite observations. Sometimes, these satellite observations are combined with terrestrial data for the smaller wavelengths signals. In Chapter 3, I address the long-wavelength negative gravity anomaly over Hudson Bay. By filtering out wavelengths smaller than 600 km, I focus mostly on satellite data, which has seen significant improvements in terms of accuracy since the launch of several dedicated gravity field missions: the Challenging Minisatellite Payload (CHAMP, *Reigber et al.*, 2002), the Gravity field and Ocean Circulation Explore (GOCE, *Drinkwater et al.*, 2003), the Gravity Recovery and Climate Experiment (GRACE, *Tapley et al.*, 2004), and the Gravity Recovery and Climate Experiment Follow-On (GRACE-FO, *Landerer et al.*, 2020). In this thesis, I use gravity field model XGM2016 (*Pail et al.*, 2018), which combines satellite data from satellite-only gravity model GOCO5s (*Mayer-Guerr*, 2015) with terrestrial data provided by the United States National Geospace-Intelligence Agency (NGA). The satellite data of the gravity model is retrieved from the GOCE and GRACE missions, as well as from kinematic orbits of 9 Low Earth Orbiting satellites (LEOs) and 6 Satellite Laser Ranging (SLR) satellites. The data are combined using largely the same methodology as for GOCO5c (*Fecher et al.*, 2017). The long wavelength signal of gravity field model XGM2016 is exhibited in Figure 1.2.

Over North America, a reduced gravitation pull can be seen in the gravity field (Figure 1.2, indicated by a dashed red line) suggesting a relation with the previous glaciation of the Laurentide ice sheet that was located in roughly the same location (*Kaula*, 1972; *Walcott*, 1970). The measurement error in the gravity field is small. Already for the GOCE mission launched in 2006, satellite gravity observations were required to have an accuracy of 1-2 mGal for a spatial resolution of roughly 100 km (*Drinkwater et al.*, 2003), and

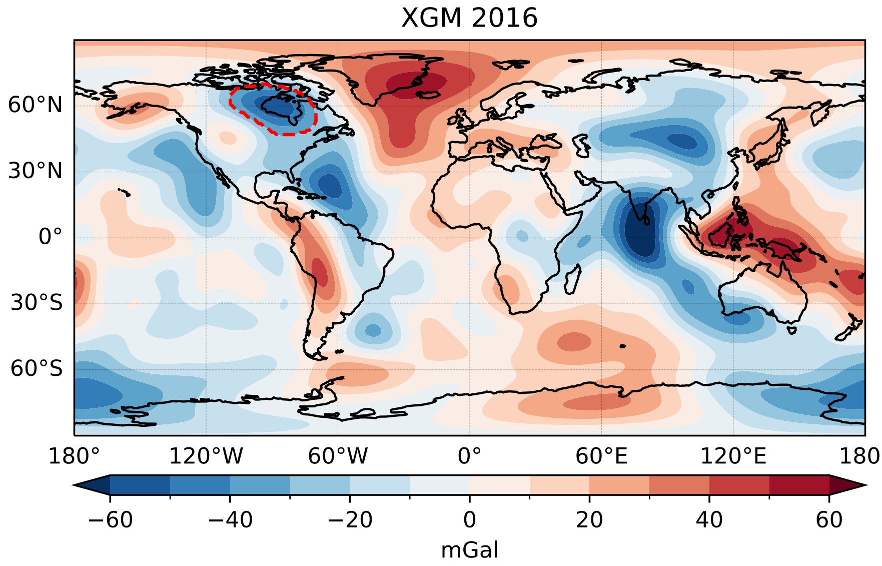

Figure 1.2: Gravity anomalies of gravity model XGM2016 for spherical harmonic degrees 2 to 15 (*Pail et al.*, 2018). The negative anomaly over Hudson Bay, circled by the red dashed line, is the focus of Chapter 2.

.

after the GOCE mission this was further reduced (*Fecher et al.*, 2017). Nevertheless, the interpretation of the gravity field remains uncertain. Previous studies are not in agreement on the relative contribution of Glacial Isostatic Adjustment to the observed negative anomaly over North America. The first studies that investigated this anomaly did not find a significant contribution of GIA (*Cathles*, 1975; *James*, 1992; *Peltier et al.*, 1992). However, *Simons and Hager* (1997) found that about half of the observed anomaly can be explained by GIA, and more recently *Métivier et al.* (2016) found that incomplete GIA explains more than 80 percent of the signal. The different conclusions can partly be explained by the different inferences of the viscosity of the Earth's mantle. Currently, no consensus has been reached on the importance of GIA in explaining the gravity anomaly, nor on the value of the mantle viscosity beneath North America.

Chapter 3 of this thesis focuses on modelling the long-wavelength gravity field of North America by including GIA and mantle convection as forces acting on the bottom of the Crust-Lithosphere-Asthenosphere (CLA) model. This approach is different from that of previous studies where the gravity field is computed using a linear addition of contributions from the crust, GIA and the mantle (e.g., *Métivier et al.*, 2016). The method used in this thesis is illustrated in Figure 1.3, and explained as follows. The forces of the crust (F_{crust}), lithosphere (F_{litho}), and asthenosphere (F_{asth}) are directed downward due to their weight. The part of the processes of GIA and mantle convection that is not contained in the geometry of the CLA model can be represented by stresses at the bottom of the CLA model, and are implemented as forces (F_{GIA} and F_{DT}). F_{DT} represents the force

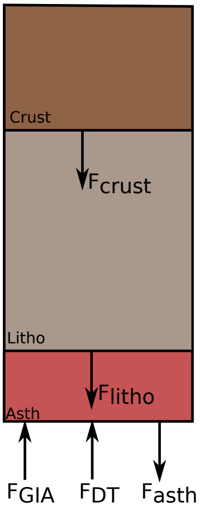

Figure 1.3: The forces involved in the combined model. The forces exerted by the crustal, lithospheric and asthenospheric layers are denoted by F_{crust}, F_{litho} and F_{asth}, respectively. F_{GIA} and F_{DT} are the forces due to GIA and dynamic topography.

due to dynamic topography, which is the surface topography due to mantle convection (*Hager et al.*, 1985). The sum of all of these forces should equal the weight of a reference column (F_{ref}). This can be summarised with the following equation:

$$F_{crust} + F_{litho} + F_{asth} - F_{GIA} - F_{MC} = F_{ref} \tag{1.1}$$

In Section 2.1, I explain the contributions of the crust (*Root et al.*, 2015), mantle and GIA in detail.

1.3.2. HORIZONTAL VELOCITIES

The GIA induced horizontal motion is the result of opposing motions in the lithosphere and in the mantle (Figure 1.4). During loading, flexure in the lithosphere results in a downward and inward motion of the surface underneath the load, while the motion of the bottom crust and mantle flow are outwards (*O'Keefe and Wu*, 2002). After removal of the ice sheet, lithosphere flexure results in outward motion, while the viscous mantle flow is inward. It depends on the size of the load and on the mantle viscosity whether lithosphere flexure or whether mantle flow dominates. If the average mantle viscosity is low ($\sim 10^{20}$ Pa s), the present-day response of the inward flowing viscous mantle of post-LGM mass changes is small, and outward lithosphere flexure dominates (*Hermans et al.*, 2018). The total horizontal motion at the surface is thus a combination of motion in the crust/lithosphere and mantle flow. For example, for a highly viscous mantle of 10^{22} Pa s, relaxation in response to these ice changes has not finished today, and inward mantle flow is still ongoing leading to inward horizontal surface motions.

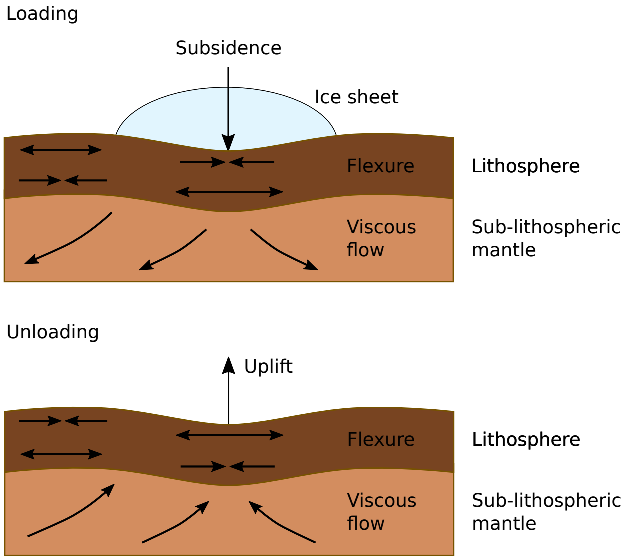

Figure 1.4: Schematic of the motion associated with Glacial Isostatic Adjustment. Adapted from *Hüttl* (2011).

Research on horizontal motions from GIA kicked off with the advent of space geodetic measurement techniques like Very Long Baseline Interferometry (VLBI), Laser Satellite Ranging (SLR), and Global Positioning System (GPS) which enabled measurements of crustal movements with accuracy of 1 mm a^{-1}. However, before that, the first modelling study on horizontal velocities in North America was *James and Morgan* (1990), who predicted that these were several mm a^{-1} in magnitude, and were pointing towards the former load in Hudson Bay. The direction of these velocities is explained by the massive amount of mantle material that was flowing inward after deglaciation of the Laurentide ice sheet. *Spada et al.* (1992) found horizontal GIA-related velocities in North America that are directed towards and away from Hudson Bay, and that these are sensitive to the viscosity increase in the transition zone and also to the density stratification. Later, several studies suggested horizontal motion below the former ice sheet that pointed outward from Hudson Bay (*James and Lambert*, 1993; *Mitrovica et al.*, 1994a; *Peltier*, 1998). In addition, one study arrived at velocities outside the former ice sheet that were almost negligible (*James and Lambert*, 1993), and another study simulated small (~ 0.5 mm a^{-1}) motion towards the former ice sheet (*Mitrovica et al.*, 1994a). *Peltier* (1998) found that the signal outside the former ice sheet depends on the underlying mantle viscosity. Observational evidence shows outward motion below the ice sheet and complicated velocity variations outside of the former ice sheet (*Sella et al.*, 2007). *Kreemer et al.* (2018) use a strain rate estimation algorithm, and find extension of > 2 mm a^{-1} beneath the ice sheet and contraction of 1-2 mm a^{-1} outside of the ice sheet.

In a tectonically complex region such as Alaska, GIA is used as a correction on the horizontal GNSS velocities in order to obtain improved plate motion estimates (e.g., *Elliott and Freymueller*, 2020; *Elliott et al.*, 2010). The horizontal GIA deformation in the region is only 7 mm a^{-1} at most (*Elliott et al.*, 2010), which is small compared to plate motions that are on the order of cm a^{-1}. Nevertheless, the effect of GIA in tectonic studies (*Klemann et al.*, 2008) should still be considered. The GIA models that are employed in these tectonic studies are simplified. For example, the studies of *Elliott et al.* (2010) and *Elliott and Freymueller* (2020) have employed the GIA code TABOO (*Spada*, 2003). This code simulates incompressible deformation and can include only radially varying viscosity profiles. It is currently unclear how big the error is that is introduced by these approximations, and if a more advanced compressible model with 3D Earth rheology would significantly alter the tectonic setting in the area.

Figure 1.5 exhibits the observed horizontal velocities in Alaska before correcting for GIA, which shows large Northwest directed velocities of up to 50 mm/yr west of the Fairweather fault and velocities that seldomly exceed 10 mm/yr to the east of this fault. This confirms the finding by *Mazzotti et al.* (2003) that most relative motion is taken in by the Fairweather-Queen Charlotte system. Furthermore, horizontal velocities near the coastline are directed North/Northwest, but further inland I find observed velocities that are directed to the North/Northeast.

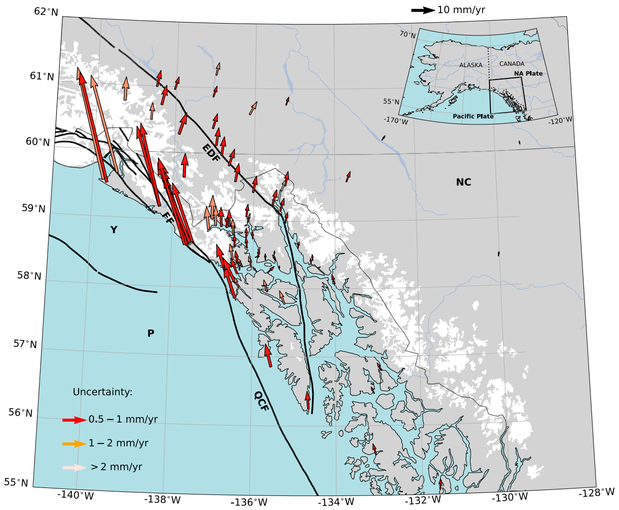

Figure 1.5: Observed horizontal GNSS velocities in Southeast Alaska for the period 2003-2012. Abbreviations are P=Pacific plate, Y= Yukatat block, FF=Fairweather Fault, QCF = Queen Charlotte Fault, EDF = Eastern Denali Fault, NC= Northern Cordillera. The faults shown in this figure are taken from the Alaska Quaternary Faults and Folds database (*Koehler et al.*, 2012). The white patches depict the current glaciers in the area.

Horizontal motion is most sensitive to the viscosity of the upper mantle (< 670 km depth, *Wu*, 2006). However, due to contrasting motions in the lithosphere and the mantle, the observed horizontal surface motion is difficult to interpret. Furthermore, horizontal motions due to GIA are also very sensitive to lateral viscosity variations (e.g., *Gasperini et al.*, 1990; *Kaufmann et al.*, 2005; *Latychev et al.*, 2005; *O'Keefe and Wu*, 2002; *Steffen et al.*, 2006). Therefore, I discuss the inclusion of lateral viscosity variations within GIA models next.

1.4. MODELLING GLACIAL ISOSTATIC ADJUSTMENT WITH LATERAL VISCOSITY VARIATIONS

Global tomography studies show that both radial and lateral viscosity variations exist within the Earth (e.g., *Porritt et al.*, 2021; *Schaeffer and Lebedev*, 2013), which I label in the following as 3D Earth structure (Figure 1.6). The effect of 3D Earth structure on GIA model results has been the focus of numerous studies. However, 1D GIA models which only employ radial variations in the structure of the Earth are still widely used. The 1D models have a lower computational cost, which enables many simulations to be performed in a short amount of time. A run with 1D models that are based on the Normal Mode Method (*Wu and Peltier*, 1982) only takes seconds to minutes, while a simulation of a finite-element model with 3D Earth structure takes several hours to multiple days. This means that many parameter values can be easily tested in 1D GIA models, while 3D GIA models can only run a limited selection of parameter values in the same amount of time.

The lateral Earth structure variations in GIA models are commonly determined from seismic velocities anomalies (e.g., *Latychev et al.*, 2005; *Li et al.*, 2018; *Steffen et al.*, 2006) in combination with high pressure, high temperature laboratory observations. One such scaling from seismic velocity anomalies to viscosity is explained in *Ivins and Sammis* (1995), and is based on the assumption that temperature anomalies are responsible for the shear wave anomalies in the seismic model. *Wu et al.* (2013) extended this method by introducing a factor between 0 and 1 to denote the unknown thermal contribution of the seismic shear wave anomalies, thereby also allowing a scaling of the magnitude of the calculated viscosity variations. The method superimposes the calculated viscosity anomalies on a reference 1D viscosity model, and is therefore a way to test the effect of perturbations in a reference model. Another method is based on diffusion creep and dislocation creep, which are both known to exist in the upper mantle (*Karato*, 1993). In this method, the viscosity is calculated from temperatures using flow laws for olivine which is the dominant material in the upper mantle. This method does not require a reference viscosity model, but uses free parameters for grain size and water content. A model providing temperatures for the lithosphere and upper mantle is WINTERC-G (*Fullea et al.*, 2021). WINTERC-G is a thermochemical model down to a depth of 400 km generated using seismic waveform inversions and data for heat flow, surface elevation, and satellite gravity.

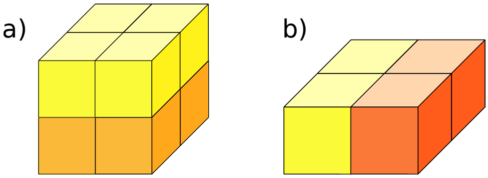

Figure 1.6: Schematic illustration of a) radial variations, and b) lateral variations in elements of the Earth model

In North America, 3D GIA models have previously been used to assess the effect of lateral Earth structure on observations of relative sea level (RSL). *Paulson et al.* (2005) noted that

GIA observables in North America were sensitive to both the viscosity at the location of the observer as well as to the viscosity below the former load. This agrees with the finding that a 1D averaged Earth model is able to reproduce RSL results of a 3D model reasonably well below the load in Glacier Bay, but not in Central Oregon along the Pacific coast (*Bagge et al.*, 2021). *Yousefi et al.* (2018) confirmed that no 1D GIA model was able to fit all the RSL data along the Pacific coast, further emphasising the need for 3D models in this region. However, 3D models did not improve the fit here even though the predictions were significantly affected by lateral Earth structures variations (*Yousefi et al.*, 2021). RSL data along the Atlantic coast of North America are also sensitive to lateral Earth structure variations, especially in the North (*Love et al.*, 2016). Along the Atlantic coast of North America, 3D models did indeed improve the fit to RSL data (*Kuchar et al.*, 2019).

The horizontal GIA-related motions are shown to be very sensitive to lateral variations in Earth structure (e.g., *Gasperini et al.*, 1990; *Kaufmann et al.*, 2005; *Latychev et al.*, 2005; *O'Keefe and Wu*, 2002; *Steffen et al.*, 2006). In North America, the effect of such variations on the horizontal motion is the same magnitude as that of horizontal motions predicted by 1D GIA models (*Latychev et al.*, 2005). Within Scandinavia, 1D GIA models simulate horizontal motions outward from the Baltic Sea, but this diverging pattern is not found with 3D Earth models due to lateral viscosity variations in the transition zone (*Steffen et al.*, 2006). Furthermore, the horizontal motions in Antarctica are controlled by the different Earth structures in East and West Antarctica, and horizontal motions point from stiff East Antarctica to the weaker West Antarctica (*Kaufmann et al.*, 2005). Therefore, the sensitivity to 3D Earth structure needs to be considered when examining the horizontal motions of GIA.

Furthermore, modelling compressible deformation enhances horizontal deformation rates in Fennoscandia and Hudson Bay by a factor two (*Tanaka et al.*, 2011) as compared to modelling incompressible deformation, which is often simulated by GIA models to prevent model instabilities. I elaborate on compressibility in the next section.

(IN)COMPRESSIBILITY

Compressibility relates to the dilatation and compression of individual elements within a model (Figure 1.7). Numerical GIA models of horizontal motions are significantly altered by including compressibility (*James and Lambert*, 1993; *Johnston et al.*, 1997; *Mitrovica et al.*, 1994a; *Tanaka et al.*, 2011), and this is therefore a process that needs to be included in those models. However, including compressibility gives rise to the growth of unstable Rayleigh-Taylor modes (*Hanyk et al.*, 1999; *Plag and Jüttner*, 1995; *Vermeersen and Mitrovica*, 2000) complicating the inclusion of compressibility within GIA models. Assuming incompressibility reduces the complexity of the governing equations, but significantly changes the modelled horizontal motion.

A partial solution is to employ so-called material compressibility, which allows for material compression but does not include the internal buoyancy force (*Klemann et al.*, 2003). Because of the absence of the internal buoyancy force, unstable buoyancy forces related to density changes can not arise, and the model is no longer unstable. However, material compressibility only approximates compressible deformation for smaller

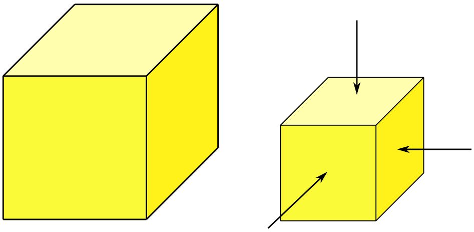

Figure 1.7: Schematic illustration of a) compressibility within elements of the GIA Earth model. The arrows denote forces acting on an element.

wavelength signals (*Tanaka et al.*, 2011).

Full compressibility (including the internal buoyancy force) has been included in several 3D GIA models. The first to do so were *Latychev et al.* (2005). Their model is based on finite volumes, and was only compressible for elastic deformation. *Zhong et al.* (2003) created a 3D GIA model in finite-element software CitcomS, which is augmented by *A et al.* (2013) for compressible deformation. A compressible spectral-finite element model is created by *Tanaka et al.* (2011), which is an extension of the incompressible spectral finite-element model of *Martinec* (2000). In this thesis, I opt to use a GIA model based on the finite-element model Abaqus, which is easily extendable to include non-linear 3D rheologies (Chapter 5, *van der Wal et al.*, 2015; *Wu and Wang*, 2008). The GIA model based on Abaqus developed by *Blank et al.* (2021) can be relatively easily adjusted for different study regions and has been coupled to a model for ice sheet dynamics in *Van Calcar et al.* (2023).

1.5. THESIS OUTLINE

This thesis contributes to the understanding of the deep Earth by using GIA models with static gravity and horizontal motion observations. I have listed a number of key questions derived from the state-of-the-art described in the previous sections. For the first key question, I focus on the negative gravity field anomaly centred over Hudson Bay in North America (circled by the red dashed line in Figure 1.2), and on the Earth structure and processes that explain it:

How can the long-wavelength gravity field of North America be modelled best?

I combine models for the Crust-Lithosphere-Asthenosphere with models for mantle convection and GIA in order to model the gravity field in this area, where I implement the models for mantle convection and GIA as dynamic contributions. This first key question is handled in Chapter 3. Next, I investigate the horizontal motion of GIA. Horizontal motions are found to be very sensitive to lateral Earth structure variations (e.g., *Gasperini et al.*, 1990; *Kaufmann et al.*, 2005; *Latychev et al.*, 2005; *O'Keefe and Wu*, 2002; *Steffen et al.*, 2006). I should therefore be able to include 3D Earth structure variations in our GIA model. Accurately modelling horizontal motion furthermore requires models to be compressible (Section 1.4). I aim to answer the following key question in Chapter 4:

> *How can the horizontal motions of GIA be modelled using 3D finite element models based on Abaqus?*

Due to the complexity of this problem, I start by developing models with a Cartesian geometry. We assess how well Cartesian models approximate the horizontal motions of spherical GIA models, and also investigate the approximation of incompressibility which is often employed in GIA models. Last, I zoom in on Alaska, a tectonically complex region subject to significant GIA (Section 1.2). Tectonic studies correct for GIA using models which do not allow for lateral variations in Earth structure and rheology, and are also not compressible (*Elliott and Freymueller*, 2020; *Elliott et al.*, 2010). The last key question is formulated as follows:

> *What is the effect of compressible 3D GIA models on the block model predictions in Alaska?*

By employing a compressible 3D GIA model, I test the impact of a more advanced GIA model on tectonic motion. This key question is investigated in Chapter 5, which results have direct implications for plate tectonics. The chapter consequently connects the research fields of GIA and tectonics. Chapter 6 summarises the conclusions and highlights recommendations for the future of GIA research on the gravity field and on horizontal motion.

2

METHODOLOGY

In this chapter, I explain the methodology that is used in Chapters 3 to 5. I start by explaining the models that I combine to simulate the long-wavelength gravity field of Chapter 3. In Chapter 4, I focus on simulating horizontal motion of GIA, and explain how the equations of motion are solved within finite-element software Abaqus. In this chapter, I also discuss two assumptions of GIA models and their effects on predicting realistic horizontal motions: the assumption of incompressibility, and approximating GIA with models of Cartesian geometry. Last, I explain the theory to understand the tectonic block models of Chapter 5.

2.1. MODELLING THE LONG-WAVELENGTH STATIC GRAVITY FIELD

In theory, the observed static gravity field over North America consists of contributions from surface layers, mantle convection, and glacial isostatic adjustment. I aim to replicate the observed static gravity field anomaly over Hudson Bay (Figure 1.2) by combining isostatic models for the upper layers (Crust-Lithosphere-Asthenosphere, hereafter CLA) with models for mantle convection and glacial isostatic adjustment as explained in Section 1.3.1. The combined model generates a 3D spherical density representation which is transformed to gravitational potential fields using a spectral method (*Root et al.*, 2016). I elaborate below on the GIA model, the application of isostasy and the mantle convection model. The GIA model is presented in Section 2.2.

2.1.1. THE CRUST-LITHOSPHERE-ASTHENOSPHERE MODEL

The first contribution is from density variations in the upper layers of the Earth which I combine in the Crust-Lithosphere-Asthenosphere (CLA) model. The CLA model creates spherical density layers, and converts those to SH coefficients of the gravitational potential (*Root et al.*, 2016). I use layer thicknesses and densities to create the spherical layers. A preset density is assigned to the layers between the surface and the bottom of the crust, the Mohorovičić discontinuity (hereafter: Moho). Between the Moho and the Lithosphere-Asthenosphere Boundary (LAB) the density is adjusted to fulfil the isostasy requirement (Section 2.1.2).

The crustal thickness is derived from active source seismics and receiver functions studies (*Laske et al.*, 2013). Below North America, the crustal thickness is close to the global average for continental crust and ranges from 30-50 km (*Laske et al.*, 2013; *Szwillus et al.*, 2019). I gather the crustal data from CRUST1.0 (*Laske et al.*, 2013), and also from the U.S. Geological Survey (USGS) Global Seismic Catalog (GSC) database to estimate the uncertainty in the adopted crustal model. CRUST1.0 contains crustal layer depths and crustal densities, while the dataset from GSC only contains the crustal thickness. In the latter case, a uniform crustal density of 2850 kg/m^3 is assumed, like in *Root et al.* (2017).

In this thesis, I use the depth of the Lithosphere-Asthenosphere Boundary (LAB) to further improve the spherical density profile. The LAB separates the conductive lithosphere from the convective asthenosphere. The lithosphere contains the crust and the uppermost part of the mantle. The thickness of the lithosphere is largest below cratons (up to 250 km, *Steinberger and Becker*, 2018). The central part of North America is underlain by a craton, and the lithosphere beneath Hudson Bay is therefore estimated to be relatively thick (150-200 km, *Eaton and Darbyshire*, 2010). The estimates of the LAB depth that are used in Chapter 3 are based on surface heat fluxes and crustal modelling (*Hamza and Vieira*, 2012), or on a joint inversion of surface waveform tomography, surface heat flow, and topography data (WINTERC, *Fullea et al.*, 2021). The lithospheric mantle density (between the Moho and the LAB) is assumed to be the most unknown parameter, and its density is retrieved by satisfying the requirement of isostasy (following Equation 3.4). The concept of isostasy is explained in the next section.

2.1.2. ISOSTASY

Topography calculated with upper layers in isostatic balance is a good approximation for the observed surface level in many areas on Earth (e.g., *Turcotte and Schubert*, 2002). Current density models for the crust and the lithosphere are not accurate enough for correcting the gravity (e.g., *Molnar et al.*, 2015). A common solution is to assume isostatic balance to determine the uncertain density in the lithosphere (like in *Root et al.*, 2015). Isostatic balance implies that at a certain compensation depth the overlying masses are equal laterally, and this can be enforced by changing layer thicknesses (*Airy*, 1855) or densities (*Pratt*, 1859). The crustal density is commonly smaller than the lithospheric density, and Airy proposed that mountainous areas had large crustal roots to compensate for the excess of mass. Pratt, on the other hand, hypothesised that mountains are compensated by less dense material below the surface.

In this thesis, I adopt the principle of lithospheric isostasy, in which the sub-crustal lithospheric density is adjusted to ensure laterally equal masses at the compensation depth (*Lachenbruch and Morgan*, 1990; *Root et al.*, 2017). The compensation depth is taken to be at 300 km depth. Any excess or insufficiency of mass at this depth is compensated by decreasing or increasing the lithospheric density, respectively, so that laterally the masses are uniform. This principle is illustrated in Figure 2.1.

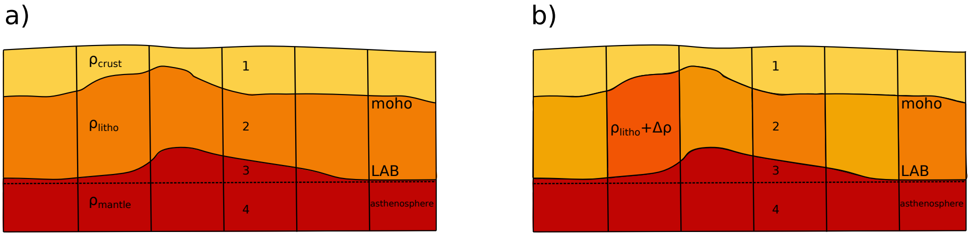

Figure 2.1: The principle of lithospheric isostasy, (a) the initial configuration and (b) the adjusted configuration. The dotted line denotes the compensation depth. Modified from Figure 4 of *Root et al.* (2017).

The dynamic processes of GIA and mantle convection are added to this isostatic model as bottom forces (Section 1.3.1). Mantle convection is included in the CLA model to determine the relative contribution of GIA to observed gravity anomalies. The processes of GIA and mantle convection are briefly described in the next sections. The reader is referred to Chapter 3 for specifics on the GIA and mantle convection models used.

2.1.3. MANTLE CONVECTION

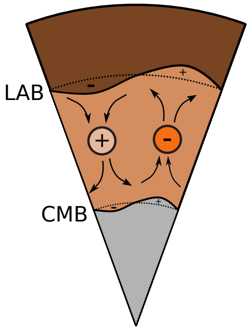

Figure 2.2: Mantle convection and its three contributions to the gravity field denoted by a plus or a minus sign.

There are three contributions of the mantle to gravity field anomalies. The first contribution is that of density anomalies in the mantle. A lighter particle results in less attraction than the average surrounding density, and therefore produces a negative anomaly in the gravity field. A heavier particle will generate more attraction and will be seen as a positive anomaly in the gravity field. These density anomalies cause movement within the mantle. A denser particle descends, and a lighter particle ascends. This causes the second and third contributions to the gravity field. The second contribution is that of deflections at the LAB. A lighter particle induces flow that deflects the LAB upwards, and causes the mantle material to be closer to the surface. The mantle material is more dense than that of the lithosphere above it, and therefore there is a net excess of mass and a positive contribution to the gravity field (Figure 2.2). The magnitude of the deflections of the LAB is mainly determined by the viscosity contrast between the upper and lower mantle (*Hager et al.*, 1985). The first and second contributions are usually opposite, as a lighter particle causes mantle material to be closer to the surface, and vice versa. The third contribution is that of deflection at the CMB, where, for upward deflection, the more dense core particles are now replacing lighter mantle particles. When realistic density and viscosity profiles are chosen, the resulting geoid predicted by models that incorporate all three effects is similar to the observed geoid signal for very long wavelengths ($\sim 11000-16000$ km, *Hager et al.*, 1985).

In Chapter 3, a spherical finite element code is used for modelling mantle convection (*Tosi*, 2008). This code solves the incompressible Stokes problem, using finite elements in the radial direction and spherical harmonics for the lateral dimensions. The model computes gravity anomalies from density anomalies and deflections at the surface and CMB. The surface deflections are calculated using the normal stress (σ_{rr}) on a free-slip boundary compensated for the mass excess or deficit of dynamical topography (*Flament et al.*, 2013):

$$\sigma_{rr} = \rho_{asth} g h_{dt}. \tag{2.1}$$

2.2. GLACIAL ISOSTATIC ADJUSTMENT MODEL

A model of Glacial Isostatic Adjustment (GIA) uses a forcing as input and simulates the response of the Earth to that forcing (Figure 2.3). The forcing is a surface load in the form of an ice model and accompanying sea level variations. The ice model defines the configuration of the ice sheet for fixed times, such as ICE-6G (Figure 1.1, *Argus et al.*, 2014; *Peltier et al.*, 2015). The ocean model prescribes the ocean loading, and resolves the height of the sea-level using the sea-level equation, an equation that calculates the changes in sea-level in response to changes in ocean and ice masses (*Farrell and Clark*, 1976). The sea-level height is defined here as the distance between the ocean surface and the solid Earth. Ice-mass changes deform the Earth's surface, and the deformations and the ice mass itself change the gravitational potential which determines the shape of the ocean's surface (defined by the geoid).

The response of the Earth to the forcing is determined by parameters inside the Earth such as the lithosphere thickness and the mantle viscosity. The lithosphere thickness causes a degree of smoothing in results for the vertical deformation, with reduced peak values for thicker lithospheres (*Wolstencroft et al.*, 2015). The mantle viscosity determines the time scale at which mantle flow takes place. A highly viscous mantle responds slowly to changes in ice sheet configurations, while a low viscosity mantle reacts faster. I can constrain both parameters using surface observations like those of the gravity field, and thereby attain new information about the Earth's interior. In Chapter 3, I use a GIA model that is based on the normal mode method (*Sabadini et al.*, 2016) which also solves for the sea-level equation. This model includes rotational feedback (*Milne and Mitrovica*, 1998; *Wu and Peltier*, 1984) and geocenter motion (*Greff-Lefftz and Legros*, 1997). It is a fast solution method that allows forward modelling of several combinations of upper and lower mantle viscosities, for an Earth that contains radially varying properties.

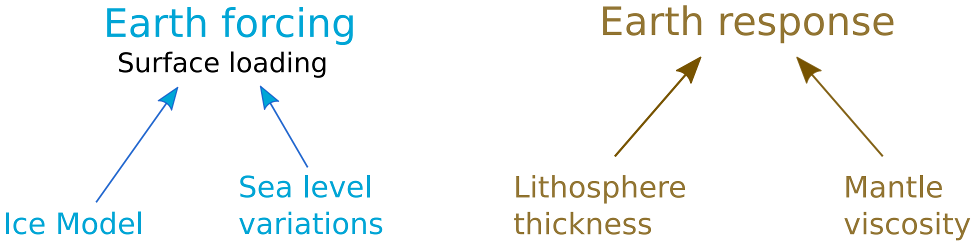

Figure 2.3: The important components of a GIA model. Adapted from Figure 15.10 of *Whitehouse et al.* (2021).

In Chapters 4 and 5, I employ and further develop a GIA model that is based on the finite-element method to investigate horizontal motions corresponding to GIA. A description of the steps to generate the models used in Chapers 4 and 5 is shown in Section 2.2.1. The horizontal motions of GIA are very sensitive to 3D variations in Earth structure (e.g., *Gasperini et al.*, 1990; *Kaufmann et al.*, 2005; *Latychev et al.*, 2005; *O'Keefe and Wu*, 2002; *Steffen et al.*, 2006). The developed model allows for 3D Earth structures, and can easily include other rheologies (Chapter 5, *van der Wal et al.*, 2015; *Wu and Wang*, 2008). It is applicable to GIA simulations for ice sheets smaller than 200 km in radius and does not include rotational feedback or geocenter motion. I develop this model using commercial finite-element software Abaqus (*Hibbitt et al.*, 2016). In sections 2.2.2 to 2.2.4, I explain how Abaqus solves the governing equations of GIA. I first derive the momentum equation for GIA, and after that describe how this equation is solved within Abaqus. I explain the limitations of the frequently employed solution method of (*Wu*, 2004), and discuss recently proposed alternative solution methods. Finally, I elaborate on the assumption of incompressibility, and also examine how well GIA is simulated with Cartesian models.

2.2.1. SETUP OF GIA MODELS IN ABAQUS

The finite-element models of Chapter 4 are created using 8-node brick elements of type C3D8H for incompressible models, and elements of type C3D8 for (material) compressible models. The models are generated using a high resolution in the center of the model, and a lower resolution outside of it. The elements in the high resolution area are roughly 27 × 27 km in size. Outside of this area, a horizontal resolution of 550 km is used. The high resolution area extends over an area of 4,400 × 4,400 km. The total width of the model is 20,000 km. Per layer, 141,376 elements are created. With 24 layers, in total 893,036 elements are generated for each model. The resolution in the finite-element models of Chapter 4 is explained in more detail in Section 4.3.4. The sides of the models are limited to vertical motion, so that no mass "leaves" the model during the simulation. The boundary conditions at the radial boundaries are stated in Section 4.2.1. The Abaqus models employed in Chapter 4 are benchmarked with the Earth model of *Spada et al.* (2011) using spherical finite-element code AFCAL, which has been benchmarked in *Martinec et al.* (2018), and FastLove-HiDeg, a code based on the normal mode method that has been verified in *Spada et al.* (2011). This benchmark test is shown in Section 4.9, and a brief recap of the results there is mentioned in the third paragraph of Section 4.3.2. Input files for the Abaqus models of this chapter are available as a published dataset at *https://doi.org/10.4121/9a9bdb35-8f65-41f1-be00-4d247722ad48*. These files were uploaded in 2023, when the paper for this chapter was published.

The finite-element models of Chapter 5 employ the same element types as the finite-element models of Chapter 4, which means that 8-node brick elements of type C3D8H are used to generate the incompressible models, and that element type C3D8 is used for the (material) compressible models. The finite-element models of Chapter 5 are generated with a high resolution area in the middle, surrounded by a low resolution area (just like in Chapter 4). The high resolution region is 1,425 by 2,325 km, and the total model width is 20,000 km. The elements in the high resolution area have a resolution of 15 × 15 km in the upper 90 km, and 75 × 75 km below that (as shown in Figure 2 of *Marsman et al.*, 2021). A total of 160,290 elements are created for a single model. This exact mesh is also used by *Marsman et al.* (2021), and is based on the setup of *Schotman et al.* (2008) and *Barnhoorn et al.* (2011). The only difference with the finite-element model of *Marsman et al.* (2021) is the bottom boundary, which in Chapter 5 is put at a depth of 2,891 km (at the core-mantle boundary), while the model of *Marsman et al.* (2021) extends to a depth of 10,000 km. More details on the model setup of Chapter 5 are described in Section 5.2.2. The boundary conditions of the finite-element models in this chapter are the same as for the finite-element models of Chapter 4. The finite-element models of Chapter 5 are tested against the model used by *Marsman et al.* (2021) in Section 5.6.

2.2.2. MOMENTUM EQUATION OF GIA

This momentum equation for external loading of a compressible Earth after linearisation and for hydrostatic balance is given by (e.g., *Wu and Peltier*, 1982):

$$\underbrace{\nabla\cdot\boldsymbol{\tau}}_{\text{Divergence of stress}} + \underbrace{\nabla\left(\vec{u}\cdot\rho_0 g_0 \hat{r}\right)}_{\text{Isostatic restoring force}} - \underbrace{\rho' g_0 \hat{r}}_{\text{Internal buoyancy force}} + \underbrace{\rho_0 \nabla\phi'}_{\text{Self-gravity}} = 0. \tag{2.2}$$

Here, $\boldsymbol{\tau}$ is the Cauchy stress matrix, $\vec{u}$ is the displacement vector, ρ_0 and g_0 are the hydrostatic background density and gravity, respectively, and $\hat{r}$ is the unit vector in the radial direction. ρ' refers to perturbations in density caused by the deformation, and ϕ' to perturbations in the gravitational potential resulting from the load and induced deformation and density changes, with $\nabla\phi = g$. Equation 2.2 involves four terms. The first term describes the divergence of stress. The second term represents an isostatic restoring force which restores equilibrium after the load has been removed or is stabilised. The third term denotes the internal buoyancy force which includes the effect of density perturbations in layers in the subsurface. These density perturbations are caused by dilatation or compression of individual elements, and are calculated using the mass conservation equation (e.g., *Backus*, 1967):

$$\rho' = -\nabla \cdot \left(\rho_0 \vec{u}\right). \tag{2.3}$$

The fourth term in Equation 2.2 relates to self-gravity which considers perturbations in the gravitational potential due to mass redistribution. The perturbed gravitational potential is calculated using Poisson's equation for gravity (e.g., *Wu and Peltier*, 1982):

$$\nabla^2 \phi' = 4\pi G \rho'. \tag{2.4}$$

Here, G is the gravitational constant.

2.2.3. SOLVING THE EQUATIONS IN ABAQUS

Abaqus solves the following equation:

$$\nabla \cdot \boldsymbol{\tau} + \mathbf{f} = 0. \tag{2.5}$$

In the absence of body forces ($\mathbf{f} = 0$), I arrive at Equation 1 of *Wu* (2004):

$$\nabla \cdot \boldsymbol{\tau} = 0. \tag{2.6}$$

Therefore, only the divergence of stress ($\nabla \cdot \boldsymbol{\tau}$) is automatically considered, and all other terms in Equation 2.2 need to be included explicitly. A frequently used method to solve for Equation 2.2 is described in *Wu* (2004), and is based on a stress transformation. Recently, additional methods of solving for GIA in Abaqus have been proposed, which either solve for the equation of motion numerically outside of the FE software (*Huang et al.*, 2023; *Wong and Wu*, 2019), or use a comprehensive stiffness matrix together with gravity (*Hampel et al.*, 2019). In this thesis, I employ the methods of *Wu* (2004) and *Hampel et al.* (2019), and therefore briefly recap them below.

METHOD OF *WU* (2004)

The method of *Wu* (2004) solves the governing GIA equations using the Coupled Laplace-Finite Elements method. In this method, a stress transformation is performed, which relates the initial stress tensor $\boldsymbol{\tau}$ to a perturbed stress tensor $\boldsymbol{t}$ plus an extra term for isostasy. The stress transformation is as follows:

$$\boldsymbol{t} = \boldsymbol{\tau} - \rho_0 g_0 u_r \boldsymbol{I}. \tag{2.7}$$

Here, $\boldsymbol{t}$ is the transformed stress tensor, $\boldsymbol{\tau}$ is the Cauchy stress tensor, and u_r the displacement in the radial direction. If I take the divergence of this transformed stress tensor, I obtain the term for the isostatic restoring force in Equation 2.2:

$$\nabla \cdot \boldsymbol{t} = \nabla \cdot \boldsymbol{\tau} - \rho_0 g_0 \nabla u_r. \tag{2.8}$$

Therefore, the isostatic restoring force is included if I perform this stress transformation. Now I only need to include the terms for internal buoyancy and for self-gravity, and the resulting equation of motion no longer contains a term for the force of isostasy:

$$\nabla \cdot \boldsymbol{t} - \rho' g_0 \hat{r} - \rho_0 \nabla \phi' = 0. \tag{2.9}$$

An assumption that is often used within GIA models is that of incompressibility (Section 1.4). *Wu* (2004) uses this assumption, which inhibits any density changes ($\rho' = 0$) causing the internal buoyancy force ($\rho' g_0 \hat{r}$) to disappear from the equation of motion. The last term in Equation 2.9 contains the perturbed potential, which is calculated using Poisson's equation (Equation 2.4). As incompressibility is assumed in this method, Poisson's equation for calculating the disturbing potential effectively becomes the Laplace equation (i.e. $\nabla^2 \phi' = 0$).

To recap, the restoring force of isostasy is included by performing a stress transformation, and self-gravity is solved for using Poisson's equation. The term for internal buoyancy force is no longer present as incompressibility is assumed.

The stress transformation performed in this method is only sufficient for incompressible models (*Bängtsson and Lund*, 2008). As compressibility enhances horizontal deformation rates by a factor two in Fennoscandia and the Hudson Bay (*Tanaka et al.*, 2011), other researchers continued to work on creating a finite element model in Abaqus that is able to solve for compressible deformation.

COMPRESSIBILITY IN ABAQUS

Several methods have been developed to simulate compressible deformation in Abaqus. One method was introduced by *Wong and Wu* (2019), which calculates the buoyancy force iteratively outside of the finite-element software. The drawback of their method was that it was at the time not applicable to realistic ice loads. *Huang et al.* (2023) extended this method, so that it is now applicable to realistic loadings. In Chapter 4 of this thesis, I solve for GIA using the approach presented in *Hampel et al.* (2019), which includes an explicit application of gravity and includes the change in forcing due to prior deformation. This method is relatively simple and elegant compared to the method described by *Wong and Wu* (2019), as in principle only a few extra lines of code are required to solve for compressible deformation. Therefore, it is potentially a good solution to the problem of including compressibility within GIA models of Abaqus. Chapter 4 also discusses this method in detail, but I provide a short summary below.

To explain the method presented in *Hampel et al.* (2019), I first have to explain how Abaqus solves for Equation 2.5. Abaqus does so by using the weak formulation, which is generated by multiplying the equation of motion with a test function. By doing so, the number of equations is reduced from three (one for each direction) to one. After some more algebra, Equation 2.5 is eventually transformed in an equation of the form

$$K_{MN}u_M = f_N, \tag{2.10}$$

where f_N is the force applied at node N, u_M is the displacement of node M, and K_{MN} is the stiffness matrix. An elaborate description of the steps to arrive at Equation 2.10 is shown in Appendix A of Chapter 4.

The method described in *Hampel et al.* (2019) solves for Equation 2.2 by performing a non-linear analysis. In such an analysis, the FE equations are solved using Newton's method which considers additional terms for the stiffness matrix K_{MN}:

$$K_{NM} = K^0_{NM} + K^\sigma_{NM} + K^L_{NM}. \tag{2.11}$$

Here, K^0_{NM} is the linear stiffness matrix, which is effectively what is included in linear analyses like that of *Wu* (2004). There are two extra terms: 1) the initial stress matrix K^σ_{NM} to include the effect of stress-stiffening, and 2) the load stiffness matrix K^L_{NM} to include the effect of gravity loading. The initial stress matrix is given by

$$K^\sigma_{NM} = \int_{V_0} \boldsymbol{\tau}^c : \partial_N \boldsymbol{\beta}_M dV_0, \tag{2.12}$$

where $\boldsymbol{\tau}^c$ is the conjugate of the stress, $\boldsymbol{\beta}_M$ the strain-displacement matrix, V_0 is the reference volume, and $\partial_N = \frac{\partial}{\partial u^N}$ which is the derivative with respect to the nodal displacements u^N. The load stiffness matrix is described by

$$K^L_{NM} = -\int_S \mathbf{N}^T_M \cdot \mathbf{Q}^S_N dS - \int_V \mathbf{N}^T_M \cdot \mathbf{Q}^V_N dV. \tag{2.13}$$

On the right hand side of Equation 2.13 are two terms, for the surface and volume load stiffness matrices, respectively. These matrices contain $\mathbf{Q}^S_N$ and $\mathbf{Q}^V_N$, which denote the variation of the surface and volume load vectors with the nodal variables. These variables are multiplied by the transpose of interpolation functions, $\mathbf{N}^T_M$.

These two extra matrices are only initialised in a large-displacement analysis. In order to include the effect of gravity, the value of the gravitational acceleration is explicitly applied to each layer of the model. An initial stress also needs to be applied to prevent any motion due to gravity loading, as well as a lithostatic bottom pressure. These are all adjustments that are relatively simple, and this therefore makes it an elegant and interesting method. So far, *Hampel et al.* (2019) has tested shallow (up to 100 km deep) Cartesian models containing at most two layers. The Cartesian model approximation is discussed in the next section.

2.2.4. CARTESIAN VERSUS SPHERICAL MODELS

In simple terms, Cartesian models can be seen as a box while spherical models also consider the curvature of the Earth (Figure 2.4). Cartesian models are often easier to employ as the governing equations are easier, and there is no direct need to include the sea level equation. Moreover, Cartesian models are able to investigate small regions with a higher resolution in a short computation time as compared to that of global spherical models. For these reasons, some Cartesian models have been employed in small study areas like Iceland, Patagonia, and Alaska (e.g., *Árnadóttir et al.*, 2009; *Ivins and James*, 1999; *Marsman et al.*, 2021). However, the Cartesian model approximation is no longer valid if I aim to simulate GIA on larger scales. Still, vertical deformation can be approximated well using Cartesian models for ice sheets roughly the size of the Scandinavian ice sheet (*Amelung and Wolf*, 1994; *Wu and Johnston*, 1998). In Chapter 4, I investigate the accuracy of the approximation of Cartesian models for horizontal deformation.

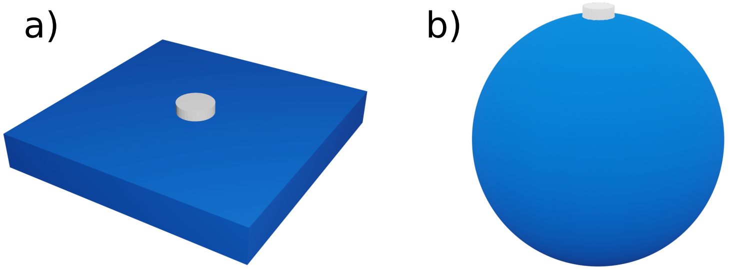

Figure 2.4: Schematic illustration of a) a Cartesian setup, and b) a spherical setup. The ice sheet is denoted in white as a circular disc.

2.3. TECTONIC BLOCK MODELS IN SOUTHEAST ALASKA

In this section, I discuss tectonic block models, which are used in Chapter 5 to infer plate velocities in Alaska (e.g., *Elliott and Freymueller*, 2020; *Elliott et al.*, 2010). To construct tectonic block models, a study area is divided in a number of blocks based on documented geologic evidence. Each block is then assigned a distinct Euler pole and angular velocity. An Euler pole is an imaginary pole around which a plate rotates with an angular velocity (Figure 2.5). The angular velocity of the rotation is constant around a single Euler pole, but depending on the distance to the rotation pole the absolute velocity can be larger or smaller. In other words, an Euler pole close to the measurement location requires small absolute velocities, but in locations that are further away from the Euler pole the absolute velocities are larger. This is why inferred surface velocities sometimes differ within a single tectonic block, like in Figure 8 of *Elliott et al.* (2010).

Chapter 5 discusses the plate motions in Southeast Alaska. This area is subject to significant glacial isostatic adjustment (e.g., *Larsen et al.*, 2005), a process that is independent of tectonic plate motions. The modelled GIA motions are therefore subtracted from the observed velocities before plate motions are derived. Studies on tectonic motions in Southeast Alaska currently correct the observed velocities for GIA using incompressible models that do not allow for lateral variations in the Earth structure. Chapter 5 will investigate if a more advanced GIA model impacts plate motions in this area.

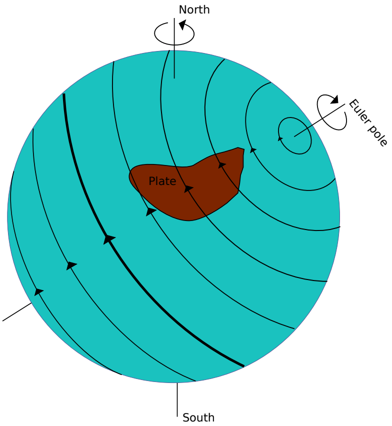

Figure 2.5: Schematic illustration of a plate rotating around its Euler pole. The arrows denote the rotation.

3

LONG-WAVELENGTH GRAVITY FIELD CONSTRAINT ON THE LOWER MANTLE VISCOSITY IN NORTH AMERICA

Abstract

The long-wavelength negative gravity anomaly over Hudson Bay coincides with the area depressed by the Laurentide ice sheet during the Last Glacial Maximum, suggesting that it is, at least partly, caused by Glacial Isostatic Adjustment (GIA). Additional contributions to the static gravity field stem from surface dynamic topography, Core-Mantle Boundary (CMB) topography, and density anomalies in the subsurface. Previous estimates of the contribution of GIA to the gravity anomaly range from 25 percent to more than 80 percent. However, these estimates did not include uncertainties in all components that contribute to the gravity field. In this study, we develop a forward model for the gravity anomaly based on density models and dynamic models, investigating uncertainty in all components. We derive lithospheric densities from equilibrium constraints, but extend the concept of lithospheric isostasy to a force balance that includes the dynamic models. The largest uncertainty in the predicted gravity anomaly is due to the lower mantle viscosity; uncertainties in the ice history, the crustal model, the lithosphere-asthenosphere boundary and the conversion from seismic velocities to density have a smaller effect. A preference for lower mantle viscosities $> 10^{22}$ *Pa s is found, in which case at least 60 percent of the observed long-wavelength gravity anomaly can be attributed to GIA. This lower bound on the lower mantle viscosity has implications for inferences based on models for mantle*

This chapter is published as Reusen, J. M., Root, B. C., Szwillus, W., Fullea, J., & van der Wal, W. (2020). Long-wavelength gravity field constraint on the lower mantle viscosity in North America. Journal of Geophysical Research: Solid Earth, 125(12), e2020JB020484.

convection and GIA.

Plain Language Summary

About 26 thousand years ago, vast parts of North America and Northern Europe were covered by ice sheets. These glaciations depressed the ground, which has been rebounding ever since the ice sheets started melting. The rate of this rebound depends on the structure of the earth below it. In this paper, we obtain more insight into the structure of the earth. To do so, we use the gravitational field, since we can observe small deviations in this field very precisely. Over Hudson Bay, we observe such a deviation. The observed gravity anomaly over Hudson Bay closely resembles the area previously covered by ice. One possible explanation for this anomaly is therefore the incomplete rebound of the land. To test this, we include the effects of previous glaciations and mantle flow in a model of the crust and the lithosphere. We vary the viscosities of the upper and lower mantle, which are important parameters when modelling glacial rebound and mantle flow. The best match is found for a stiff lower mantle, implying that at least 200 meters of land uplift remains and that a minimum of 60 percent of this anomaly can be attributed to the depression caused by past glaciations.

3.1. INTRODUCTION

The global gravity model XGM2016 exhibits a negative anomaly of about 50 mGal near Hudson Bay for wavelengths larger than 600 km (Figure 3.1) (*Pail et al.*, 2018). The shape of this anomaly resembles the contours of the deflection due to the former Laurentide ice sheet. Hence, the anomaly is thought to be caused by the incomplete rebound following the deglaciation of the Laurentide ice sheet (*Kaula*, 1972; *Walcott*, 1973), a process known as glacial isostatic adjustment (GIA). Because of incomplete GIA, the topography is not in equilibrium, and this topographic deflection can be seen in the gravitational potential field, hereafter referred to as the gravity field, or rather in anomalies of this field with respect to the gravity field of a reference Earth for which we use gravity anomalies. If GIA were the only cause for the gravity anomaly, the observed gravity anomaly with its small error would form a useful constraint on GIA models. However, the gravity field contains contributions from the crust, the lithosphere, the mantle, and GIA. Before using the gravity anomaly to constrain GIA, these contributions need to be quantified.

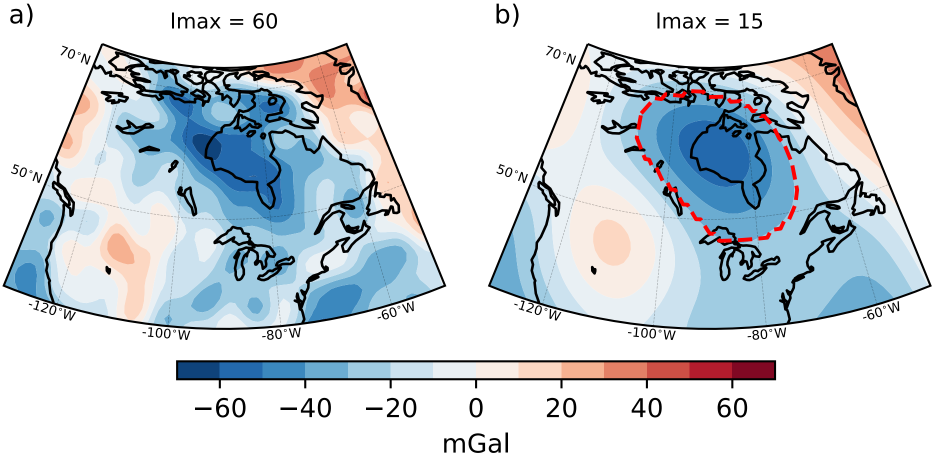

Figure 3.1: The gravity field of XGM2016 (*Pail et al.*, 2018) over North America up to degree 60 (a) and up to degree 15 (b). The study area is indicated by the dashed red line, which contains the points where the value is at least 50 percent of the peak value.

The crustal and lithospheric contributions to the gravity field are from density contrasts at geological boundaries. One of these density contrasts marks the boundary between the crust and the mantle, the Moho. Knowledge of the geometry of this boundary is therefore important for gravity modelling. A second boundary is the lithosphere-asthenosphere boundary (LAB), which can be defined as a boundary separating the conductive and convective regimes (e.g., *Eaton et al.*, 2009; *Fischer et al.*, 2010; *Sleep*, 2005). This boundary is not characterised by a large jump in density, but determines where the mantle can start to flow to equalise the weight of the overlying material. The LAB is therefore an important boundary for the force balance in the upper mantle, and can be inferred from estimates of, among others, heat flow or seismic tomography (*Afonso* *et al.*, 2019; *Eaton et al.*, 2009). Beneath Hudson Bay, the lithosphere is cratonic and has a thickness of 150-200 km (*Eaton and Darbyshire*, 2010).

Another factor determining the gravity field contribution of the crust and the lithosphere is isostasy. Isostasy implies that the pressures at a certain depth are equal. For example, the crustal thickness, which delivers the buoyancy to maintain the topography, can be determined in the classical Airy isostasy theory (crustal isostasy; *Watts*, 2001). In other studies, isostasy is calculated based on a lithosphere floating on top of a homogeneous asthenosphere (lithospheric isostasy; *Lachenbruch and Morgan*, 1990). Isostasy is often a necessary assumption to be able to fit the observed gravity anomaly, also for North American studies (e.g., *Métivier et al.*, 2016). However, lithospheric isostasy neglects forces from the mantle. Here, we will extend the lithospheric isostasy to include forces from GIA and convection models, which are expected to play a significant role in North America.

Mantle contributions to the gravity field consist of (i) density anomalies in the mantle, (ii) surface dynamic topography (*Hager et al.*, 1985) and (iii) topography of the Core-Mantle Boundary (CMB). (ii) and (iii) depend on the viscosity contrast between upper and lower mantle; a smaller contrast results in a larger signal for the surface dynamic topography, while the signal is smaller for the CMB topography. (i) and (ii) have opposite sign; a positive density anomaly drags the surface down, resulting in negative dynamic topography which counteracts the positive gravity anomaly from the density anomalies. The lower boundary of the mantle marks the largest density contrast in the Earth, larger than the density contrast at the surface. Only long wavelength surface features are affected by CMB topography, and for these wavelengths it is hence important to include (iii). The long wavelength signal in the gravity field and the geoid can be matched well by mantle convection modelling using seismic tomography as input for the mantle density distribution (*Hager et al.*, 1985). For North America, the main mantle signal that is expected is that of the subducted Farallon slab, of which the geometry and subduction history are complex (*Sigloch*, 2011).

The GIA contribution to the gravity field is mostly dependent on the ice sheet history and on the viscosity of the Earth's mantle. The ice thickness controls the magnitude of the deflection, while the viscosity controls how fast the equilibrium is reached. A large viscosity leads to a smaller displacement during the loading phase, as compared to low viscosities, and also to a slower rebound after removal of the load. Meanwhile, in a low viscosity mantle, the deflection during loading is larger, but a fast relaxation after unloading can also lead to a small remaining displacement. Because of this, there are often multiple solutions of the viscosity for the same displacement. This explains part of the differences in viscosity profiles obtained in different studies.

Previous studies attribute different percentages of the gravity anomaly to GIA (e.g., *Métivier et al.*, 2016; *Paulson et al.*, 2007). This discrepancy can to a large extent be explained by different assumptions of the underlying mantle viscosity, and whether GIA and surface dynamic topography, as well as crustal and mantle density variations are considered in the modelling or data correction. The first studies that try to explain the gravity anomaly over Hudson Bay note that it can not be explained by GIA using a lower mantle viscosity of 10^{21} Pa s, and suggest by inference that the major contribution is that of mantle convection (*Cathles*, 1975; *James*, 1992; *Peltier et al.*, 1992). *Simons and Hager* (1997) find that the GIA contribution is significant and that about 50 percent of the free-air gravity anomaly can be explained by GIA. In their study, they employed a lower mantle viscosity that is close to 10^{22} Pa s. *Tamisiea et al.* (2007) used time-variable gravity from the GRACE mission to isolate the GIA signal and found viscosities between 10^{21} and 10^{22} Pa s. Consequently, they attribute only 25-45 percent of the free-air gravity anomaly to GIA. Finally, *Métivier et al.* (2016) investigated gravity, together with gravity gradients, by combining a lithospheric model with models for GIA and mantle convection, and found values of at least 10^{22} Pa s. In their study, GIA contributes more than 80 percent. All in all, the contribution of GIA to the gravity anomaly is still uncertain, with most recent estimates ranging from 25-45 percent (*Tamisiea et al.*, 2007) to more than 80 percent (*Métivier et al.*, 2016), with part of the spread explained by the unknown mantle viscosity.

The mantle viscosity is not well constrained and many studies have attemped to determine its value by employing constraints on mantle convection models (e.g., *Soldati et al.*, 2009; *Steinberger and Calderwood*, 2006), GIA models (e.g., *Paulson et al.*, 2007; *Wu and Peltier*, 1983) or a combination of both (*Forte and Mitrovica*, 1996; *Mitrovica and Forte*, 2004). Mantle convection studies that determine the viscosity are often global studies employing a radial viscosity profile containing many layers. These global inferences of the viscosity generally favour lower mantle viscosities > 10^{22} Pa s (e.g., *Bower et al.*, 2013; *Perry et al.*, 2003; *Steinberger and Calderwood*, 2006). GIA studies have been performed on both a global and regional scale, and generally use relative sea level (RSL) data and geodetic data to constrain the viscosity. No consensus has been reached on the value of the viscosity in the lower mantle under North America, with values varying by two orders of magnitude (10^{21}-10^{23} Pa s) (e.g., *Métivier et al.*, 2016; *Paulson et al.*, 2007).

Dynamic models (i.e. the mantle convection model and the GIA model) contain more uncertain parameters than the viscosity. One of these parameters is the ice history, to which the gravity field is especially sensitive at the margin of ice sheets (*Mitrovica et al.*, 1994b; *Wu*, 2006). However, the extent of the Laurentide ice sheet is relatively well known, in contrast to its thickness (*Stokes*, 2017). Uncertainty due to the ice history has been included in some previous studies of the gravity field (*James*, 1992; *Métivier et al.*, 2016), but not in all (*Peltier et al.*, 1992; *Tamisiea et al.*, 2007). For mantle convection modelling, density anomalies are needed, which are commonly derived from seismic velocity anomalies. The conversion factor between velocity anomalies and density anomalies can vary between 0.2 and 0.4 (*Karato*, 1993; *Trampert et al.*, 2004), as determined by measurements and employed in convection models (*Steinberger and Calderwood*, 2006). This conversion factor can have a large influence on the resulting gravity, as it can amplify or minimize gravitational signals from the mantle. *Métivier et al.* (2016) assign a conversion factor to each viscosity layer in their mantle models, but do not show the sensitivity to this parameter.

We combine contributions from a crust-lithosphere-asthenosphere (CLA) model, mantle densities, and CMB topography in a forward model, and vary parameters of all components. If all geometries and densities would be perfectly known, this would be able to explain the observed gravity anomaly. However, the assumption of a force balance is required to compute the densities in the CLA model. We include GIA and surface dynamic topography in the force balance for North America, which we argue is the way to include all model components consistently.

Viscosity controls the contribution from the dynamic models to the force balance, and the contribution of CMB topography. In the presence of other uncertainties, viscosity is the most important parameter, and we are able to constrain it from fitting the observed gravity field. From this viscosity, we obtain the contributions of GIA and mantle convection to the gravity anomaly.

Section 3.2 explains the approach used to construct the density model of the crust-lithosphere-asthenosphere and its conversion to gravity anomalies. After that, we elaborate on the GIA and mantle convection models used and how they are included in the isostatic balance of the crust-lithosphere-asthenosphere. Section 3.3 starts by investigating the effect of uncertainty of the crustal and lithospheric model on the modelled gravity field. Next, we show the GIA and mantle contributions to the gravity field as a function of the viscosity profile. After this, we discuss uncertainties due to the ice history and due to the conversion from seismic velocities to density. We find the best fitting solution for an earth model with varying upper- and lower mantle viscosity, and obtain a lower bound on the lower mantle viscosity.

3.2. METHODOLOGY

In this section, we start by stating the complete model used in this study. The top layers are the crust, lithosphere, and asthenosphere. Second, we explain how GIA and surface dynamic topography are incorporated in our crust-lithosphere-asthenosphere model using isostatic equilibrium. After that, we elaborate on the crust-lithosphere-asthenosphere models, the mantle models, and the GIA models. It is not our aim to explain small-scale features in the data, and we would not be able to do so with the current models. We therefore set a maximum spherical harmonic degree for the data-model comparison and explain the reason for this choice of maximum degree at the end of Section 3.2.6.

3.2.1. THE COMPLETE MODEL

Our forward model includes the gravity field (Δg) of a CLA model, mantle density anomalies below 300 km (ρ_m), and topography at the CMB:

$$\Delta g_\mathrm{tot} = \Delta g_\mathrm{CLA} + \Delta g_{\rho\mathrm{m}} + \Delta g_\mathrm{CMB} \tag{3.1}$$

Note that the signal of GIA and surface dynamic topography do not appear explicitly in Equation 3.1. These non isostatic pressures are included in the isostatic balance of the crust-lithosphere-asthenosphere model (Section 3.2.2). The mantle density anomalies are derived from seismic velocity anomalies, see Section 3.2.4. The gravity signal from the topography at the CMB is computed by a mantle convection model (*Tosi*, 2008).

It might seem contradictory that the influence of GIA is not explicit in Equation 3.1, yet we are able to constrain its contribution to the gravity field. The explanation is that the GIA contribution is determined by viscosity, which controls the contribution of mantle in the last term of Equation 3.1, but also the contributions of GIA and surface dynamic topography in the force balance that is employed for the CLA model as will be explained in Section 3.2.2. Thus, a data-model comparison allows us to constrain the viscosity, and with the viscosity we are able to retrieve the contribution of GIA and mantle convection to the gravity field.

For Equation 3.1, the gravity anomaly needs to be computed for layers of arbitrary density. To do this, we use a spectral method that transforms 3D spherical density models into spherical harmonic coefficients of the gravitation potential (*Root et al.*, 2016), and employ the SHTools package (*Wieczorek and Meschede*, 2018) to convert the coefficients to gravitational potential fields in the spatial domain. We calculate the gravity anomaly at a height of 6738 km, the height at which XGM 2016 is calculated.

Although the geoid is commonly used, we opt to show gravity anomalies, which is the radial derivative of the gravity potential. Our choice to represent the gravity field is in principle arbitrary for the long-wavelengths that we employ in this study. Strictly speaking, we are computing gravity disturbances, these disturbances are referred to as gravity anomalies in this study.

3.2.2. ISOSTASY IN THE CRUST-LITHOSPHERE-ASTHENOSPHERE MODEL

In principle, the gravity field can be represented by geometry and density information of each layer in the sub-surface. In practice, accurate density information is not available at each depth, and the assumption of isostasy is made to solve for densities or geometry. In this study, we employ lithospheric isostasy (*Lachenbruch and Morgan*, 1990; *Root et al.*, 2017), which involves adjusting the density of the lithosphere. In an isostatic balance, no dynamic processes should be present. However, the dynamic forces of GIA and surface dynamic topography are acting on the bottom of our CLA model, so we need to correct for those. We present a consistent way of including information from crustal models, isostasy, and GIA and surface dynamic topography models.

To implement lithospheric isostasy, free body diagrams are made for mass columns up to 300 km (Figure 3.2). The forces involved are those caused by the weight of the crust, lithospheric mantle, and asthenosphere, and we implement GIA and surface dynamic topography as radial forces acting at 300 km. The pressure at 300 km depth for each column should equal that exerted by a reference column. Here, the reference column consists of a 30 km thick crustal layer and a 270 km thick mantle layer with densities of 2850 kg/m^3 and 3300 kg/m^3, respectively (Figure 3.2). Equilibrium of the forces is then achieved in the following manner:

$$F_{\mathrm{crust}} + F_{\mathrm{litho}} + F_{\mathrm{asth}} - F_{\mathrm{GIA}} - F_{\mathrm{DT}} = F_{\mathrm{ref}} \tag{3.2}$$

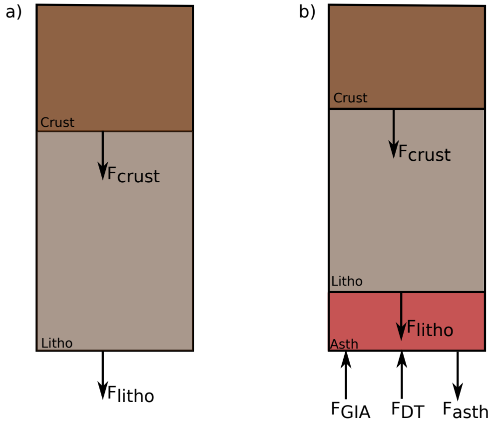

Figure 3.2: The forces involved in the reference column (left) and in our model (right). The forces exerted by the crustal, lithospheric and asthenospheric layers are denoted by F_{crust}, F_{litho} and F_{asth}, respectively. F_{GIA} and F_{DT} are the forces due to GIA and surface dynamic topography.

For each layer the pressure at 300 km can simply be calculated from its weight per area. To include surface dynamic topography, we calculate the radial stress caused by this process (*Flament et al.*, 2013):

$$\sigma_{\mathrm{rr}} = \rho_{\mathrm{asth}} g h_{\mathrm{DT}}, \tag{3.3}$$

and add it to the force balance of Equation 3.2. The density (ρ_{asth}) is that of the asthenosphere and equal to 3300 kg/m^3, g is the average value of the gravity, and h_{DT} is the height of the surface dynamic topography. σ_{rr} is calculated by the mantle convection model (*Tosi*, 2008), discussed in Section 3.2.4.

In principle, the contribution of GIA above 300 km is already included in the geometry of the crust and lithosphere, because their boundaries are deflected by GIA. However, GIA below 300 km plays a role through the stress that acts at the bottom of our CLA model, similar for the surface dynamic topography. These stresses affect the isostatic balance, so we include stresses from both GIA and surface dynamic topography in the isostatic balance to create a force balance (Equation 3.2). Following the approach of *Root et al.* (2015), we implement the effect of GIA by shifting the layers above 300 km according to the respective GIA deflection at the surface, h_{GIA}, defined positive upwards. This way, we assume isostasy based on a configuration in which GIA is no longer present. h_{GIA} is calculated by the GIA model, discussed in Section 3.2.5, and is taken to be the same for all elastic layers, which are the lithospheric layers conform to *Root et al.* (2015).

Combining these ideas in the force balance (Equation 3.2), assuming constant gravity in the top 300 km yields:

$$
\begin{aligned}
&\underbrace{\sum_{\mathrm{i}} \rho_{\mathrm{crust,i}} \left[(r_{\mathrm{i}} - h_{\mathrm{GIA}})^3\right]_{r_{\mathrm{lb,i}}}^{r_{\mathrm{ub,i}}}}_{\text{Crustal Columns}} + \underbrace{\left(\rho_{\mathrm{litho}} + \Delta\rho\right)\left[(r - h_{\mathrm{GIA}})^3\right]_{r_{\mathrm{LAB}}}^{r_{\mathrm{Moho}}}}_{\text{Lithospheric column}} \\
&+ \underbrace{\rho_{\mathrm{asth}}\left[(r_{\mathrm{LAB}} - h_{\mathrm{GIA}})^3 - (r_0 - 300\mathrm{km})^3\right]}_{\text{Asthenospheric column}} - \underbrace{\rho_{\mathrm{asth}}\left[(r + r_0)^3\right]_0^{h_{DT}}}_{\text{Surface dynamic topography column}} \qquad (3.4) \\
&= \underbrace{\sum_{\mathrm{j}} \rho_{\mathrm{ref,j}}\left[r_{\mathrm{j}}^3\right]_{r_{\mathrm{ref\,lb,j}}}^{r_{\mathrm{ref\,ub,j}}}}_{\text{Reference column}}
\end{aligned}
$$

The summation i is over all the crustal layers defined in the crustal model, where $r_{\mathrm{ub,i}}$ and $r_{\mathrm{lb,i}}$ are the upper and lower boundary of layer i, respectively, and $\rho_{crust,i}$ is the crustal density for the layer, which can vary laterally. An earlier version of this equation, without the processes of GIA and surface dynamic topography, is shown in *Root et al.* (2017). The first, second, and third term on the left-hand side of the equation represent the crustal, lithospheric, and asthenospheric layers in the model, respectively, and the right-hand side represents the reference column. r_0 is equal to 6371 km, the radius of the Earth. The radii to the Moho and the topographic boundaries are defined positive upwards. We assume that the geometry and density of the crust are reasonably well known from seismic data compared to deeper layers. However, deriving density from seismic models in the asthenosphere does not result in a good fit with gravity data. Therefore, isostasy is used as constraint to achieve a density model that provides a good fit with gravity. From this constraint, we can only constrain one parameter. Even if there would be reliable density information from seismic models, there would be a strong trade-off effect between different LAB or asthenosphere density and obtained lithospheric density. In the end, we opt to adjust the density of the mantle lithosphere, which is less well known, and is represented by $\Delta\rho$ in equation 3.4. It is important to note that the GIA contribution to the first four terms contains the entire GIA contribution (*Root et al.*, 2015). Boundaries below 300 km have a smaller density change and/or a smaller deflection and these are neglected. Similarly, the fourth term contains all of the effect of surface dynamic topography. This term is negative, because σ_{rr} is defined positive upwards in equation 3.3, and, consequently, the direction of this load is opposite that of the gravitational loads. Thus, a positive surface dynamic topography contribution results in an effective negative mass that will be compensated because of the pressure balance represented by Equation 3.4.

To recapitulate, the force balance (Equation 3.2) is transformed into a pressure balance. We can do so, because the area of the model columns is the same as that of the reference column. Assuming that gravity is constant for all layers in the crust-lithosphere-asthenosphere model, we obtain the pressure balance shown in Equation 3.4.

3.2.3. CRUST, LITHOSPHERE, AND ASTHENOSPHERE MODELS

The CLA model relies on seismic information for crustal thickness, crustal densities, and an LAB estimate, together with the lithospheric densities obtained in Section 3.2.2. To account for uncertainty in the crustal thickness, two crustal models are used: CRUST1.0 (*Laske et al.*, 2013) and a crustal model based on the U.S. Geological Survey (USGS) Global Seismic Catalog (GSC) database, which was interpolated to a 1x1° grid using kriging interpolation (*Szwillus et al.*, 2019). This dataset has been augmented over North America with data from the Geological Survey of Canada (*Schetselaar and Snyder*, 2017), and will be named GSCaug hereafter. CRUST1.0 has a resolution of 1x1° and each cell has a unique 8 layer density profile profile. The GSCaug dataset only presents the Moho depth. We adopt a crustal density of 2850 kg/m^3 for the GSCaug dataset, based on the reference profile described in Section 3.2.2. For both crustal models, the topography, bathymetry and ice-cover are taken from CRUST1.0, as uncertainties in these components are negligible for the long wavelength signal studied in this article. Moho depths of the crustal models are shown in Figure 3.3a and 3.3b. In oceanic areas, the Moho depth is 20 km at most. The Moho depth is clearly larger for continental areas, with values of 30 to 50 km. Around Hudson Bay, there are regional differences of up to 10 km between the crustal models. CRUST1.0 is used as the default crustal model in the rest of the analysis. This is different from *Métivier et al.* (2016), in which an isopycnal configuration of the crust was used.

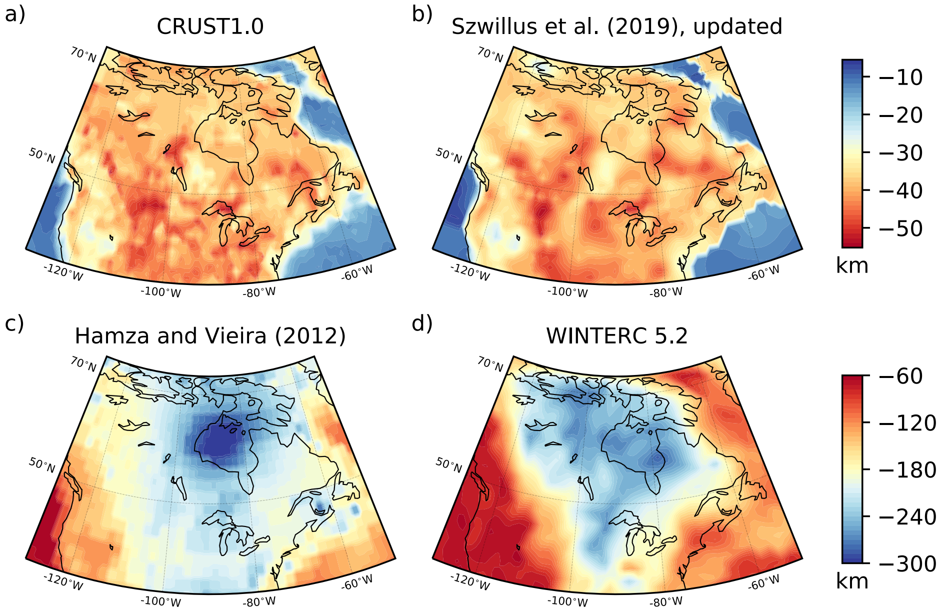

Figure 3.3: Moho depth of a) CRUST1.0 (*Laske et al.*, 2013), and b) an augmented version of the Moho model compiled by *Szwillus et al.* (2019), as well as the LAB depth of c) *Hamza and Vieira* (2012), and d) WINTERC v5.2.

The lithosphere and the asthenosphere are separated by the LAB. To account for uncertainty in this depth we use two estimates for the LAB (Figure 3.3c and 3.3d). The first option is the LAB model of *Hamza and Vieira* (2012), a model that is derived from estimates of surface heat fluxes and crustal modelling. The second option is obtained from WINTERC v5.2, which is a 3D model of the lithosphere and the upper mantle based on a joint-inversion of surface wave form tomography, surface heat flow, and elevation of the topography. In both models, the LAB reaches its largest depth in an area below Hudson Bay, thereby correlating with the observed gravity anomaly. In the LAB model compiled by *Hamza and Vieira* (2012), the LAB low over Hudson Bay is more confined and larger in amplitude than the WINTERC LAB.

We have used the LAB from *Hamza and Vieira* (2012) as our reference model, and the LAB estimate from WINTERC v5.2 as our alternative model, in the remainder of this study. However, the LAB from *Hamza and Vieira* (2012) is probably not well constrained, since estimates of surface heat fluxes form a poor constraint in terms of sparsity and error. However, since there is no real density jump at the LAB, we do not expect large changes in the gravity field as a result of the choice here. The sensitivity to this choice is investigated more thoroughly in Section 3.3.

3.2.4. MANTLE BELOW 300 KM

The contributions of the mantle below 300 km are computed using a mantle convection model (*Tosi*, 2008). This spectral finite element code solves the incompressible Stokes problem and computes the gravity field resulting from density anomalies and boundary deflections. For the radial direction, the model employs finite elements, while for the angular direction spherical harmonics are used to parameterise the solutions to the Stokes problem. The model uses mantle density anomalies as input, and produces dynamic topography at the surface (*Hager et al.*, 1985) and at the CMB. It is assumed that convection is only driven by density perturbations below 300 km.

The density anomalies are in turn derived from seismic velocity anomalies. Here, the seismic velocity anomalies are taken from the global, composite tomography model SMEAN2, which uses the approach of *Becker and Boschi* (2002) to combine S40RTS (*Ritsema et al.*, 2011), GyPSUM-S (*Simmons et al.*, 2010) and SAVANI (*Auer et al.*, 2014). There is uncertainty inherent in the choice of tomography model. However, SMEAN2 is an aggregate of multiple tomography models, and *Becker and Boschi* (2002) show that the tomography models correlate for long wavelengths. Moreover, SMEAN2 is an aggregate of multiple tomography models. We assume the uncertainty is smaller than the uncertainty in conversion factor (Equation 3.5) and effect are partly compensated by varying the conversion factor. Shear-wave velocity anomalies (Δv) can be converted to density anomalies ($\Delta\rho$) by a conversion factor (p) (*Karato*, 2008):

$$\frac{\Delta\rho}{\rho} = p\frac{\Delta v}{v}. \tag{3.5}$$

In this study, the conversion factor has a constant value of 0.15. In reality, the conversion factor can change radially (*Karato*, 2008; *Steinberger and Calderwood*, 2006) and laterally, but a single value is sufficient if the sensitivity to the parameter is small. The uncertainty introduced by the conversion factor is analysed in Section 3.3. We do not include a transition zone, due to trade-off effects which allow both low and high viscosity in the transition zone to fit the geoid (*King*, 1995). The layering is the same as the GIA model, in which trade-off effects are perhaps even stronger (*Paulson et al.*, 2007). The converted density anomalies, together with a three-layered viscosity profile (elastic lithosphere, upper mantle, and lower mantle), are used as input in the mantle convection code. The lithosphere is assumed to have a thickness of 100 km. In 3.5, we investigate the sensitivity to the lithospheric thickness in the mantle convection model. The viscosities of the upper and lower mantle are separated by the 670 km discontinuity. The density of the core is assumed to be homogeneous and is set equal to 4500 kg/m^3. The CMB and the Earth's surface are modelled as free-slip, impermeable boundaries. The output of the mantle convection code consists of stresses at the top and bottom boundaries. The stresses are converted to surface dynamic topography values with Equation 3.3. After, the surface dynamic topography is converted to pressure to compute lithospheric density anomalies in order to fulfil isostatic balance in the crust-lithosphere-asthenosphere model using Equation 3.4. The mantle density anomalies and the CMB topography are converted to spherical harmonic coefficients following the approach of *Root et al.* (2017), and these coefficients are added to the coefficients from the crust-lithosphere-asthenosphere model, as shown in Equation 3.1.

3.2.5. GIA MODELS

The GIA response to the glacial loading is calculated with a normal mode method (*Wu and Peltier*, 1982) for radial variations in viscosity within a multilayer model (*Vermeersen and Sabadini*, 1997) with self-consistent sea levels (*Mitrovica and Peltier*, 1991a). Rotational feedback (*Milne and Mitrovica*, 1998; *Wu and Peltier*, 1984) and geocenter motion (*Greff-Lefftz and Legros*, 1997) are incorporated in the model. Since we will only look at degrees 2 to 15, as will be shown in Section 3.2.6, the direct effect of geocenter motion will drop out, but any coupling to higher terms through the sea level equation, although small, is included. The code is developed by *Schotman* (2008) and has recently been benchmarked for simple loading scenarios in *Martinec et al.* (2018). In general, viscosity in GIA models can vary radially (1D) or in both the radial and lateral directions (3D). GIA models with a 1D viscosity in North America match results from laterally averaged 3D models reasonably well (*A et al.*, 2013). Moreover, the effect of 3D viscosity on predictions around Hudson Bay is limited (*Li et al.*, 2020). Therefore, it is expected that the 1D Earth model employed in our model produces reasonably accurate results.

The GIA model adopts a similar 3-layer Earth model as the mantle convection code discussed in Section 3.2.4, consisting of an 80 km thick, elastic lithosphere and a viscous upper (<670 km) and lower (>670 km) mantle. 2 viscous layers in the mantle provides sufficient degrees of freedom to model GIA observables (*Paulson et al.*, 2007). Therefore, we do not consider separate layers to model shallower phase transitions. The elastic parameters are obtained from the Preliminary Reference Earth Model (PREM; *Dziewonski and Anderson*, 1981) and are the same as in *van der Wal et al.* (2009). This lithospheric

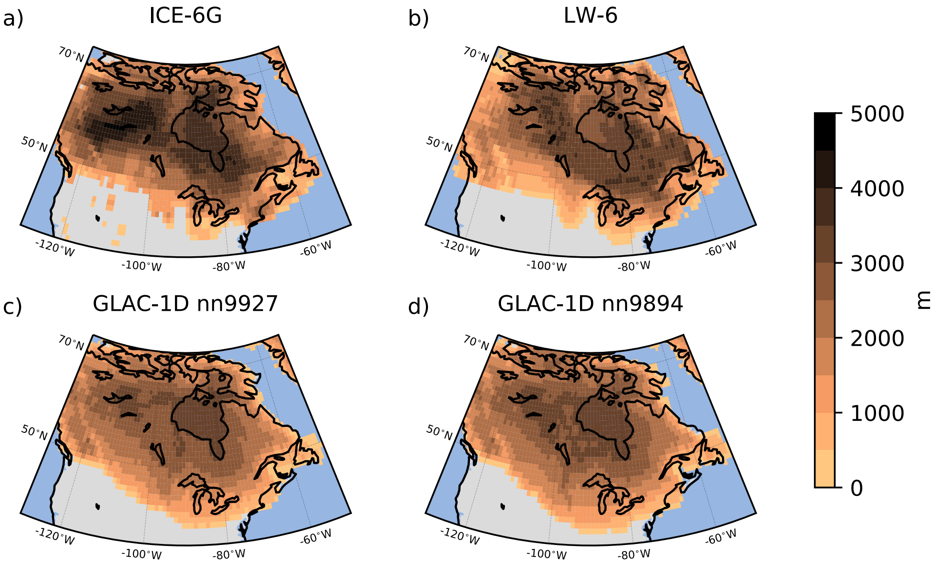

Figure 3.4: The ice thickness at LGM (26 ka) for the ice histories used in this study: a) ICE-6G (*Argus et al.*, 2014; *Peltier et al.*, 2015), b) LW-6 (*Lambeck et al.*, 2017), and c-d) two GLAC-1D models (*Tarasov et al.*, 2012)

thickness is different than that of the mantle convection model, but since our results turned out to be insensitive to the lithospheric thickness, this difference will not have a large effect.

An important uncertainty in the GIA model is caused by the unknown ice loading history. Four different ice histories are employed to assess this uncertainty. The ice models are: ICE-6G (*Argus et al.*, 2014; *Peltier et al.*, 2015), the model by *Lambeck et al.* (2017), which will be labelled LW-6, and two variants of the GLAC-1D model (*Tarasov et al.*, 2012), named GLAC-1D nn9894 and GLAC-1D nn9927. The ICE-6G and GLAC-1D models are global models, while LW-6 is a regional model. ICE-6G uses ice extent constraints and is tuned to fit relative sea level (RSL) data and geodetic constraints, although the fitting started with a model based on ice dynamics. The North American sector of GLAC1-D uses much of the same RSL and geodetic constraints as that of ICE-6G, as well as marine limit and strandline data. It also accounts for age uncertainty in the geologically-inferred deglacial margins and is derived from an approximate Bayesian formalism applied to a thermo-mechanically coupled glaciological model. The ICE-6G and GLAC-1D models are based on the VM5a viscosity profile (*Peltier et al.*, 2015), while the viscosity profile used for the LW-6 model consists of a three layer viscosity profile with an upper mantle viscosity of 5.1×10^{20} Pa s and a lower mantle viscosity of 1.3×10^{22} Pa s. There will be a bias in the viscosity fit towards the implicit viscosity profiles, although gravity data have not been used to constrain the ice models. To reduce the effect of the bias we use the different ice models and especially the GLAC-1D model, which depend less strongly on the viscosity, because they are primarily controlled by ice dynamics.

Ice thicknesses at 26 ka are up to 5000 meter in the ICE-6G model, and up to 4000 meter in the other models (Figure 3.4). ICE-6G also has thicker ice in the western part of North America compared to the other models. Together, this is a partial representation of the uncertainty in the ice loading history. For all models, three glacial cycles of 112 ka are used to account for the effect on the gravity anomaly of earlier glaciations in models containing larger values for the lower mantle viscosity. The glaciation phase, between 26 ka and 112 ka, of LW-6 is not available. We use the ICE-6G ice model to fill this gap. The first two glacial cycles are assumed to be the same as the last one.

3.2.6. SPHERICAL HARMONIC TRUNCATION LIMIT

The signal that we want to explain is the long-wavelength gravity field, which contains most of the GIA and mantle convection. The truncation limit should be a trade-off between containing most of the GIA and mantle signal, and minimizing the uncertainties in the other components, especially in the crustal model, which can introduce uncertainties up to 110 mGal (*Root et al.*, 2015). Also, the lithospheric density anomalies are especially uncertain in the short-wavelength region. Another argument in favor of a low maximum Spherical Harmonic (SH) degree is the assumption of local isostasy made in the model, which works best for long wavelength signals (*Gvirtzman et al.*, 2016; *Watts*, 2001), since flexural isostasy starts to contribute significantly to degrees larger than ~ 30 (*Watts and Moore*, 2017).

Mantle convection manifests itself in longer wavelengths, and contains most of its signal below SH degree 10 (e.g., *Gu et al.*, 2001; *Steinberger et al.*, 2019; *Su and Dziewonski*, 1991). Therefore, the truncation is mostly determined by the GIA signal. In Figure 3.5, the amplitude and the location of the GIA signal are plotted for models containing an upper mantle viscosity of either 2×10^{20} or 4×10^{20} Pa s and a lower mantle viscosity $>10^{21}$ Pa s. The solid lines result from models with an upper mantle viscosity of 4×10^{20} Pa s and a lower mantle viscosity of 3.2×10^{21} Pa s (blue), 1.3×10^{22} Pa s (green) and 2.6×10^{22} Pa s (red). The gravity anomaly for different viscosity profiles is represented by the shaded areas and exhibits the same behaviour as shown by the solid lines.

The idea is to find a truncation limit above which the GIA gravity signal loss is relatively small. The amplitude of the GIA signal over North America starts to decrease slightly for a maximum SH degree lower than 20, stabilises again and then decreases rapidly for a maximum SH degree lower than 10 (Figure 3.5a.). A second criterion is based on the location of the maximum amplitude of the GIA signal in the models. For different truncation limits, the location of the maximum amplitude in the gravity field is compared to that of the original model, which uses a maximum SH degree of 50 (Figure 3.5b). For a truncation limit at SH degree 10, the distance to the original maximum amplitude is almost 300 km. The previous sentences argue for a cut-off that is higher than 10, but does not have to be higher than 20 to capture most of the GIA model. Another criterion is that we want to reduce the effect of uncertainty in the crustal model. Since the large-scale features of the crustal models are very similar for a maximum SH degree of 15 or less, and the uncertainty in the crustal model is increased significantly for SH degree 20 (Figure 3.15), we will use SH degree 15 as the maximum degree for all models and observations in the rest of this study. We also briefly looked at cut-off degrees 14 and 16.

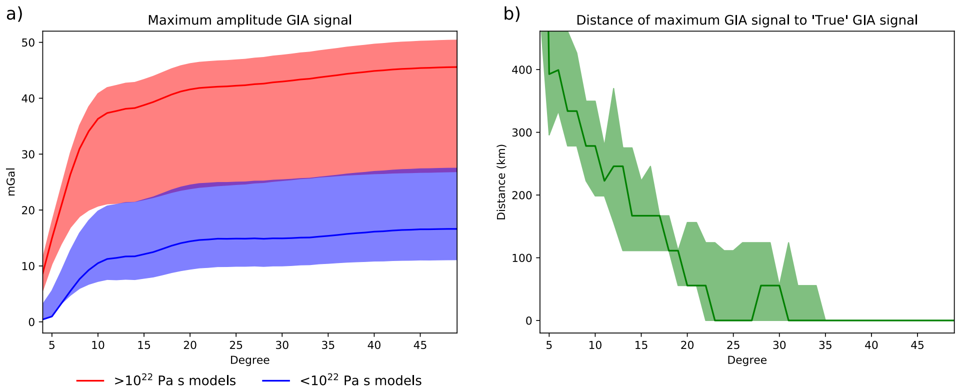

Figure 3.5: The gravity anomaly associated with the GIA signal, according to the GIA models employed in this study (a) and the distance of the maximum GIA signal to the maximum GIA signal using spherical harmonic degree up to 50 (b). The red and blue lines represent the first ($10^{21} < \nu_{lm} < 10^{22}$ Pa s) and second ($\nu_{lm} > 10^{22}$ Pa s) set of models, respectively. The shading encompasses all models within each set. For b, results from the sets of models are indistinguishable and therefore shown together. The solid lines represent the result for $\nu_{um} = 4 \times 10^{20}$ (all solid lines) and $\nu_{lm} = 3.2 \times 10^{21}$ Pa s (blue), 1.3×10^{22} Pa s (green) and 2.6×10^{22} Pa s (red). These viscosities are chosen for the solid lines, because these are the median values of the available models in the ranges considered.

3.3. RESULTS

To obtain density anomalies that are necessary to forward model gravity, we use the force balance of equation 3.4. We fit the viscosity to observations, and from our preferred viscosity we obtain the GIA and mantle convection contributions to the gravity field. As mentioned in Section 3.2.2, the lithospheric mantle densities are adjusted to ensure a force balance. We assign a single lithospheric density to each grid cell between the Moho and the LAB. We obtain lithospheric densities between 3320 and 3380 kg/m^3 (Fig 3.14a) using the LAB from *Hamza and Vieira* (2012). The range in lithospheric densities is larger (3140 - 3500 kg/m^3) for the WINTERC v5.2 LAB (Fig 3.14b). The largest differences between the modelled densities are present in areas where the lithosphere is relatively thin, since here the densities need to be adjusted more to accommodate a similar change in LAB. In areas where the lithosphere is thick, like Hudson Bay, differences in the modelled lithospheric densities are less prominent. Thus, because the LAB is used to determine the lithospheric density needed for isostasy, the sensitivity of the gravity anomaly to the LAB estimate is reduced.

Figure 3.6a shows the gravitational signal due to a combination of our crustal model (CRUST1.0) and our LAB (taken from *Hamza and Vieira*, 2012). A small gravity low of up to 15 mGal is present just Southwest of Hudson Bay. This gravity anomaly extends to the south and reaches 30 mGal south of Lake Michigan. The gravity high over the Rocky Mountains is up to 20 mGal. The uncertainty due to the crust can be caused by: i) the

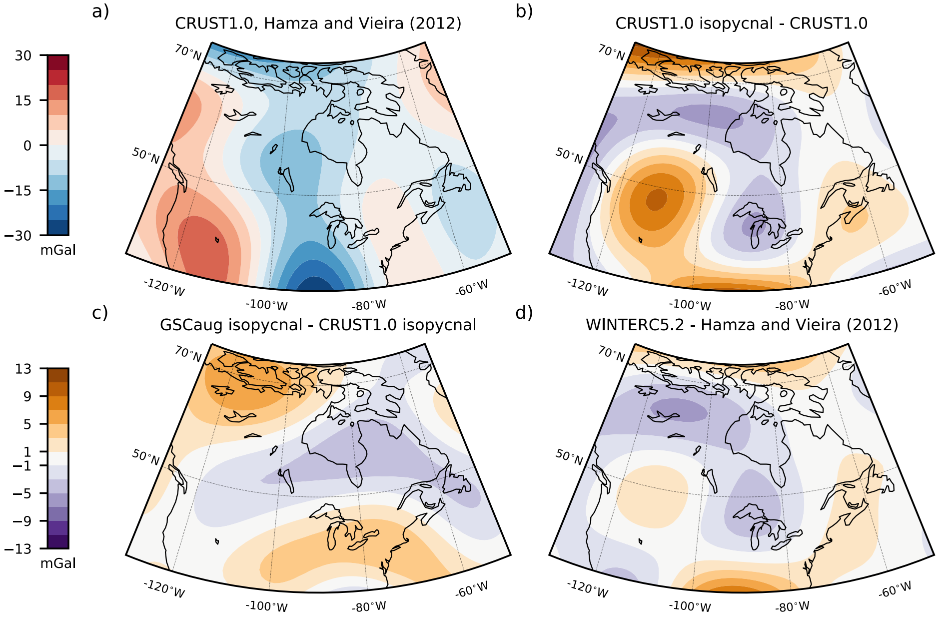

Figure 3.6: The effect of the crust and the lithosphere on the gravity field (a), and the spread in gravity field due to the use of different crustal densities (b), Moho models (c), or LAB models (d).

density profile adopted, and ii) the Moho employed in our model. To determine the effect of different density profiles, we compare the gravitational signal from a layered density profile with that of an isopycnal crust with a density of 2850 kg/m^3, without changing the Moho (in both cases, the Moho is that of CRUST1.0). The fact that we only focus on spherical harmonic degrees 2 to 15 greatly reduces the range, as only the long wavelength signals remain, and these are generally more consistent among different crustal models (Figure 3.6b-d). The range in the crustal signal over Hudson Bay is small and for the most part below 5 mGal. In two regions, the range is 10 mGal, namely in the Canadian Arctic Archipelago and in the geologically complex Rocky Mountains. Figure 3.6c shows the range in the crustal signal due to the Moho. This is the spread in gravity signal caused by employing the CRUST1.0 and the GSCaug Moho models. When determining the range caused by different Mohos, we have made use of an isopycnal crust. The range in the signal due to the Moho are small and, with the exception of the region over the Canadian Arctic Archipelago, below 5 mGal. We determine the range in signal due to different LABs in the same way as we did for the Moho. The range in the gravity contribution due to different LAB representations is only up to 5 mGal over Hudson Bay (Figure 3.6d). The reasons for these small numbers, despite large differences in LAB, are the compensating effect of fitting lithosphere densities to the isostasy constraint and the absence of a density jump at the LAB.

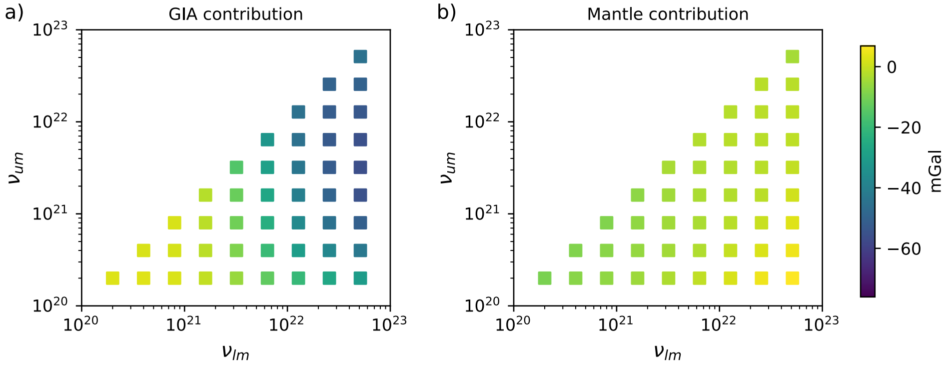

Figure 3.7: Contributions of GIA (a) and the mantle below 300 km (b) to the modelled minimum of the anomaly in the gravity field for different upper and lower mantle viscosities, in mGal, calculated at the location of the modelled maximum.

GIA and surface dynamic topography both contribute to the total modelled gravity signal of the crust-lithosphere-asthenosphere model through their contribution to the force balance (Equation 3.2) and the resulting effect on the lithospheric density. To compare the contributions of GIA and the mantle, the GIA and surface dynamic topography heights calculated in Section 3.2 are converted to SH coefficients. The contributions from mantle density anomalies and CMB topography are added to that of surface dynamic topography to form the total effect of the mantle. From the SH coefficients for GIA and the mantle, the gravity anomalies can be calculated and compared. We vary the viscosity values of the upper and lower mantle between 10^{20} and 10^{23} Pa s and calculate the gravity signal at the location of the modelled minimum in the gravity anomaly. We do so, because we believe that the gravity anomaly minimum characterises the signal better than a value of the gravity anomaly at a fixed location. The viscosity influences the gravity signal through the GIA and surface dynamic topography contribution to the force balance, and also through the CMB topography. Thus, even though the GIA deflections can not be isolated from the crustal geometry, we can obtain the GIA contribution to the gravity field with a strong constraint on lower mantle viscosity, with which we can predict the GIA signal. Figure 3.7 exhibits a wide range of values, depending on the viscosity profile. The GIA contribution is most sensitive to the viscosity of the lower mantle. For lower mantle viscosities $>10^{22}$ Pa s, GIA contributes at least 30 mGal to the negative anomaly. This contribution decreases when the lower mantle viscosity decreases. Lower viscosities imply a shorter relaxation time, and consequently less remaining uplift is present in the lithosphere. This results in a smaller contribution to the gravity field. For all viscosity profiles, the contribution of the mantle below 300 km (including surface dynamic topography) does not exceed -20 mGal, and can even be weakly positive for lower mantle viscosities $>10^{22}$ Pa s. The crust and lithosphere contributions do not depend on the underlying viscosity profile, and contribute 15 ± 10 mGal to the gravity anomaly (Figure 3.6a). The spread in the crustal signal comes from the changing location of the minimum, and the use of different crustal models.

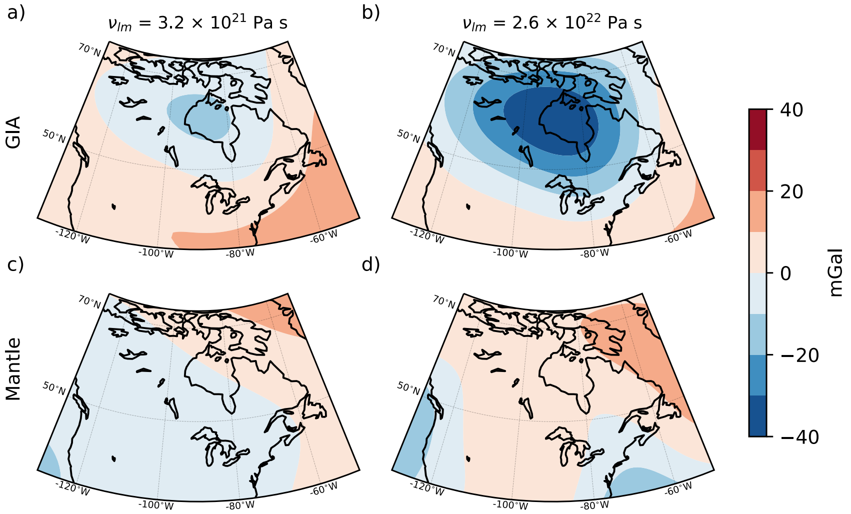

Figure 3.8: Effect of GIA (top row) and mantle convection (bottom row) on the gravity field for a lower mantle viscosity equal to 3.2 × 10 ^{21} Pa s (first column) and 2.6 × 10 ^{22} Pa s (second column). The viscosity of the upper mantle is the same across all subplots and equal to 4 × 10^{20} Pa s.

As we have seen that the gravity field is sensitive to the lower mantle viscosities, it is insightful to exhibit the contributions of GIA and the mantle below 300 km (with surface dynamic topography), and their dependence on the lower mantle viscosity. Depending on the lower mantle viscosity, the GIA signal can be up to 20 mGal (Figure 3.8a) or up to 40 mGal (Figure 3.8b). For mantle convection, amplitudes are lower, but the sign can be reversed depending on the lower mantle viscosity. For a lower mantle viscosity of 3.2 × 10^{21} Pa s, the signal is weakly negative and consequently contributes positively to the observed gravity anomaly (Figure 3.8c). For a viscosity of 2.6 × 10^{22} Pa s, anomalies due to mantle convection are weakly positive over Hudson Bay (Figure 3.8d). The positive signal in Figure 3.8d compensates slightly for the increased amplitude of the negative anomaly due to GIA.

Next, we look for constraints on the lower mantle viscosity, taking into account uncertainties in other components. In order to place constraints on the viscosity of the lower mantle, we have created models according to Equation 3.1 for different combinations of the upper and lower mantle viscosity, using the crustal and lithospheric models of Figure 3.3. We compared results of these models with the observed gravity field for the area depicted by the red dashed line in Figure 3.1, which is the area covering Hudson Bay and the region south of Hudson Bay up to major lakes like Lake Michigan. A misfit is then calculated using the following formula:

$$\chi^2 = \frac{1}{N}\sum_{\mathrm{i}=1}^{\mathrm{N}}\left(\frac{o_{\mathrm{i}} - p_{\mathrm{i}}}{\sigma_{\mathrm{i}}}\right)^2, \tag{3.6}$$

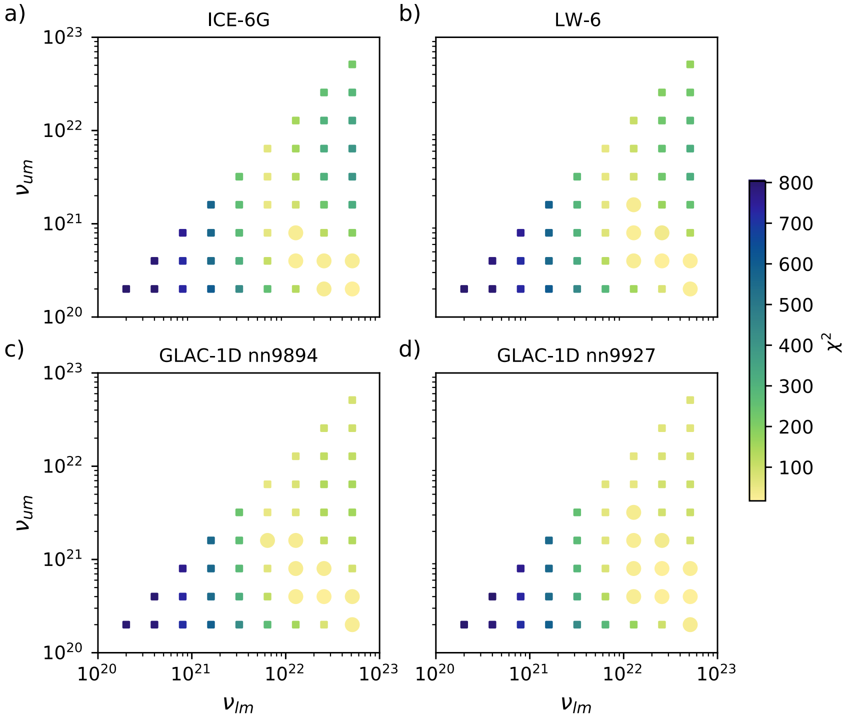

Figure 3.9: χ^2 misfit for different upper (ν_{um}) and lower (ν_{lm}) mantle viscosities. Each subplot is made using a different ice history: a) ICE-6G *Argus et al.* (2014); *Peltier et al.* (2015), b) LW-6 *Lambeck et al.* (2017), and c-d) two GLAC-1D ice histories *Tarasov et al.* (2012). Models containing lower mantle viscosities > 10^{22} Pa s perform better for all ice histories. The models that fit the data within 2.5 × the standard deviation are denoted by circles.

where N is the number of grid cells inside the area of the latitude/longitude grid, and o_i and p_i are the observations and the predicted values at gridpoint i, respectively. σ_i is the uncertainty of the observation. Since the values of the observed gravity anomaly at each gridpoint are correlated, we can not use this as the uncertainty. Instead, we attribute an arbitrary value of 1 to σ_i, and calculated χ^2 values for four possible combinations of crustal models and LABs. We then averaged the results of these models. The relative value with respect to other viscosity profiles is what matters in these plots. We have highlighted the models for which χ^2 is below 40. This is an arbitrary boundary created to emphasize the better performing models. The misfit for different upper and lower mantle viscosities is shown in Figure 3.9. The well performing models are found almost exclusively for lower mantle viscosities of more than 10^{22} Pa s (Figure 3.9). Models containing lower mantle viscosities in the range 10^{21} - 10^{22} Pa s underestimate the negative anomaly in the gravity field observed over Hudson Bay, naturally resulting in high χ^2 values.

Next, we investigate whether this conclusion changes for different choices in the mod-

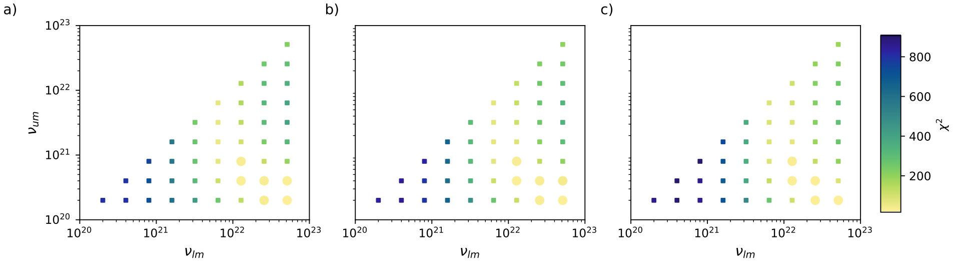

Figure 3.10: χ^2 misfit for different upper (ν_{um}) and lower (ν_{lm}) mantle viscosities using ICE-6G (*Argus et al.*, 2014; *Peltier et al.*, 2015). Results are shown for a lithospheric thickness of 80 km (a), 115 km (b), and 150 km (c). Models containing lower mantle viscosities > 10^{22} Pa s perform better for all ice histories. The models that have a χ^2 lower than 40 are denoted by circles.

elling. The good fit for lower mantle viscosities above 10^{22} Pa s does not change if we change the lithospheric thickness in the GIA model from 80 km to 115 km or to 150 km (Figure 3.10), or if we make the area of interest smaller (the area delimited by the dashed red line in Figure 3.1). For example, we can choose the area to contain all points that have a value that is at least 40 percent of the peak value, as opposed to the 50 percent threshold used in the rest of this study. Moreover, if simulations were performed with a different spherical harmonic truncation limit (e.g., 14 or 16 as the upper limit), the general patterns in the misfit plot remain the same. The most important other sources of uncertainty are discussed in the following paragraphs.

The next parameter that we will discuss is the ice history, which is used as an input to the GIA model. Variations in ice heights and the time of melting translate directly in the gravity signal (*Mitrovica and Peltier*, 1991b). The subplots in Figure 3.9 correspond to the four ice histories used. Lower mantle viscosities >10^{22} Pa s show lower misfit values, regardless of the ice model used. This confirms that the preferred viscosity profile does not depend strongly on the ice history. For the GLAC-1D nn9894 ice history, lower mantle viscosities of 6.4 × 10^{21} Pa s also perform well. However, for these specific well performing models, the upper mantle viscosity needs to be >10^{21} Pa s, which is not corroborated by other studies on the viscosity of the upper mantle in North America (e.g., *Paulson et al.*, 2007; *Sasgen et al.*, 2012; *Tamisiea et al.*, 2007; *Wolf et al.*, 2006). Thus, regardless of the employed ice history, lower mantle viscosities >10^{22} Pa s are preferred.

The final parameter that we will test the sensitivity to is the conversion factor from seismic velocity anomalies to density anomalies. We vary the conversion factor between 0.1 and 0.4 to represent the range of possible values (*Trampert et al.*, 2004) and study its effect on our conclusions. For each conversion factor a χ^2 misfit is calculated using Equation 3.6. The largest sensitivity is to the viscosity of the lower mantle. For this reason, Figure 3.11 shows the spread in χ^2 values as a function of the lower mantle viscosity, while the upper mantle viscosity is kept fixed at 4 × 10^{20} Pa s. Almost all models containing lower mantle viscosities >10^{22} Pa s have a lower χ^2 value than models containing lower mantle viscosities <10^{22} Pa s, independent of the conversion factor used. The spread in misfit values between observations and models decreases when the lower

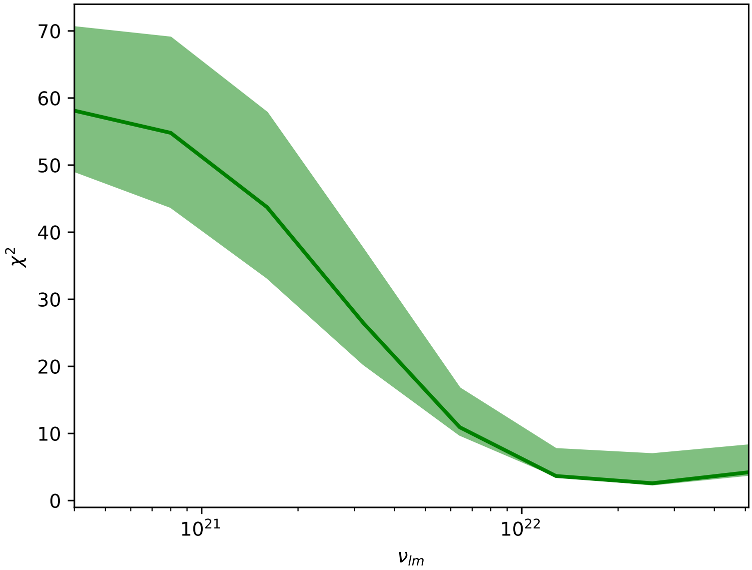

Figure 3.11: χ^2 misfit as a function of the lower mantle viscosity for different conversion factors in the mantle convection code. The dark green line shows the χ^2 misfit for a conversion factor of 0.15, the default value used in the study. The spread indicates the effect of varying the conversion factor between 0.1 and 0.4.

mantle viscosity is increased. This is because, for those viscosities, the contribution of the mantle convection signal is close to zero, or just about positive over North America (see Figure 3.7). Consequently, an amplification or reduction does not alter this contribution much. Hence, the preferred viscosity profile is not sensitive to the conversion factor, in agreement with findings by *King* (1995), justifying our choice for a single value of the conversion factor of 0.15.

Figure 3.12 shows the gravity field from the best fitting model and the residual between this model and the gravity observations. We find the lowest misfit for the LW-6 ice history, using an upper mantle viscosity of 4 × 10^{20} Pa s and a lower mantle viscosity of 2.56 × 10^{22} Pa s. Some residuals can be expected over other areas over North America, as the misfit is only calculated over Hudson Bay. Nevertheless, the negative residual to the southwest of Hudson Bay near the Rocky Mountains deserves special attention, because it influences the gravity anomaly inside the region bounded by the contour in Figure 3.1. There are several possible explanations for this anomaly: Figure 3.6b suggests that the uncertainty in the density profile is the cause, as a clear uncertainty over the Rocky Mountains due to the density profile is exhibited. Employing an isopycnal crust indeed improves the fit, but does not enable the full removal of the anomaly over the Rocky mountains. Other options are changes in the LAB (see Figure 3.6d) or the effect of lateral viscosity changes in GIA models(e.g., *A et al.*, 2013; *Kuchar et al.*, 2019; *Paulson et al.*, 2005).

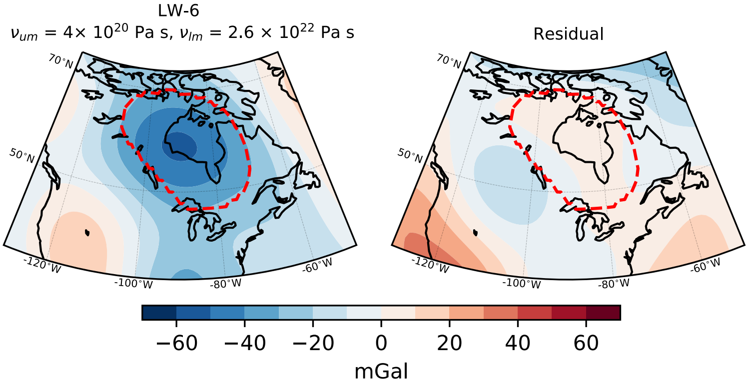

Figure 3.12: Long-wavelength gravity anomaly of the model containing the best fitting viscosity profile (ν_{um} = 4 × 10^{20} Pa s, ν_{lm} = 2.6 × 10^{22} Pa s) and ice history (LW-6) (a), and the residual with the observations (b). The red dashed line denotes the area used for the calculation of the misfit with the observed gravity field of XGM2016.

3.4. CONCLUSION & DISCUSSION

In this study, we combined dynamic models for GIA and mantle convection with a crust-lithosphere-asthenosphere model, and matched the results to the long-wavelength gravity anomaly. The dynamic pressures caused by GIA and surface dynamic topography are implemented in the crust-lithosphere-asthenosphere model to compute the lithospheric density anomalies that are needed for isostasy. We argue that this is a necessary step to be able to derive a consistent forward gravity field model. Uncertainties in the ice history, crustal model, LAB and conversion factor are found to be small enough in the long-wavelength domain, such that a lower bound can be placed on the lower mantle viscosity. The best fitting model to the gravity field observations is found when lower mantle viscosities are larger than 10^{22} Pa s. Our results do not constrain the upper mantle viscosity, as the better performing models are present for the full range of upper mantle viscosities (10^{20} - 10^{21} Pa s) preferred in previous studies (e.g., *Paulson et al.*, 2007; *Sasgen et al.*, 2012; *Tamisiea et al.*, 2007; *Wolf et al.*, 2006).

Previous studies have suggested that the gravity anomaly over Hudson Bay is mainly due to mantle convection (*Cathles*, 1975; *James*, 1992; *Peltier et al.*, 1992). *Peltier et al.* (1992) found that conversion factors (from seismic velocities to densities) in the range of 0.5-1.5 are needed to explain the gravity anomaly by mantle convection, which is large compared to recent estimates which are in the range 0.1-0.4 (*Trampert et al.*, 2004). *Tamisiea et al.* (2007) attributed less than 50 percent (25-45%) of the anomaly to GIA. They estimated the viscosity based on gravity rates, but did not check whether the remaining percentage can be explained by mantle convection and did not include crustal and lithospheric density anomalies. Our results show that, at the modelled minimum, at least 60 percent of the negative anomaly in the gravity field can be attributed to GIA. In previous studies (*Métivier et al.*, 2016; *Simons and Hager*, 1997), the authors also found a preference for a lower mantle viscosity $> 10^{22}$ Pa s.

Earlier GIA studies (*Caron et al.*, 2017; *Nakada and Okuno*, 2016) found that two sets of viscosity profiles result in small misfit values, which is classical for GIA models. The first set of well-performing models contains lower mantle viscosities between 10^{21} and 10^{22} Pa s, whereas the second set has lower mantle viscosities greater than 10^{22} Pa s. Solutions containing lower mantle viscosities between 10^{21} and 10^{22} are derived from data on RSL (*Cianetti et al.*, 2002), GRACE gravity rates (*Tamisiea et al.*, 2007; *van der Wal et al.*, 2008), GPS (*van der Wal et al.*, 2009) or a combination of two of these (*Paulson et al.*, 2007; *Zhao*, 2013). ICE-6G is based on the VM5a viscosity structure, which has a lower mantle viscosity $<10^{22}$ Pa s (*Peltier and Drummond*, 2008).

In contrast, several studies have found a high viscosity in the lower mantle, for example by an inversion of GPS, tide level gauges, absolute gravimetry and sea level indicators (*Wolf et al.*, 2006) or by inverting for gravity rate observations from GRACE together with present-day ice mass changes in Alaska and Greenland (*Sasgen et al.*, 2012). *Steffen et al.* (2009) compared GRACE solutions with results of a GIA model adjusted to fit RSL curves and found 2×10^{22} Pa s for the lower mantle viscosity. Geological evidence for RSL change and the tilting of paleo lake shorelines, combined with present-day crustal movement converged to high lower mantle viscosity models (*Lambeck et al.*, 2017). *Métivier et al.* (2016) used gravity gradients and concluded that lower mantle viscosities larger than 2×10^{22} Pa s are preferred. This agrees with analysis of $\dot{J}_2$ data, which required viscosities above 5×10^{22} Pa s in the lower part of the lower mantle (*Nakada and Okuno*, 2016). Finally, *Kuchar et al.* (2019) found that an average viscosity of 3×10^{22} Pa s is needed to fit RSL data in 1D models and that the evolution of the peripheral bulge near the Atlantic and Gulf coast is what requires these high viscosities. While the area investigated here does not include the peripheral bulge near the Atlantic and Gulf coast, results from our model, constrained by the gravity field, exhibit a clear preference for lower mantle viscosities $> 10^{22}$ Pa s. The lower mantle viscosity affects inferences based on GIA models, such as the distribution of ice volume required to close the sea level budget at LGM (*Lambeck et al.*, 2014).

In general, mantle convection studies are global studies, employing a more complex radial viscosity profile than used in our study. Nevertheless, the viscosity found in our study is in rough agreement with studies on slab sinking speeds (*Čížková et al.*, 2012), mantle convection (e.g., *Bower et al.*, 2013; *Perry et al.*, 2003; *Steinberger*, 2007), or when mantle convection is combined with GIA (*Mitrovica and Forte*, 2004). In three-layered mantle convection models, one of the important parameters determining the amplitude and shape of the surface dynamic topography is the increase in viscosity between the upper and lower mantle. Since the upper mantle viscosity over North America is found to lie between 10^{20} and 10^{21} Pa s (e.g., *Paulson et al.*, 2007; *Sasgen et al.*, 2012; *Tamisiea et al.*, 2007; *Wolf et al.*, 2006), lower mantle viscosities $> 10^{22}$ Pa s require a jump that is likely to be at least a factor of 20 at the boundary between the upper and lower mantle. This is consistent with other mantle convection studies (*Rudolph et al.*, 2015), but deviates somewhat from a study that found a jump of only 10 between the upper and lower mantle viscosity (*Liu and Zhong*, 2016). All in all, our results are not in conflict with most studies on mantle convection. Our results also prefer an upper mantle viscosity between

10^{20} and 10^{21} Pa s, and consequently support a contrast larger than 20 between the upper and lower mantle viscosity, which favours slower slab sinking speeds (*Van der Meer et al.*, 2018).

We have developed an approach to combine crust-lithosphere-asthenosphere models with models for GIA and surface dynamic topography using isostasy. In principle, we solve for the average viscosity value of the complete lower mantle, but most of the sensitivity will be towards the upper part of the lower mantle (e.g., *Mitrovica and Peltier*, 1991c). Our approach can in principle be applied to other regions that experience ongoing large scale GIA, like Fennoscandia, Alaska, and Antarctica. The spherical harmonics were truncated at degree 15, which diminished uncertainties due to the crustal model that were previously found to be large in Scandinavia (*Root et al.*, 2015). If we studied small scale GIA signals, a larger uncertainty would be introduced by the crustal model. Since mantle convection covers the long wavelengths, this concept could also be useful for regional mantle convection models that aim to constrain viscosity or the conversion factor from seismic velocities to densities.

3.5. APPENDIX A: SENSITIVITY TO LITHOSPHERIC THICKNESS IN THE MANTLE CONVECTION MODEL

In Figure 3.10, we have shown that the main results do not exhibit a large sensitivity to the lithospheric thickness in the GIA model. Besides the sensitivity to the lithospheric thickness in the GIA model, it is also insightful to explore the sensitivity to the thickness of the lithosphere in the mantle convection model. There are also only minor differences in the gravity signal coming from the mantle convection model, up to 0.6 mGal for an upper and lower mantle viscosity of 4×10^{20} and 1.3×10^{22} Pa s, respectively (Figure 3.13).

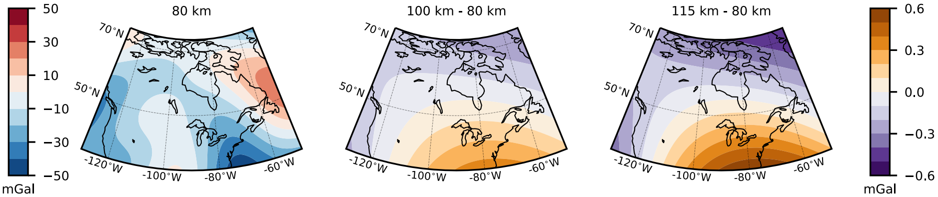

Figure 3.13: Gravity field resulting from the mantle convection model for a lithospheric thickness of a) 80 km, and differences xfor a lithospheric thickness of b) 100 km, and c) 115 km. In these figures, an upper and lower mantle viscosity of 4×10^{20} and 1.3×10^{22} Pa s are employed, respectively.

3.6. APPENDIX B: ISOSTATIC LITHOSPHERIC MANTLE DENSITIES

Lithospheric mantle densities are adjusted to fulfil the requirement of isostasy. The adjusted lithospheric mantle densities are shown in Figure 3.14. The range in values for the lithospheric mantle density is larger when the WINTERC 5.2 LAB is used, compared to that using the LAB from *Hamza and Vieira* (2012). This implies that larger lateral changes in lithospheric mantle density are needed to satisfy the isostasy requirement when WINTERC 5.2 is used for the LAB.

3.7. APPENDIX C: THE CRUSTAL SIGNAL FOR LMAX 20

In our study, we have only looked at the first 15 SHs. For a maximum degree of 20, the range in the gravity signal is of the same magnitude, but there are more regions where the spread is > 10 mGal, as compared to Figure 3.6.

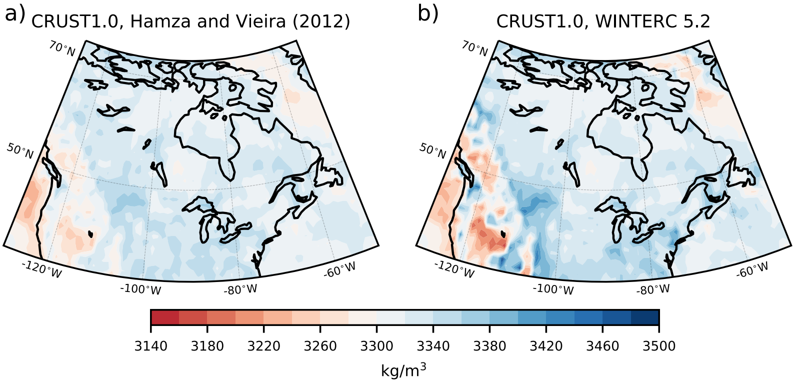

Figure 3.14: Lithospheric mantle densities after isostatic compensation using the CRUST1.0 crustal model and (a) the LAB from *Hamza and Vieira* (2012), or (b) the WINTERC 5.2 LAB.

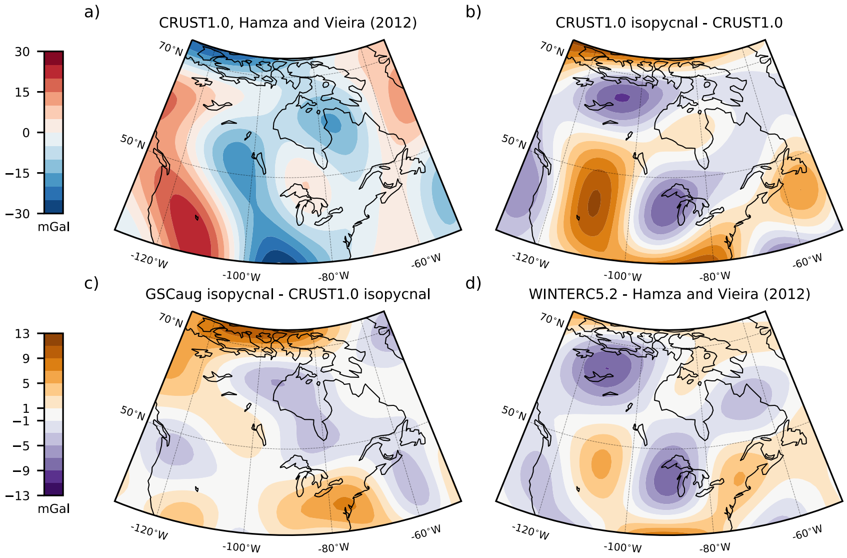

Figure 3.15: Same as Figure 3.6, but now for a maximum degree of 20. The spread in the gravity field is of the same magnitude, but there are more region with uncertainties > 10 mGal, especially in the crust.

4

SIMULATING HORIZONTAL CRUSTAL MOTIONS OF GLACIAL ISOSTATIC ADJUSTMENT USING COMPRESSIBLE CARTESIAN MODELS

Abstract

Significant land uplift and horizontal motions have been recorded with Global Navigation Satellite Systems (GNSS) in areas such as Alaska, Iceland, and the Northern Antarctic Peninsula (NAP) as a result of Glacial Isostatic Adjustment (GIA) due to ice melt after the Little Ice Age. Here, analysis of horizontal displacement rates can be of extra importance, as they are more sensitive to Earth properties in shallower layers than vertical displacement rates. Proper modelling of horizontal displacement rates with dedicated GIA models requires a spherical Earth with compressible rheology. However, in these small areas, the employed GIA models are often incompressible using a cartesian geometry to ease computation and in some cases allow for lateral viscosity changes or more complex rheology. We investigate the validity of modelled horizontal displacement rates using different approximations, i.e. using spherical or cartesian Earth structures, and incompressible, material compressible or compressible rheology. While the lack of self-gravity and sphericity compensate each other in the vertical, this is less the case for the horizontal. For a disc ice sheet with a radius just over 200 km and a thickness of 1,000 m, differences due to sphericity are

---

This chapter is published as Reusen, J. M., Steffen, R., Steffen, H., Root, B. C., & van der Wal, W. (2023). Simulating horizontal crustal motions of glacial isostatic adjustment using compressible Cartesian models. Geophysical Journal International, 235(1), 542-553.

minimal, and the modelled horizontal displacement rates of compressible cartesian models differ from those simulated by a compressible spherical model by 0.63 mm/a. Thus, compressible cartesian GIA models can be applied for modelling horizontal displacement rates of small ice sheets like those in Alaska, Iceland, and NAP. Unfortunately, the implementation of compressibility in Abaqus that we use here cannot be extended to spherical models as gravity can not be specified for a spherical body. Other modelling approaches are recommended in such cases.

4.1. INTRODUCTION

In understanding Glacial Isostatic Adjustment (GIA) the observed horizontal motions of the crust generally receive less attention than the vertical motions, even though these horizontal motions are found to be very sensitive to lateral and radial variations in viscosity (e.g., *Gasperini et al.*, 1990; *Hermans et al.*, 2018; *Kaufmann et al.*, 2005; *Latychev et al.*, 2005; *O'Keefe and Wu*, 2002; *Steffen et al.*, 2006; *Vardić et al.*, 2022). In addition, horizontal motions are significantly affected by compressibility (*James and Lambert*, 1993; *Johnston et al.*, 1997; *Mitrovica et al.*, 1994a; *Tanaka et al.*, 2011), which is not supported by several commonly used GIA models.

In particular, GIA models which neglect sphericity generally do not include compressibility. To our knowledge, the only exceptions are *Wolf et al.* (1985), which is based on a uniform Earth model, and *Klemann et al.* (2003) which is no longer in use (Klemann, personal communication). Such 'cartesian models', as we will call them in the following, have been used for several applications. However, cartesian models either assume incompressibility (e.g., *Árnadóttir et al.*, 2009; *Ivins and James*, 1999; *Larsen et al.*, 2003, 2004; *Pagli et al.*, 2007; *Schotman et al.*, 2008; *Zwinger et al.*, 2020), or use material compressibility only (e.g., *Auriac et al.*, 2013; *Kaufmann et al.*, 2005; *Lund et al.*, 2009; *Marsman et al.*, 2021; *Nield et al.*, 2018; *Steffen et al.*, 2006). The latter refers to models in which the material is compressible, i.e. it has a Poisson ratio below 0.5, but the buoyancy forces are not adjusted for the change in density due to compressibility (*Klemann et al.*, 2003). However, it is currently unclear how accurate the approximation of material compressibility is compared to full compressibility, where the internal buoyancy force is included in the equation of motion. Compressibility can also be approximated by adjusting the flexural rigidity, which is most accurate for smaller wavelength signals (*Tanaka et al.*, 2011). Cartesian models are attractive because they provide a means to incorporate high spatial resolution and 3D variations in Earth structure with small computation times. In the following we will refer to models that can deal with 3D variations in Earth model parameters as 3D models.

Cartesian GIA models provide sufficient accuracy for the vertical deformation for ice sheets up to the size of the Fennoscandian ice sheet (*Amelung and Wolf*, 1994; *Wu and Johnston*, 1998), but for horizontal deformation this has been less thoroughly investigated. In this study, we will explore to what extent cartesian models can be used for GIA studies, for incompressible, material compressible, and fully compressible models. We thereby test a recently highlighted implementation of compressibility, and investigate possibilities to extend this to a spherical geometry.

We aim to answer the following research questions:

(1). How can we implement full compressibility in cartesian GIA models of Abaqus?

(2). How well are horizontal motions approximated by a cartesian model with (i) incompressibility, (ii) material compressibility and (iii) full compressibility as compared to a fully compressible spherical model?

We focus on the horizontal motions, as the effect of compressibility on the horizontal is larger, and the observations are to date relatively underused. To answer the first research question, we implement compressibility using the method of *Hampel et al.* (2019) for cartesian multi-layer models in Abaqus. We also briefly examine the method of *Hampel et al.* (2019) for spherical GIA models, but conclude that the method cannot be implemented in spherical models. We compare the cartesian model with a spherical compressible 1D model based on a semi-analytical method, and we include a case study of glacial unloading on top of a low-viscous mantle representative of the mantle in West Antarctica, Alaska, and Iceland. This provides recommendations for what applications the cartesian model, compressible or incompressible, can be used regarding analysis of horizontal motions and their observation.

4.2. THEORY

The software Abaqus is based on the finite element (FE) method. Two different implementations are described, which have been used in the modelling of the loading scenarios: (1) a model employing Elastic Foundations (EF, *Wu*, 2004), similar to the model in *Schotman et al.* (2008), and (2) a "Non-linear geometry with explicit Gravity" (NG) model, described in *Hampel et al.* (2019). The EF model is employed in many GIA studies (e.g., *Li et al.*, 2020; *Lund et al.*, 2009; *Nield et al.*, 2022; *Steffen et al.*, 2006; *van der Wal et al.*, 2015), and has been benchmarked for incompressible material parameters in *Spada et al.* (2011). It is used to validate the NG model implementation for the incompressible case. We start with a description of the governing equations of GIA, and how this is handled by the EF model. Afterwards, we introduce how the finite element equations are solved in Abaqus to better understand what is done in the NG model, and its differences with the EF model.

The conservation of momentum equation for external loading of a compressible Earth linearized with respect to hydrostatic equilibrium is given by (*Wu and Peltier*, 1982):

$$\nabla\cdot\boldsymbol{\tau}-\nabla\left(\mathbf{u}\cdot\rho_0 g_0\hat{r}\right)-\rho' g_0\hat{r}-\rho_0\nabla\phi'=0. \tag{4.1}$$

Here, $\boldsymbol{\tau}$ is the Cauchy stress matrix, $\mathbf{u}$ is the displacement vector, ρ_0 and g_0 are the hydrostatic background density and gravity, respectively, $\hat{r}$ is the unit vector in the radial direction, ρ' denotes the density perturbation with respect to the hydrostatic background state, and ϕ' is the perturbation in the gravitational potential. Equation 4.1 contains four terms. The first term is the divergence of stress. The second term is the restoring force of isostasy (*Wu*, 2004), which is an upwards force preventing the ice load from sinking indefinitely. The third term is the internal buoyancy force, caused by the change in the density of the individual elements due to dilatation. The density perturbation that is added to equation 4.1 is derived from the mass conservation equation (*Backus*, 1967):

$$\rho'=-\nabla\cdot\left(\rho_0\mathbf{u}\right). \tag{4.2}$$

For incompressible models, changes in density are zero (i.e. $\rho'=0$) and the third term in equation 4.1 disappears. The fourth term in equation 4.1 represents the self-gravity.

We will neglect the self-gravity in the cartesian models as this is not typically included in earlier studies with such models, partly because it is found to compensate the lack of sphericity (*Amelung and Wolf*, 1994). However, it is present in the spherical NMM model that we use for validation, so we need to quantify that effect. In compressible models, the gravitational potential responds to a change in the density of the elements. The perturbed potential can be derived from Poisson's equation (*Wu and Peltier*, 1982):

$$\nabla^2 \phi' = 4\pi G \rho'. \tag{4.3}$$

Here G is the gravitational constant. The corresponding boundary conditions for the GIA problem are summarised below.

4.2.1. BOUNDARY CONDITIONS

The general boundary conditions are (*Cathles*, 1975; *Wu*, 2004):

(i) at the surface of the Earth, $[\tau_{rr}]_{r=0}$ = -σg_0, where σ is the surface mass density of the ice load, and r is the depth, where $r = 0$ corresponds to the surface and is defined positive downwards. In other words, the normal stress at the surface is equal to the applied pressure due to the load. For shear stresses, we have $[\tau_{r\theta}]_{r=0} = 0$.

(ii) At internal boundaries, there should not be a discontinuity in the stress and the displacements. For the stress this implies $[\tau_{rr}]_{r-}^{r+} = [\tau_{r\theta}]_{r-}^{r+} = 0$, and for the displacement this translates to $[\mathbf{u}]_{r-}^{r+} = 0$.

(iii) At the Core-Mantle Boundary (CMB), the fluid core is simulated by setting the normal stress equal to the multiplication of the core density, ρ_f, with gravity, g_0, and with the radial displacement at the CMB, u_r: $[\tau_{rr}]_{r=-H} = \rho_f g_0 u_r$. Here H is the depth to the CMB. In Abaqus, the core is simulated by employing a Winkler foundation at the model bottom with a magnitude equal to $\rho_f g_0$. The tangential stresses vanish at the CMB, and there is continuity of displacement, i.e. $[\mathbf{u}]_{r-}^{r+} = 0$.

4.2.2. THE EF METHOD

Here, we briefly review the method that uses elastic foundations and a stress transformation (*Wu*, 2004). The setup of the model is illustrated in Figure 4.1a. Abaqus differentiates between small-displacement and large-displacement analyses (Table 4.1) via the nonlinear geometry keyword (NLGEOM; Abaqus 2021 documentation, *Hibbitt et al.*, 2016). The elements in a small-displacement analysis used by *Wu* (2004) do not carry the information of the stress with them. Therefore, buoyancy forces associated with density changes are not included in the stiffness matrix. Moreover, the stiffness matrix is linear, as there is no dependence on the prior displacement. Using this method, we need to manually add an isostatic restoring force to prevent the load from sinking indefinitely (*Purcell*, 1998; *Wu*, 1992). To still satisfy the equation of motion (equation 4.1), the following stress transformation is performed (*Wu*, 2004):

$$\boldsymbol{t} = \boldsymbol{\tau} - \rho_0 g_0 u_r \boldsymbol{I}. \tag{4.4}$$

Here $\boldsymbol{\tau}$ is the stress, $\boldsymbol{t}$ the transformed stress, and u_r the displacement in the radial direction. The divergence of the transformed stress now becomes equal to the divergence of the stress plus the isostatic restoring force term:

$$\nabla \cdot \boldsymbol{t} = \nabla \cdot \boldsymbol{\tau} - \rho_0 g_0 \nabla u_r. \tag{4.5}$$

The equation of motion for non-self gravitating incompressible models reads

$$\nabla \cdot \boldsymbol{\tau} - \nabla \left(\mathbf{u} \cdot \rho_0 g_0 \hat{r}\right) = 0. \tag{4.6}$$

Equation 4.6 is the same as Equation 4.1, but without internal buoyancy (third term in Equation 4.1) and self-gravity (fourth term in Equation 4.1). With the stress transformation of Equation 4.5, we can write the equation of motion for non self-gravitating incompressible models as

$$\nabla \cdot \boldsymbol{t} = 0, \tag{4.7}$$

which can then be solved by Abaqus. The boundary conditions are changed because of the stress transformation, and are listed in the next subsection.

BOUNDARY CONDITIONS FOR THE EF METHOD

The boundary conditions for the transformed stress are as follows (*Wu*, 2004):

(i) at the surface of the Earth, $[t_{rr} + \rho_0 g_0 u_r]_{r=0}$ = -σg_0. This is the same as before, but now with an extra term due to the substitution of $\boldsymbol{t}$ for $\boldsymbol{\tau}$. The boundary conditions for the shear stresses are not affected by the stress transformation: $[\tau_{r\theta}]_{r=0} = 0$.

(ii) at internal boundaries, we again need continuity in the stress and displacement. For the normal stress we obtain $[t_{rr}]_{r-}^{r+} = \left(\rho_- - \rho_+\right) g_0 u_r$. For the shear stress and the displacement, we have $[\tau_{r\theta}]_{r-}^{r+} = 0$, and $[\mathbf{u}]_{r-}^{r+} = 0$.

(iii) at the CMB, the boundary condition is also altered, as now the difference in density between the solid lower mantle, ρ_s and the fluid core, ρ_f, is the required quantity (*Wu*, 2004): $[t_{rr}]_{r=-H} = \left(\rho_f - \rho_s\right) g_0 u_r$. Again, the tangential stresses vanish at the CMB, and $[\mathbf{u}]_{r-}^{r+} = 0$.

These boundary conditions are satisfied by applying elastic foundations at the boundaries with a magnitude equal to the density difference ($\Delta\rho$) across the layer multiplied with the background gravity g_0. The elastic foundations act as a stabilizing force, as they work in the direction opposite to the radial displacement, and their magnitude increases with the radial displacement. The elastic foundations only work for horizontal boundaries, while inclined boundaries can be simulated using springs (*Schmidt et al.*, 2012a).

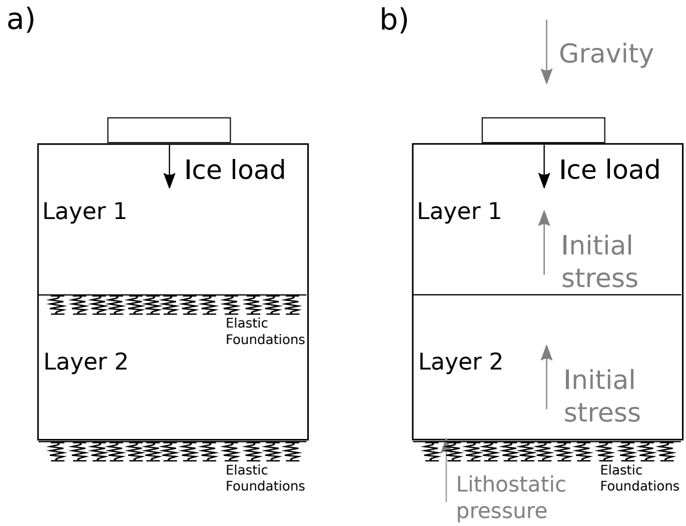

Figure 4.1: Schematic of a) the EF, and b) the NG model approaches. In grey are the forces and stresses specific to the NG approach.

The drawback of the EF method is that it is not possible to adapt the model to allow for compressibility (*Bängtsson and Lund*, 2008) as the internal buoyancy force is not represented in the stiffness matrix.

4.2.3. THE NG METHOD

The second approach was described by *Hampel et al.* (2019) using the 'geometrically non-linear formulation' (N) in Abaqus and also explicitly applying a gravitational force (G), which we will label as NG. This approach has been used in studies on the interaction between ice caps and faults (e.g., *Hampel and Hetzel*, 2006; *Hampel et al.*, 2009; *Turpeinen et al.*, 2008).

A complete description of how Abaqus solves the governing Equations is shown in Appendix A. In the current section, we start with the finite-element formulation of the momentum equilibrium, Equation S.10, and solve for the nodal displacements by employing Newton's method. At iteration increment k, the nodal displacements $\tilde{u}_M^k$ are assumed and the residual, $R_N(\tilde{u}_M^k)$, is calculated, where R_N is equal to the left hand side of equation S.10. If the residual is larger than a tolerance value, the residual is calculated again for a new increment: $\tilde{u}_M^{k+1} = \tilde{u}_M^k + \delta\tilde{u}_M$. Here $\delta\tilde{u}_M$ is calculated as follows (*Nguyen and Waas*, 2016):

$$\delta\tilde{u}_M = -\left(\frac{\partial R_N}{\partial \tilde{u}_M}\right)^{-1} R_N(\tilde{u}_M^k) = -K_{NM}^{-1} R_N(\tilde{u}_M^k). \tag{4.8}$$

Thus, for the Newton method used in a non-linear analysis of Abaqus, the Jacobian, $\frac{\partial R_N}{\partial \tilde{u}_M}$, of the FE equations is considered (*Hibbitt et al.*, 2016). This Jacobian is the stiffness matrix K_{NM}, which is sum of the stiffness matrix for the small-displacement analysis that is given by equation S.13, K^0_{NM}, the initial stress matrix, K^{σ}_{NM}, and the load stiffness matrix, K^L_{NM}:

$$K_{NM} = K^0_{NM} + K^{\sigma}_{NM} + K^L_{NM}. \tag{4.9}$$

The initial stress matrix is based on the current state of stress:

$$K^{\sigma}_{NM} = \int_{V_0} \boldsymbol{\tau}^c : \partial_N \boldsymbol{\beta}_M dV_0, \tag{4.10}$$

where $\boldsymbol{\tau}^c$ is the conjugate of the stress, and $\boldsymbol{\beta}_M$ the strain-displacement matrix. The load stiffness matrix is

$$K^L_{NM} = -\int_S \mathbf{N}^T_M \cdot \mathbf{Q}^S_N dS - \int_V \mathbf{N}^T_M \cdot \mathbf{Q}^V_N dV. \tag{4.11}$$

The two terms on the right hand side of equation 4.11 are the surface and volume load stiffness matrices, respectively. They include $\mathbf{Q}_N$, the variation of the surface and volume load vectors with the nodal variables, pre-multiplied by the transpose of the interpolation functions $\mathbf{N}_M$.

In short, Abaqus describes the basic FE equations in integral form using a stiffness matrix to describe the divergence of stress (first term in equation 4.1), an initial stress matrix for the stress-stiffening effects (i.e. to include buoyancy, second term in equation 4.1), and a load stiffness matrix for the dependence of gravity loading on the current density (i.e. to calculate the internal buoyancy, the third term in equation 4.1). The initial stress matrix and load stiffness matrix are only included in a non-linear analysis (Abaqus keyword NLGEOM, *Hibbitt et al.*, 2016). The procedure is non-linear as the stiffness matrix is now dependent on the displacement within the model.

Gravity loading needs to be applied explicitly to each layer (Table 4.1) for the correct calculation of the initial stress matrix (equation 4.10) and the load stiffness matrix (equation 4.11). As input for the gravity, we only need the value of the gravitational acceleration in the respective layer, and the associated changes in density are calculated automatically (*Freed et al.*, 2014). An initial stress and a lithostatic pressure are applied to prevent any model displacements to take place due to the gravity loading (Figure 4.1b) as in *Hampel et al.* (2019). For our multi-layer model, the initial stress in each layer is equal to the weight of the overlying layers:

$$\sigma_{N+1} = \sum_{i=0}^{N} \rho_i g_i h_i, \tag{4.12}$$

Method	Non-linear geometry with Gravity (NG)	Elastic Foundations (EF)
Forces	Ice load, Gravity	Ice load
Initial stress applied	Yes	No
Spin-up steps:	1. Static step (w/ gravity only)	-
	2. Viscous step (w/ gravity only)	-
Ice loading steps:	3. Static step (w/ ice load & gravity)	1. Static step (w/ ice load)
	4. Viscous step (w/ ice load & gravity)	2. Viscous step (w/ ice load)

Table 4.1: The differences between the NG and EF methods within Abaqus, see also schematic Figure 4.1.

with N the number of the layers, where $i = 0$ is the surface layer, and i increases for deeper layers. ρ_i, g_i, and h_i are the density, gravity, and thickness of the ith layer, respectively. For the uppermost layer ($i = 0$): $\sigma_0 = 0$. A lithostatic pressure is needed at the bottom of the model to simulate the initial stress in the core, which is calculated in the same way. An elastic foundation is present at the core-mantle boundary.

The usage of the NG approach requires two so-called spin-up steps before we apply an ice load (see Table 4.1 and *Hampel et al.* (2019)). This is necessary to obtain a stable pre-stressed equilibrium configuration. First we run a static step, in which only elastic behaviour is considered. In this step, the gravity balances the initial stress to minimize residual displacements. Following *Hampel et al.* (2019), we then run a viscous step of 10 thousand years (ka). After these two spin-up steps, an ice load is added and the loading scenario is performed. The run time of this approach is 5-10 min longer than a similar simulation that uses the EF approach, which does not require spin-up steps, on a total simulation time of 4-5 hours.

4.3. BENCHMARK SETUP

We use a spherical GIA model, labeled as SM, based on the normal mode method (NMM) for validation of the implementation of the FE models for radially symmetric Earth models. The SM model and the benchmark setup, i.e. the ice load and the Earth rheology and structure, are explained next. We identified 5 contributions for variations between the model results: (1) the difference in approach of the finite-element method (NG or EF), (2) the presence of sphericity, (3) the inclusion of self-gravity, (4) the different Earth models in the compressible runs, and (5) the approximation introduced by the FE method in general, which is controlled by the spatial resolution. Of these, contributions (4) and (5) are expected to have only a minor effect, and thus they are only briefly discussed in Sections 4.3.3 and 4.3.4, while the others represent the main goals of our investigation and these will be discussed in Section 4.4.

4.3.1. THE NORMAL MODE MODEL

In models that employ the Normal Mode Method (NMM), the variables are expanded in spherical harmonics and the system of differential equations is solved analytically in the spectral domain. The NMM is presented in detail in *Peltier* (1974) and *Wu and*

Name	Coord	ν	$\rho' g_0 \hat{r}$	$\rho_0 \nabla \phi'$	Figures
SM	Spherical	Table 3	Y	Y	4a, 5, 6
SM-I	Spherical	0.5	–	–	2, 3, 4a, 6
NG	Cartesian	Table 3	Y	N	4b, 5, 6
NG-I	Cartesian	0.5	–	–	2, 3, 4b
EF	Cartesian	Table 3	N	N	4c, 5, 6
EF-I	Cartesian	0.5	–	–	2, 3, 4c, 6

Table 4.2: The models employed in the study, the geometry, Poisson's ratio, terms included in each model, and the Figures in which the respective models appear. The letter "I" in the model name refers to incompressible models.

Peltier (1982). Self-gravity is included in the NMM model, meaning that the fourth term in equation 4.1 is included, and equation 4.3 is solved (Table 4.2).

The NMM code we use is ICEAGE (*Kaufmann*, 2004), described in *Kaufmann and Lambeck* (2000).The Green's functions represent the response functions and are derived from the viscoelastic load Love numbers determined by the code. All variables are expanded using spherical harmonics in order to solve the system of differential equations. The spherical harmonic expansion is truncated at degree 256, which corresponds to a spatial resolution of about 80 km. We tested the effect of the maximum spherical harmonic degree truncation on our results. Increasing the maximum spherical harmonic degree from 256 to 512 results in a maximum difference in horizontal deformation of only 0.01 m, situated around the ice edge (Figure 4.7). As the original displacements are several tens of meters in the horizontal, this effect is deemed insignificant. An overview of the models employed in this study is shown in Table 4.2.

4.3.2. THE LOADING SCENARIOS

Here we describe the loading scenario in the experiment to validate the method of *Hampel et al.* (2019) for cartesian multi-layer models. Respective changes are discussed in Section 4.4.2.

An ice load similar to that in *Spada et al.* (2011) is used, which is a pillbox with a constant thickness of 1,000 m and a fixed radius. We employ discs with five radii between 222 and 1,111 km, in 222-km steps, to test the effect of the extent of the ice sheet on the accuracy of the cartesian model. This is equivalent to roughly 2 to 10 latitudinal degrees, in 2-degree steps, respectively. The density of the ice is 931 kg/m^3. The load is applied instantaneously to the model (after the necessary spin-up in case of the NG model), after which a simulation is run for 10 ka during which the load remains on the model. The displacement results are evaluated after 10 ka of loading, to agree with the benchmark studies of *Spada et al.* (2011) and *Martinec et al.* (2018).

The models are all benchmarked for the disc load example with the respective Earth model of *Spada et al.* (2011) in Appendix C. The vertical displacements of the two FE models and SM match well with output from FastLove-HiDeg, a NMM implementation by *Vermeersen and Sabadini* (1997) and *Riva and Vermeersen* (2002) that has been benchmarked in *Spada et al.* (2011). Vertical displacements between FastLove-HiDeg and the respective models differ less than 3% for the 222 km radius ice load, and less than 2.5% for an ice sheet with a 1,111 km radius.

4.3.3. EARTH MODEL

The Earth model employed in the following experiments is determined by what we can employ in the compressible SM model. The ICEAGE code requires a high resolution of material parameter variations to suppress the growth of unstable Rayleigh-Taylor modes (*Hanyk et al.*, 1999; *Plag and Jüttner*, 1995; *Vermeersen and Mitrovica*, 2000) that may occur due to unstable density stratification induced by compressional deformation (*Wong and Wu*, 2019). In contrast, FE methods employ a rather coarse horizontal depth model with a few material parameter changes only to reduce the number of nodes and elements. Such a model with several tens of km thick homogeneous layers of constant density and bulk modulus would result in unstable conditions in compressible SM models. We employ the Preliminary Reference Earth Model (PREM, *Dziewonski and Anderson*, 1981) for the compressible SM, and use 8 layers with volume averages of the PREM values in all other models, including the incompressible SM (Table 4.3). The depths of the 8 layers are chosen to minimize the differences in the velocities due to different material-parameter layer approximations.

The presence of a density inversion in the volume averaged density profile requires a negative elastic foundation in the EF model. *Hampel et al.* (2019) outlined that this would be impossible in Abaqus. Indeed this cannot be done in the Abaqus/CAE frontend, but it can be done directly in the input file or by applying the foundation at the bottom face of the element above the boundary instead of the top face of the element below the boundary. As the negative density jump at 80 km is only 9 kg/m^3, we omit the use of an elastic foundation at this boundary in the EF model.

We quantified the effect of the Earth model approximation using incompressible models for the horizontal displacements and for the horizontal displacement rates in Appendix D. This difference will determine how well we can validate the cartesian NG model. Its effect fluctuates around 5% of the horizontal displacement for both the 222 and 1,111 km radius ice sheet, with a peak to at most 12% at the ice edge for the larger ice sheet. For the horizontal displacement rates, the effect is a bit less than 10% below the ice load, decreasing to 5% just outside of the ice edge.

4.3.4. RESOLUTION IN THE FINITE ELEMENT MODELS

The resolution selected in the FE model is a trade-off between accuracy and computation time. The vertical resolution is only 1 km in SM. In the FE models, it is not feasible to use as many layers. We ran several resolution tests and find that the results are most sensitive to the horizontal resolution. Differences are less than 1 m between a horizontal resolution of 27 and 54 km (0.25 and 0.5 lateral degrees, respectively). We therefore opt for a horizontal resolution of ~27 km and do not aim for a higher horizontal resolution. Furthermore, each of the 8 Earth layers is divided into 4 FE layers in the vertical direction.

Layer	From (km)	To (km)	Density (kg/m^3)	Young's modulus ($\times 10^{12}$ Pa)	Viscosity ($\times 10^{21}$ Pa s)	Gravity (m s^{-2})	Poisson's ratio
1	0	25	2,895.7506	0.1091	–	9.8356	0.2638
2	25	80	3,376.7141	0.1721	–	9.8499	0.2803
3	80	220	3,365.9506	0.1638	1	9.8862	0.2874
4	220	400	3,501.3442	0.1981	1	9.9424	0.3000
5	400	670	3,910.8079	0.2858	1	9.9968	0.2960
6	670	2,891	5,215.9378	0.6590	2	10.1826	0.2974
7	2,891	5,149.5	10,750	0	0	7.1302	0.5000
8	5,149.5	6,371	13,000	0.4721	0	2.0626	0.4437

Table 4.3: The Earth model parameters for the 8 layer configuration. Values are volume averages derived from PREM. The depth is defined positive downwards.

We use this resolution in the region covering the inner 2,200 km of the model. The total width of the model is 20,000 km, and the outer region has a coarser resolution of ~550 km (5 degrees in lateral extent). This setup with a higher resolution in the region below and close to the ice sheet is similar to the setup of the cartesian models in *Schotman et al.* (2008) and *Marsman et al.* (2021). Using 16 cores, a computation time is achieved of roughly 4-4.5 hours for the incompressible and material compressible simulations, and 4.5-5 hours for the compressible NG runs. We make use of hexahedral, 8 node elements of type C3D8H for the incompressible models and C3D8 for the compressible models (including models using material compressiblity).

4.4. RESULTS

Hampel et al. (2019) showed that the NG method works for incompressible homogeneous half space models and for incompressible shallow (i.e. 100 km deep) cartesian models consisting of two layers. In principle, the NG method is suitable to deal with compressibility, and this was tested for the shallow two layer cartesian models (*Hampel et al.*, 2019). To allow the usage of the method to model glacial loading scenarios, the model needs to include a lithosphere and the mantle down to the core-mantle boundary. We extend their model to the core of the Earth by incorporating the 8-layer approximation, and make the model compressible by changing Poisson's ratio to the values listed in Table 4.3. We apply a disc load of 1,111 km (as described in Section 4.3.2), and compare the horizontal displacement of the NG and EF models against results from SM to understand the differences.

We distinguish three forms of compressibility: (1) full compressibility including the effect of compressibility on self-gravity in equation 4.3, (2) full compressibility without self-gravity, and (3) material compressibility (*Klemann et al.*, 2003). The full compressible models differ from the material compressible model in that they include the internal buoyancy force in the equation of motion (equation 4.1). The compressible version of SM simulates (1), NG reproduces (2), and EF can only include (3).

4.4.1. DISPLACEMENTS

INCOMPRESSIBLE MODEL RESULTS

First, we investigate three effects mentioned at the start of Section 4.3: the approach taken by the FE method, sphericity, and self-gravity. We isolate the first effect by comparing results from the EF-I and NG-I models. Comparing these cartesian models with SM then gives us the combined effect of the second and the third. *Amelung and Wolf* (1994) noted that self-gravity compensates for the sphericity in the vertical. We examine if such a compensation is also present in the horizontal.

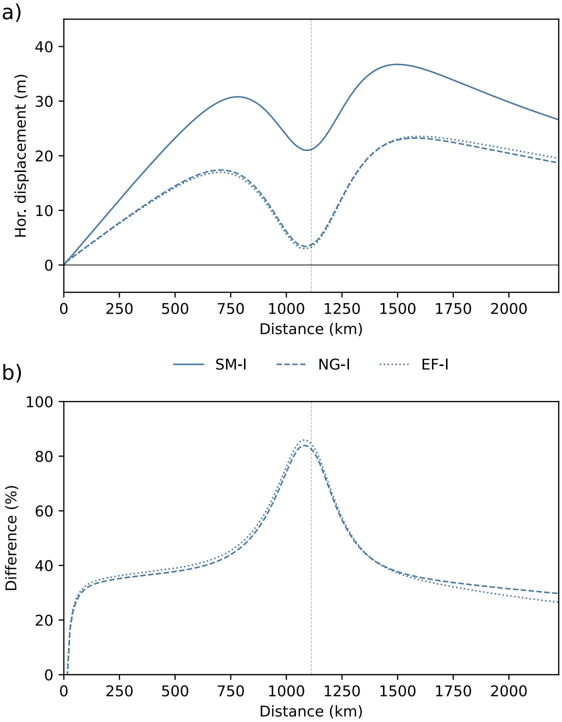

Figure 4.2: Horizontal displacement after 10 ka of loading using an ice load 1,111 km in radius for (a) SM-I, NG-I, and EF-I, and (b) the difference in percentage of NG-I and EF-I with SM-I. The edge of the ice load is marked by a vertical grey dashed line.

Horizontal displacements underneath and outside of the ice sheet are positive (outwards) after 10 ka of loading with a 1,111 km radius ice sheet for all models, with a (local) minimum at the ice sheet boundary (Figure 4.2). During loading, the mantle flow is outwards from the center of loading resulting in positive displacements, while lithospheric flexure results in a motion towards the center of the ice sheet (*O'Keefe and Wu*, 2002). Horizontal lithospheric flexure is largest at the ice sheet boundary, explaining the location of the (local) minimum. The maximum value of the horizontal displacement is found outside of the ice sheet, and ranges from 20 m for NG-I and EF-I to more than

35 m for SM. Overall, the cartesian models EF-I and NG-I are found to be in excellent agreement, especially in the near field (Figure 4.2a). Therefore, we conclude that the approach taken by the FE method only leads to insignificant changes using a complete Earth model from the surface of the Earth down to the core-mantle boundary.

To investigate the effect of sphericity and self-gravity we compare the cartesian models with SM in Figure 4.2b. We observe a significant difference in simulated horizontal displacement of about 40% below the load, increasing to more than 80% at the load edge (Figure 4.2b). Thus, where self-gravity partially compensates for the sphericity in the vertical (*Amelung and Wolf*, 1994), this is not the case for the horizontal. In the next section we test if a better agreement can be obtained using a smaller ice sheet, which minimises the effects of self-gravity (*Pollitz*, 1997) and sphericity.

DISPLACEMENTS FOR A SMALL ICE SHEET

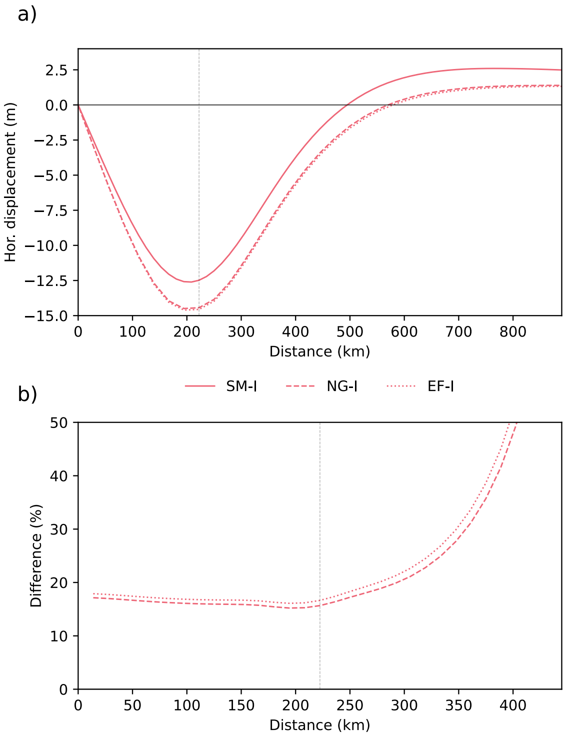

Figure 4.3: a) Horizontal displacement after 10 ka of loading as simulated by SM-I, NG-I, and EF-I, and b) the difference of NG-I and EF-I with SM-I. The dashed and dotted lines are on top of each other in Figure a. The edge of the ice load is marked by a vertical grey dashed line.

With an ice sheet 222 km (2 degrees) in radius, the modelled horizontal displacements are inwards below the ice sheet. This is a result of the lithospheric flexure that is dominant for an ice sheet with a small lateral extent. The displacements are smaller in magnitude, and only -15 m at most (Figure 4.3a). Differences between the incompressible cartesian and spherical models are less than 20% below the load (Figure 4.3b). For such a small ice sheet, the agreement between cartesian and spherical models has significantly improved compared to the largest ice sheet of this study.

THE EFFECT OF COMPRESSIBILITY ON THE DISPLACEMENTS

To understand the effect of the different approximations for compressibility, we compare the incompressible and compressible simulations. In all models, the effect is most pronounced at the ice margins, which is also illustrated by the volumetric strain in Appendix F (Figure 4.13). This figure shows the dilatation of the elements and is thereby a measure of the relative magnitude of compressibility. An increasing effect is seen for larger ice sheets in SM and NG, but not for EF (Figure 4.4). Evidently, including the internal buoyancy force leads to an increasing effect below and further outside the load. For the smallest ice sheet, the effect of compressibility in NG and SM is circa 5 and 6 m, respectively (on a total deflection of 20-40 m). For larger ice sheets, this effect increases to almost 25 m in both models. The resulting compressibility effect of SM and NG agrees to a large extent, but also exhibits minor differences, which are caused by the different Earth model and by the resolution, possibly combined with the effect of self-gravity on compressibility which is included in SM but not in NG.

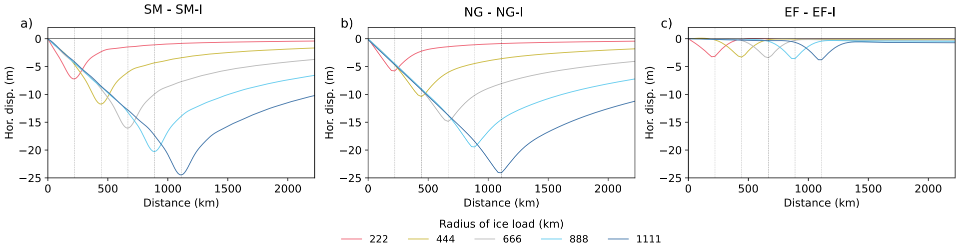

Figure 4.4: The effect of compressibility on the modelled horizontal displacements in (a) SM, (b) NG, and (c) EF. SM-I uses the PREM Earth model, just like SM. The edges of the ice loads are marked by vertical grey dashed lines.

The effect of material compressibility on the horizontal displacement for EF is at most 3-4 m, independent of the size of the ice sheet (Figure 4.4c). Its effect peaks around the ice edge, where the density change due to deformation is largest (Figure S7). This is also where the flexure in the lithosphere is largest as this is where the slope in the vertical displacement is at its maximum. For small ice sheets, the material compressible EF model performs similar to the other compressible models. However, as the size of the ice sheets increase, the agreement deteriorates. Based on Figure 4.4, we conclude that material compressibility only approximates compressibility for small ice sheets, although NG outperforms EF even for such small ice sheets.

COMPRESSIBLE MODEL RESULTS

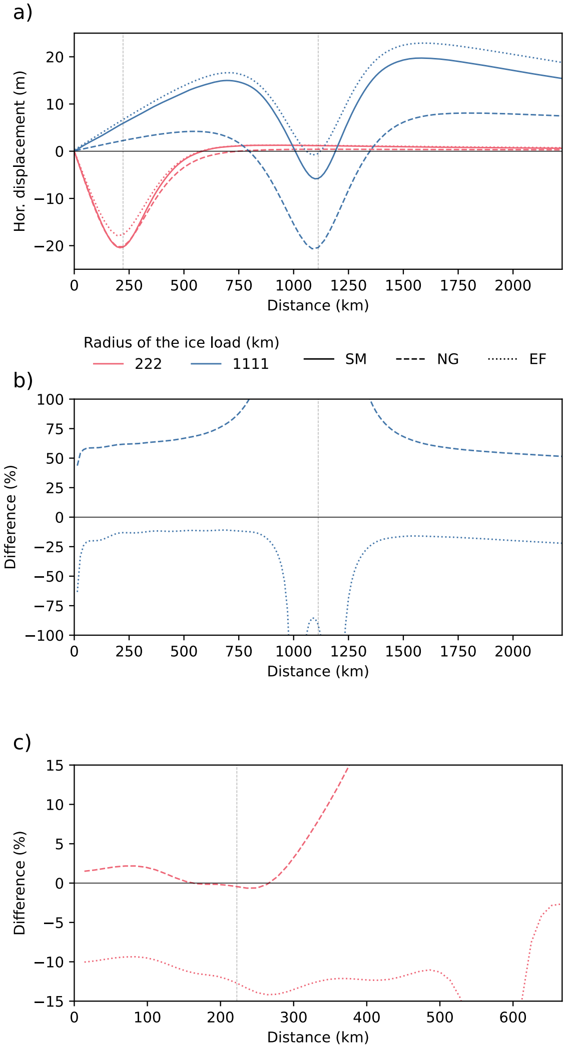

Figure 4.5: (a) Horizontal displacement after 10 ka of loading using ice loads 1,111 and 222 km in radius for SM, NG, and EF, as well as the difference of NG and EF with SM for (b) the 1,111 km and (c) 222 km radius ice sheets. The edges of the ice loads are marked by vertical grey dashed lines.

With all the information from the previous section we are now able to explain Figure 4.5 which shows the horizontal displacement of compressible and material compressible models after 10 ka of loading with an ice sheet 1,111 km in radius. Differences with respect to SM are smaller for EF (mostly less than 15% below the load) than for NG (50% almost everywhere, Figure 4.5b). The approximation of compressiblility as material compressibility in EF leads to a decent agreement with the spherical model. The lack of full compressibility in this approximation partly compensates for the lack of sphericity, leading to a better apparent agreement even though compressibility is modelled less accurately. Furthermore, we notice that for the 222 km radius ice sheet NG indeed matches the SM results better than EF (Figure 4.5c). The advantage of NG simulating compressibility better than EF is unfortunately diminished by the effect of sphericity, and thus the NG approach is less applicable for modelling large ice sheets.

4.4.2. HORIZONTAL DISPLACEMENT RATES

The total horizontal displacement due to GIA cannot be observed, while the rate in horizontal displacement (the velocity) can be measured using Global Navigation Satellite Systems (GNSS) stations. Therefore we focus on the rates in the remainder, and assess the magnitude of modelling approximations.

We aim to develop a case study that is representative for GIA in Iceland, Alaska, and NAP. Based on studies of those regions (e.g., *Árnadóttir et al.*, 2009; *Elliott et al.*, 2010; *Hu and Freymueller*, 2019; *Nield et al.*, 2014; *Pagli et al.*, 2007), we select an elastic thickness of 80 km, and between 80 km and 220 km we consider a low viscosity layer of 1×10^{19} Pa s. Below this layer down to 670 km, we employ an upper mantle viscosity of 4×10^{20} Pa s, the same value as in *Fleming et al.* (2007), *Larsen et al.* (2005), and *Elliott et al.* (2010). The lower mantle viscosity (below 670 km) is 1×10^{22} Pa s. The ice load has a radius of 222 km, just as before in this paper. Due to the small extent of the load, GIA is mainly sensitive to the upper layers, and the exact value of the lower mantle viscosity is less important (*Fleming et al.*, 2007; *Sato et al.*, 2011). We employ the PREM Earth model values for both incompressible and compressible SM simulations, and a layered Earth model with volume averages in the cartesian models. The thickness of the ice cap has been tuned so that the modelled vertical rates match the peak uplift rates observed in Alaska of 30 – 35 mm/a (*Larsen et al.*, 2005). A good fit has been found for an ice cap thickness of 200 m.

To start, we simulate 2 ka of loading. *Fleming et al.* (2007) concluded that the influence of Last-Glacial Maximum ice loads was negligible over Iceland. In combination with the low viscosity profile employed, we deem 2 ka of loading to be sufficient to reach equilibrium for our case studies. We will assume equilibrium with the load prior to unloading, and then calculate the displacement rates after 205 years of unloading. The rates are calculated as the difference between 200 and 210 years after unloading, divided by 10 years. We use a spin-up of 10 ka in the NG simulations as described in Section 4.3.2, although we expect that this could be shorter (e.g. 2 ka) due to the presence of a low viscosity layer in that simulation. The runtime is 3-3.5 hours for the incompressible simulations, and 6-6.5 hours for the compressible NG run. In SM, runtimes are only a few seconds.

Modelled horizontal displacement rates reach values of 5-7 mm/a, similar to those modelled by *Elliott et al.* (2010) for Alaska. The largest displacement rates of up to 6.8 mm/a are found for SM (Figure 4.6a.). We use SM as a reference, and compare it with all other models in Figure 4.6b. The effect of compressibility on the horizontal can be seen by comparing SM and SM-I, and amounts to about 1.5 mm/a at most, again showing that the effect of compressibility is not negligible in the horizontal (*James and Lambert*, 1993;

Mitrovica et al., 1994a; *Tanaka et al.*, 2011).

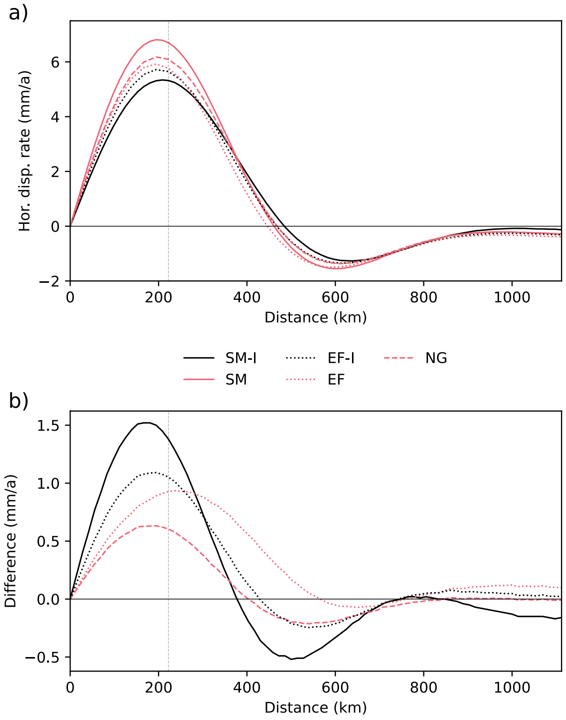

Figure 4.6: Horizontal displacement rate for (a) SM, SM-I, NG, EF, and EF-I, and (b) differences of the respective models with SM. The edge of the ice load is marked by a vertical grey dashed line.

The cartesian models all simulate displacement rates that differ less than 1.1 mm/a from SM (Figure 4.6b). Differences are 0.93 mm/a for the EF model, and 0.63 mm/a for the NG model. However, the maximum in the difference to the EF model has also moved in the horizontal direction (it is now outside the load). This model nevertheless provides a minor improvement with respect to EF-I, although not as much as the NG model.

These modelling technique-dependent differences can still be considered significant when compared to current precision and uncertainties of GNSS observations. *Kierulf et al.* (2021) show that horizontal velocities of GNSS networks can reach such precision already after 2-3 years of observations. Uncertainties of horizontal velocities meanwhile reach 0.5 mm/a for global GNSS solutions (*Vardić et al.*, 2022) and, depending on the chosen noise model and further corrections, can be much less than 0.35 mm/a for regional ones (*Kierulf et al.*, 2021; *Lahtinen et al.*, 2019).

4.5. STEPS TOWARDS A COMPRESSIBLE SPHERICAL FINITE ELEMENT MODEL

Modelling the whole GIA process eventually requires including sea-level changes induced by the ice mass changes and the deformation, and their effect on deformation itself. Such interactions must be solved on a global scale with a spherical model. This spherical model should ideally allow the implementation of lateral heterogeneous material parameters. Several fully or partially compressible spherical 3D models have already been developed. *Latychev et al.* (2005) implemented compressibility in a 3D GIA model, but only elastic compressibility was included. *Martinec* (2000) developed a spectral finite-element model for 3D visco-elastic relaxation in a spherical Earth, which was extended by *Tanaka et al.* (2011) to allow for compressibility. A 3D finite-element (FE) model by *Zhong et al.* (2003) was ameliorated by *A et al.* (2013) to achieve a fully compressible 3D FE model. *Wong and Wu* (2019) introduced a new approach by calculating separately the change in body forces due to compressibility in iteration with the FE model. However, their approach is not yet applicable for realistic loadings.

As the NG method is able to represent the compressible effects in a straight-forward way, we try to implement the NG method in spherical FE models. However, the limiting factor turns out to be the explicit application of gravity loading. Gravity can be defined in the vertical direction for a cartesian model, but Abaqus does currently not have the option for gravity to be directed radially inward as is the case for a spherical body. Gravity can of course be implemented separately as a body force that is directed radially inward, but for the magnitude of the body force we need to manually compute the density, which changes as a result of compressibility (third term in equation 4.1). In principle, we can calculate the dilatation and the corresponding density change for every time step and iterate. If we were to do this, we lose the advantage of the NG method, namely that Abaqus includes the load stiffness matrix (equation 4.11), and thereby automatically considers changes in density associated with changes in pressure (*Freed et al.*, 2014). We suggest that, for complete simulations for a compressible spherical model, approaches such as those in *Wong and Wu* (2019) should be used, who solve the differential equations iteratively and apply the change in body force due to compressibility.

4.6. CONCLUSION

Cartesian models of Glacial Isostatic Adjustment (GIA) previously generated by Abaqus have neglected compressibility. Here, we extended a method for including compressibility in FE models using a geometrically non-linear formulation with explicit application of gravity (*Hampel et al.*, 2019), named NG. The method has the advantage that it includes compressibility in line with the GIA equation of motion. Compressibility (without self-gravity) is accounted for including the effect of dilatation on buoyancy forces when we decrease Poisson's ratio below that of incompressible materials. We investigated the effect of two assumptions made in earlier studies, namely incompressibility and a cartesian Earth model (e.g., *Árnadóttir et al.*, 2009; *Ivins and James*, 1999; *Larsen et al.*, 2003, 2004; *Pagli et al.*, 2007; *Schotman et al.*, 2008; *Zwinger et al.*, 2020). We also investigate material compressibility in the conventional method (e.g., *Auriac et al.*, 2013; *Kaufmann et al.*, 2005; *Lund et al.*, 2009; *Marsman et al.*, 2021; *Nield et al.*, 2018; *Steffen et al.*, 2006), which allows for material compression, but does not include the internal buoyancy force in the equation of motion. The conventional method has been named as EF.

We considered the spherical normal mode model SM to simulate the full effect of compressibility, and tested the effect of compressibility and material compressibility in the FE models NG and EF against it. The absolute effect of compressibility on the horizontal displacement is most evident at the ice margins, and increases for larger ice sheets in SM and NG. The effect of compressibility in the material compressible EF model shows no dependence on the size of the ice sheet, which indicates that compressibility is not represented well. For ice sheets below roughly 200 km in radius, only considering material compressibility in the constitutive equation (Hooke's law) is a reasonable approximation of full compressibility, although NG performs better even for small ice sheets. At the same time sphericity is found to be important for simulations that aim to model the horizontal displacement rates, and it can only be neglected for small (maximum ~200 km radius) ice sheets. While sphericity and self-gravity at least partly compensate each other in the vertical, we find that there is no such compensation for horizontal displacements. For larger ice sheets, horizontal displacements simulated by material compressible EF models perform better than compressible NG models as the missing full compressibility is partly compensated with the lack of sphericity.

We investigated the applicability of the cartesian models in small scale GIA studies with large uplift rates due to recent unloading by simulating the horizontal displacement rates for a scenario representative for post-LIA uplift in Iceland, Alaska, and West Antarctica. Horizontal displacement rates of compressible and material compressible cartesian models differ from SM by 0.63 and 0.93 mm/a, for NG and EF respectively. SM-I differs by 1.5 mm/a, and therefore performs worse than the cartesian models, highlighting the importance of using compressibility for modelling horizontal velocities of small-scale GIA. To conclude, we show that for small ice sheets results from cartesian models are sufficiently close to results when the full GIA equation of motion (including self-gravity) is solved, and the compressible cartesian NG model approach is acceptable (Table 4.4).

Since most GNSS observations are available for long time spans even in such small-scale regions like Alaska, Iceland and NAP, the appropriate modelling approach has to be chosen before a comparison of modelled vs. observed horizontal velocities can be made. We see that for an ice sheet with a 222 km radius, the accuracy of the NG model is slightly above any GNSS precision and uncertainty. Hence, only smaller ice caps should be modelled with cartesian NG models when fitting horizontal velocities is the goal.

Horizontal displacement rates are sensitive to mantle viscosity, and much can be learned from investigating them in small scale study areas like Alaska, Iceland, or West Antarctica (e.g., *Árnadóttir et al.*, 2009; *Marsman et al.*, 2021; *Samrat et al.*, 2020). We tested the effect of compressibility in 1D models, but the cartesian models can accomodate 3D subsurface structures that are likely to exist. Finally, we attempted to implement the NG method in a spherical FE model, but found that the advantage of this method is lost, as a radial gravity distribution cannot be specified in Abaqus. Therefore, the change in buoy-

Name	Coord	Can lateral variations be included?	Approximate computation time	Difference with SM (2 deg radius load)	Difference with SM (10 deg radius load)
SM	Spherical	N	∼ seconds to few minutes	-	-
NG	Cartesian	Y	3-3.5 hours (incompressible) Up to 6.5 hours (compressible)	hor disp: <2.5% rate: 0.63 mm/yr	hor disp: >50%
EF	Cartesian	Y	3-3.5 hours (material compressible and incompressible)	hor disp: 10-15% rate: 0.93 mm/yr	hor disp: <25 %

Table 4.4: An overview of the models in this study, where they are applicable and their computation time. The values for the differences with SM are shown below the load for the compressible and material compressible simulations for NG and EF, respectively.

ancy forces would have to be calculated outside the FE software as done by e.g. *Wong and Wu* (2019), confirming the finding of *Bängtsson and Lund* (2008) that it is impossible to calculate the buoyancy force inside the FE software.

4.7. APPENDIX A: SOLVING THE EQUATIONS IN ABAQUS

The governing equations are solved using a different solution method for the NG method. To be able to explain the differences with the EF method, we review how the finite element equations are solved within Abaqus. Abaqus solves for the following equation of motion (*Hibbitt et al.*, 2016):

$$\nabla \cdot \boldsymbol{\tau} + \mathbf{f} = 0, \tag{4.13}$$

where **f** are the body forces. The equation of motion is solved using the weak formulation which replaces the equations for each of the three directions by a single equation. In order to generate the weak formulation, we multiply equation 4.13 by a test function, here considered to be the 'virtual' velocity field $\delta\mathbf{v}$, which is an arbitrary field of sufficient continuity, and integrate over the domain. After some algebra we obtain:

$$\int_S \mathbf{t} \cdot \delta\mathbf{v} + \int_V \mathbf{f} \cdot \delta\mathbf{v} dV = \int_V \boldsymbol{\tau} : \boldsymbol{\delta D} dV. \tag{4.14}$$

Here, **t** is the surface traction per unit area at any point on the surface S, defined as $\mathbf{t} = \mathbf{n} \cdot \boldsymbol{\tau}$. Furthermore, $\boldsymbol{\delta D} = \mathrm{sym}\{\nabla \delta\mathbf{v}\}$, the symmetric part of the virtual velocity gradient. $\boldsymbol{\delta D}$ is also known as the virtual strain rate or the virtual rate of deformation. The colon ':' is the double dot product for tensors, where $\boldsymbol{A} : \boldsymbol{B} = A_{ij} B_{ij}$. We can replace the Cauchy stress tensor $\boldsymbol{\tau}$ and the virtual strain rate $\boldsymbol{\delta D}$ in equation 4.14 by any conjugate pairing of stress and strain, and choose a stress and strain that are defined relative to a reference volume V_0 (*Hibbitt et al.*, 2016). We arrive at the following equation:

$$\int_S \mathbf{t} \cdot \delta\mathbf{v} + \int_V \mathbf{f} \cdot \delta\mathbf{v} dV = \int_{V_0} \boldsymbol{\tau}^c : \boldsymbol{\delta\epsilon} dV_0. \tag{4.15}$$

Here, $\boldsymbol{\delta\epsilon}$ is the virtual strain rate associated with $\delta\mathbf{v}$, and $\boldsymbol{\tau}^c$ is the conjugate stress. The specific strain rate that we use for $\boldsymbol{\delta\epsilon}$ depends on the individual elements. Equation 4.15 is then discretized by introducing shape functions **N** for the deformations **u**. For simplicity, we show the case for only two dimensions, so **u** contains $u(x,y)$ and $v(x,y)$ for the nodal displacement in x and in y, respectively. We get for eight nodal elements:

$$u(x,y) \approx \sum_{N=1}^{8} N_N(x,y)\tilde{u}^N, \tag{4.16}$$

$$v(x,y) \approx \sum_{N=1}^{8} N_N(x,y)\tilde{v}^N. \tag{4.17}$$

Here u_i and v_i are the displacement at the nodes. In matrix form:

$$\mathbf{u} = \begin{Bmatrix} u(x,y) \\ v(x,y) \end{Bmatrix} = \left[\begin{array}{cc|cc|cc} N_1 & 0 & N_2 & 0 & \cdots & \cdots \\ 0 & N_1 & 0 & N_2 & \cdots & \cdots \end{array} \right] \left\{ \begin{array}{c} u_1 \\ v_1 \\ \hline u_2 \\ v_2 \\ \hline \vdots \\ \vdots \end{array} \right\}. \tag{4.18}$$

Similarly, we obtain for the virtual velocity field $\delta\mathbf{v}$:

$$\delta\mathbf{v} = \mathbf{N}_N \widetilde{\delta v}^N. \tag{4.19}$$

Here $\mathbf{N}_N$ are the shape functions of row N, and $\widetilde{\delta v}^N$ is the Nth element of the virtual velocity field at the nodes. $\boldsymbol{\delta\epsilon}$ is equal to

$$\boldsymbol{\delta\epsilon} = \boldsymbol{\beta}_N \widetilde{\delta v}^N, \tag{4.20}$$

where $\boldsymbol{\beta}_N$ is the strain-displacement matrix. It is the derivative of $\mathbf{N}_N$ with respect to the position:

$$\boldsymbol{\beta}_N = \begin{bmatrix} \frac{\partial N_N}{\partial x} & 0 \\ 0 & \frac{\partial N_N}{\partial y} \\ \frac{\partial N_N}{\partial y} & \frac{\partial N_N}{\partial x} \end{bmatrix}. \tag{4.21}$$

We get from equation 4.15 after cancelling the common factor $\widetilde{\delta v}^N$:

$$\int_{V_0} \boldsymbol{\beta}_N : \boldsymbol{\tau}^c \, dV_0 - \int_S \mathbf{N}_N^T \cdot \mathbf{t} \, dS - \int_V \mathbf{N}_N^T \cdot \mathbf{f} \, dV = 0. \tag{4.22}$$

Here the superscript T refers to the transpose of $\mathbf{N}_N$. We can work this out further, using the definition for $\boldsymbol{\tau}^c$:

$$\boldsymbol{\tau}^c = \mathbf{H} : \boldsymbol{\beta}_M \tilde{u}^M. \tag{4.23}$$

Here, $\mathbf{H}$ is a fourth order tensor containing material properties which is the proportionality constant in the stress-strain relation, and the summation is over node M. The equation of motion is now as follows:

$$\tilde{u}^M \int_{V_0} \boldsymbol{\beta}_N : \mathbf{H} : \boldsymbol{\beta}_M dV_0 = \int_S \mathbf{N}_N^T \cdot \mathbf{t} dS + \int_V \mathbf{N}_N^T \cdot \mathbf{f} dV, \tag{4.24}$$

which is of the form $K_{NM} u_M = f_N$ solved by the FE software Abaqus, with K_{NM} the stiffness matrix:

$$K_{NM} = \int_{V_0} \boldsymbol{\beta}_N : \mathbf{H} : \boldsymbol{\beta}_M dV_0. \tag{4.25}$$

This stiffness matrix is used by the Elastic Foundations method.

4.8. APPENDIX B: SENSITIVITY TO THE SPHERICAL HARMONIC TRUNCATION LIMIT

Normal mode model SM-I uses spherical harmonic (SH) degrees in the horizontal direction. In the main paper, the maximum amount of SH degrees is 256. Here, we test how much more accurate a cut-off degree of 512 is for our results in the horizontal. Increasing the maximum SH degree from 256 to 512 only improves our results by 0.01 m at most, with this maximum difference situated around the ice edge (Figure 4.7). The maximum horizontal displacement is -11 m, and thus this difference is deemed insignificant for the results of this study.

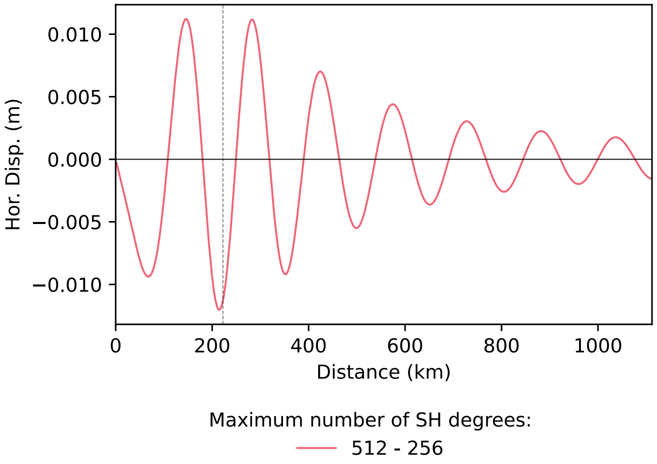

Figure 4.7: Difference in modelled horizontal displacement after 10ka of loading with a disc load 222 km in radius.

4.9. APPENDIX C: SPADA ET AL. (2011) BENCHMARK

Our first benchmark was with results using the Earth model described in *Spada et al.* (2011). For this benchmark, we also used AFCAL, a spherical FE code that has been benchmarked in *Martinec et al.* (2018), and FastLove-HiDeg, a normal mode code which is validated in *Spada et al.* (2011). These two models are described in more detail below. The simulations for this benchmark consists of 4 Earth layers (5 boundaries), each divided into 12 FE elements in the vertical direction for the box models. Using 16 cores, a computation time is achieved of 16-18 hours for the incompressible runs with the box models. We compare the vertical displacement and subtract the value in the far field from the FE model results, as both FE box models in this study differ by about 1.5 meters in the far field. We perform this correction in the same way as *Hampel et al.* (2019), and the output of the box models is hence shown with respect to the upper right corner of the model.

4.9.1. MODELS USED FOR THE BENCHMARK

AFCAL

The AFCAL model is a spherical axisymmetric FE model using elastic foundations (*van der Wal et al.*, 2010; *Wu and van der Wal*, 2003), and is used in benchmark A of *Martinec et al.* (2018). The viscous deformation is computed by ABAQUS, and the self-gravity is calculated by solving for the gravitational potential using the SH method in the Laplace domain. It contains a tangential resolution of 0.0625 degrees and a radial resolution of at least 4 elements per layer, double than what is used in *Martinec et al.* (2018), as the deformation due to the 2 degree load is found to be sensitive both to horizontal and the vertical resolution. Poisson's ratio is set to 0.495, in order to prevent volumetric locking. The change in gravitational potential is applied as a force at the boundaries for the next iteration (as in *Wu*, 2004). Four iterations are used, as was also done in *Martinec et al.* (2018).

FASTLOVE-HIDEG

The normal mode code FastLove-HiDeg uses the multilayer matrix propagation method (*Vermeersen and Sabadini*, 1997), and has been benchmarked in *Spada et al.* (2011). This model will be used as a reference for all the other incompressible models. 512 SH degrees are used for the computation. The horizontal resolution of the model is 0.03125 degrees, which is mostly an oversampling, since the resolution is effectively determined by the amount of SH degrees available in the model.

4.9.2. RESULTS

The NMM codes SM-I and FastLove-HiDeg match excellently, and differences are everywhere below 1% (Figure 4.8). The residual in the vertical displacement between the spherical FE model peak at the edge of the ice sheet with values just below 3%.

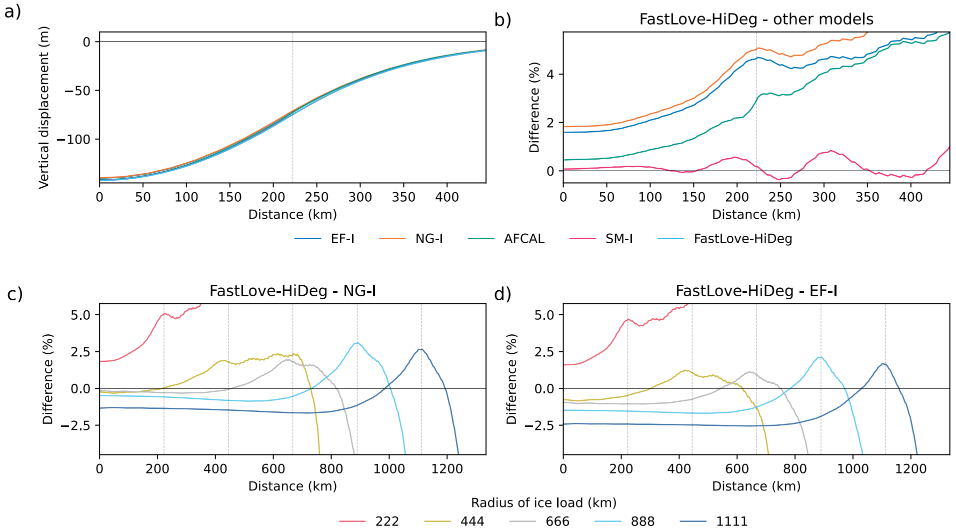

Figure 4.8: Vertical displacement for the incompressible models for a disc 2 degrees in extent (a), as well as the difference in vertical displacement rate with FastLove-HiDeg (b). The bottom subplots show the difference in vertical displacement between FastLove-HiDeg and NG-I (c) and box-EF (d), respectively, for discs with 5 different radii. The ice edges are denoted by the dashed vertical lines.

The vertical displacements for the box models are expected to differ a little from the spherical models, but still match well, with differences below 3% under the ice sheet for four out of 5 ice sheet simulations. This is in agreement with *Amelung and Wolf* (1994) and *Wu and Johnston* (1998), who found that box models provide an acceptable level of accuracy in the vertical for ice sheets the size of the Fennoscandian ice sheet.

4.10. APPENDIX D: SENSITIVITY TO THE EARTH MODEL

The compressible spherical model SM needs many layers to be stable. Because of this, it employs PREM, with a resolution of 1 km in the vertical. This inherently results in differences compared to models that employ constant layer values, like Abaqus. The constant layer values can be approximated in SM-I, and compared with the incompressible PREM Earth model. This way, we can obtain more information on the sensitivity to the Earth model. Using the 10 ka loading scenario, differences in the horizontal displacement are fluctuating between 5 and 7% for the 222 km and 1,111 km radius ice sheet, with a peak of 12% around the ice edge for the simulation with the larger ice sheet (Figure 4.9). Using the unloading scenario for the horizontal displacement rates, differences are found to be up to 10% close to the load center, decreasing to 5% just outside of the load (Figure 4.10).

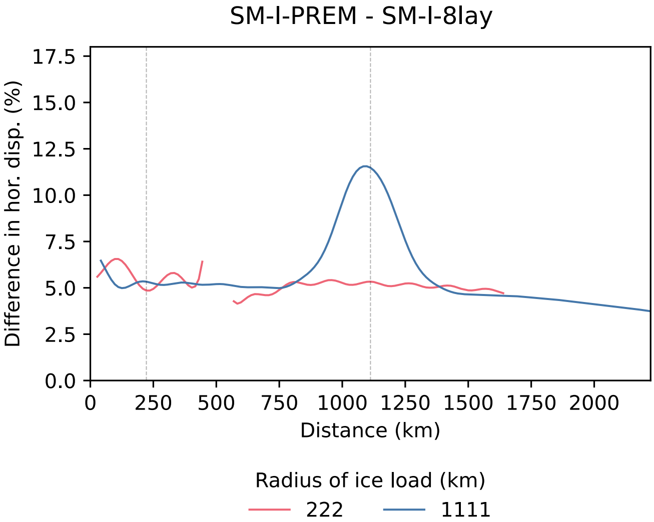

Figure 4.9: Difference in horizontal displacement due to the Earth model approximation for the incompressible ICEAGE model, using 10 ka of loading. When the absolute value of the original signal is below 1.5m, the values are masked.

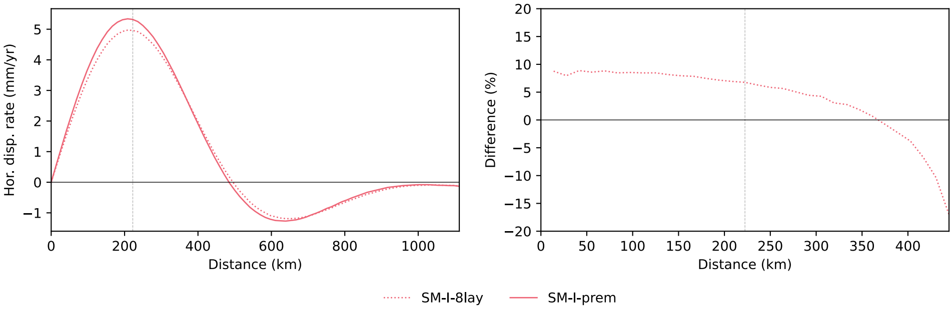

Figure 4.10: Using the unloading scenario, (a) simulated horizontal displacement rate, and (b) differences in horizontal displacement rate due to the Earth model approximation for the incompressible ICEAGE model.

4.11. APPENDIX E: SENSITIVITY TO THE RESOLUTION OF THE FEM MODEL

We test the effect of the vertical and horizontal resolution in our finite element models NG-I and EF-I. The vertical resolution shows little sensitivity to an increase in the vertical amount of seeds in a layer (Figure 4.11). There appears to be a little more sensitivity in NG-I as compared to EF-I, especially in the far field. We opt for 4 vertical seeds per Earth model layer in our box models, as 5 vertical seeds is deemed unnecessary, and models with a resolution of 4 vertical seeds per Earth layer can still be run within reasonable computation time (~ 4 hours).

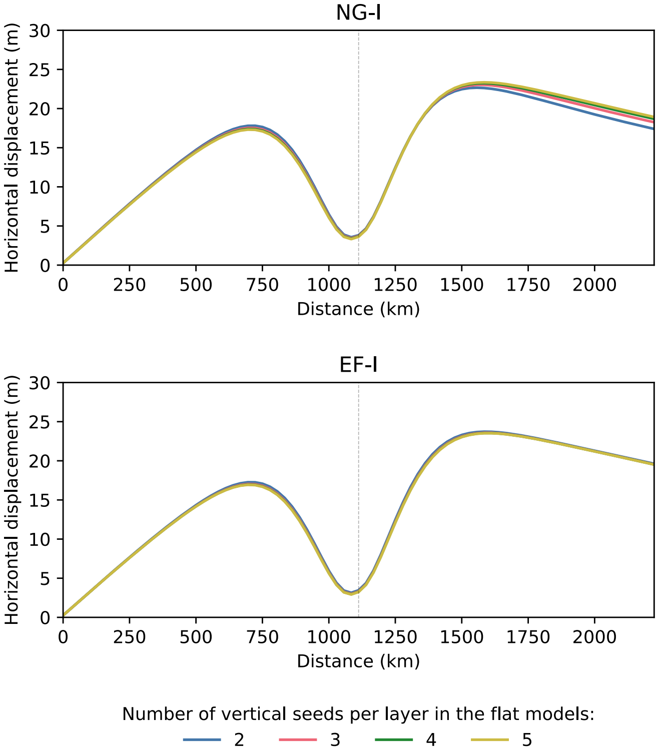

Figure 4.11: Difference in horizontal displacement after 10ka of loading for NG-I (a) and EF-I (b) due to changing the amount of elements per layer, for the 1111 km radius disc load.

The horizontal resolution shows a higher sensitivity to the modelled horizontal displacement, and a clear visual improvement can be seen in Figure 4.12 when increasing the horizontal resolution in the high resolution region from 222 km to 27 km. NG-I and EF-I exhibit an almost identical sensitivity to the horizontal resolution. We decided to employ the finest horizontal resolution tested (27 km) in all other simulations of this paper.

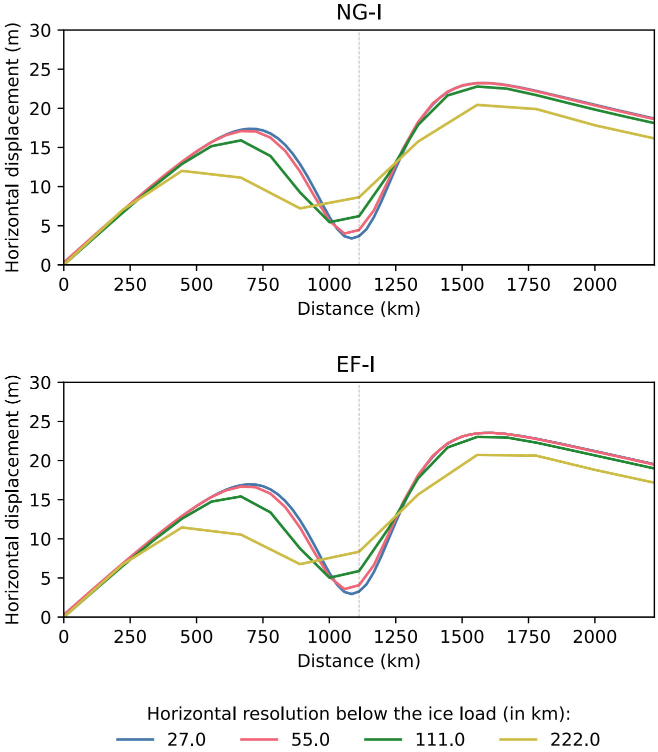

Figure 4.12: Difference in horizontal displacement after 10ka of loading for NG-I (a) and EF-I (b) due to changing the horizontal resolution below the load, for the 1111 km radius disc load.

4.12. APPENDIX F: VOLUMETRIC STRAIN AFTER 10KA OF LOADING IN THE NG MODEL

Compressibility is related to the dilatation of the elements, and the corresponding increase or decrease in density, assuming that the mass of each element is conserved. Therefore, we plot the volumetric strain, $\frac{\Delta V}{V}$, which is calculated as the sum of the three diagonal strain components:

$$\frac{\Delta V}{V} = \epsilon_{11} + \epsilon_{22} + \epsilon_{33} \tag{4.26}$$

There is compression under the ice load and expansion just outside of the ice load. The minimum value of -15 for the volumetric strain implies a density increase of roughly 0.45 kg/m^3 (average crustal density of 3000 kg/m^3 multiplied with -15 $\times 10^{-5}$). This is reasonable, as the strain scales as |u|/wavelength (*Pollitz*, 1997). In the case of 10 ka loading with a 1111 km radius load, the deformation is dominant in the vertical and about 200 m. The wavelength of the load is twice the radius and therefore equal to 2222

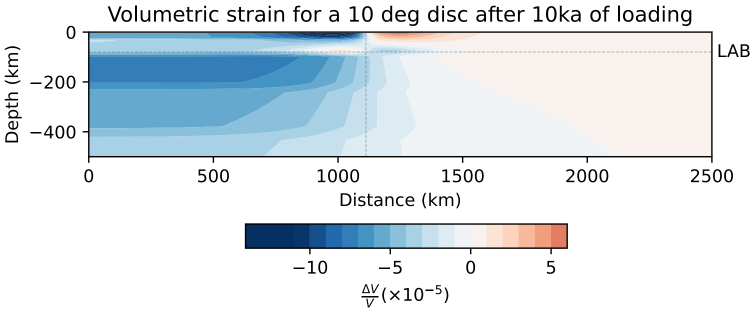

Figure 4.13: Volumetric strain after 10ka of loading with a 10 deg disc in the NG model. Positive values denote compression, and negative values dilatation. The Lithosphere-Asthenosphere Boundary (LAB) is denoted by the horizontal dashed line.

km. |u|/wavelength then roughly equals 200 m / 2222 km which is equal to just under 1×10^{-4}, similar in magnitude to what is found here for the volumetric strain.

The Lithosphere-Asthenosphere Boundary (LAB) exhibits a clear boundary for the volumetric strain of the elements, as just above this boundary values are positive, and below we find negative values again. This implies that material in the uppermost layer of the mantle compresses more than the lowest elemental layer in the crust. The most negative strain is found just below the surface, as anticipated.

5

THE EFFECT OF A 3D EARTH STRUCTURE ON HORIZONTAL GIA MOTION IN SOUTHEAST ALASKA

5.1. INTRODUCTION

Southeast Alaska is a tectonically complex region that experienced significant seismic activity over the past century, such as the M_w 7.9 Fairweather Earthquake in 1958 and the M_w 7 Queen Charlotte Earthquake in 1927 (e.g., *Doser and Lomas*, 2000). Its tectonic setting is best described by right-lateral strike-slip motion along the Fairweather and Queen Charlotte faults (Figure 5.1). These two faults accommodate most of the observed relative motion between the neighbouring Pacific and North America plates (*Mazzotti et al.*, 2003). To the west of the region, interpretations of the observed motions are complicated by the existence of the Yakutat terrane, which is proposed to be either an oceanic plateau that is thicker than normal oceanic crust but thinner than continental crust (*Christeson et al.*, 2010; *Worthington et al.*, 2012), or a mix of oceanic and continental crust (*Leonard et al.*, 2007).

Understanding the tectonic motion allows us to better explain the observed topography and seismic activity in Southeast Alaska. Global Navigation Satellite Systems (GNSS) measurements are performed in the area (e.g., *Elliott and Freymueller*, 2020; *Elliott et al.*, 2010; *Freymueller et al.*, 2008; *Larsen et al.*, 2005). These measurements show the integrated effect of all processes on the surface and subsurface, which makes it difficult to deduce plate motion. Nevertheless, several studies have attempted to infer plate velocities by dividing the tectonic region of Alaska in multiple blocks, and determine the

---

This chapter is written in the form of a draft article, and has been realised in collaboration with Dr. Julie Elliott from Michigan State University, Prof. Jeffrey Freymueller from Michigan State University, and Ir. Celine Marsman from Utrecht University.

location of the Euler pole and the associated angular velocity for each block. The geometry of those blocks is based on documented seismic and geologic evidence (*Elliott et al.*, 2010). The first study making use of a block model to study tectonics in Alaska is *Lahr and Plafker* (1980), who derived velocities for three distinct blocks relative to the North American plate. Examples of later studies are *Elliott et al.* (2010) for Southeast Alaska and *Elliott and Freymueller* (2020) for the whole of Alaska. These studies divided their study region in ten and seventeen blocks, respectively. This enabled them to obtain an integrated kinematic view of the tectonics in the area, and also provided constraints on the seismic activity in the region.

However, before tectonic motion can be distinguished, the Global Navigation Satellite Systems (GNSS) measurements need to be corrected for crustal movement due to Glacial Isostatic Adjustment (GIA) (e.g., *King et al.*, 2016; *Klemann et al.*, 2008; *Turner et al.*, 2020). This is especially relevant for Southeast Alaska, as it harbours the Glacier Bay region which experiences high uplift rates (up to 30 mm a^{-1}) and considerable horizontal motion (up to 7 mm a^{-1}) due to GIA (*Elliott et al.*, 2010; *Hu and Freymueller*, 2019; *Larsen et al.*, 2005). This horizontal motion is much larger than a typical uncertainty in GNSS derived horizontal velocity of 0.5 mm a^{-1}(e.g., *Vardić et al.*, 2022).

How well GIA is known in Southeast Alaska depends on the employed GIA model, and the accuracy of its predictions. The studies of *Elliott et al.* (2010) and *Elliott and Freymueller* (2020) have employed the self-gravitating spherical GIA model TABOO (*Spada*, 2003) to simulate GIA in Alaska. This model is incompressible, which is shown to introduce some error because the real Earth is compressible. The error introduced by this approximation is especially large for horizontal deformations (*James and Lambert* (1993); *Johnston et al.* (1997); *Mitrovica et al.* (1994b); *Reusen et al.* (2023); *Tanaka et al.* (2011), this thesis).

In addition, 3D structure is generally not included in GIA models that are used to correct GNSS velocities. For example, the GIA model utilised by *Elliott et al.* (2010) and *Elliott and Freymueller* (2020) allows only for a radially varying Earth structure, while horizontal motions are found to be especially sensitive to lateral Earth structure (e.g., *Gasperini et al.*, 1990; *Kaufmann et al.*, 2005; *Latychev et al.*, 2005; *O'Keefe and Wu*, 2002; *Steffen et al.*, 2006; *Vardić et al.*, 2022). In the following lines, I summarise a sample of these studies investigating the effect of 3D Earth structure on horizontal velocities. *Kaufmann et al.* (2005) find that horizontal motion in Antarctica is directed from stiffer East Antarctica to weaker West Antarctica when implementing a 3D Earth structure. *Steffen et al.* (2006) study horizontal motion due to GIA in Fennoscandia, and find that the typical divergent motion acquired using 1D Earth models is no longer present in 3D GIA models. Finally, *Latychev et al.* (2005) investigate GIA in North America, and conclude that lateral variations weaken the outward directed horizontal motions in the near field which was found by 1D models.

Regional and global tomography studies show that lateral variations in seismic velocities are present in Alaska (e.g., *Jiang et al.*, 2018; *Porritt et al.*, 2021; *Schaeffer and Lebedev*, 2013). These seismic velocity variations translate to lateral variations in viscosity under the assumption that the seismic velocity anomalies are mainly caused by variations in temperature. Alaska's complex tectonic setting, exhibited by the numerous faults in Fig-

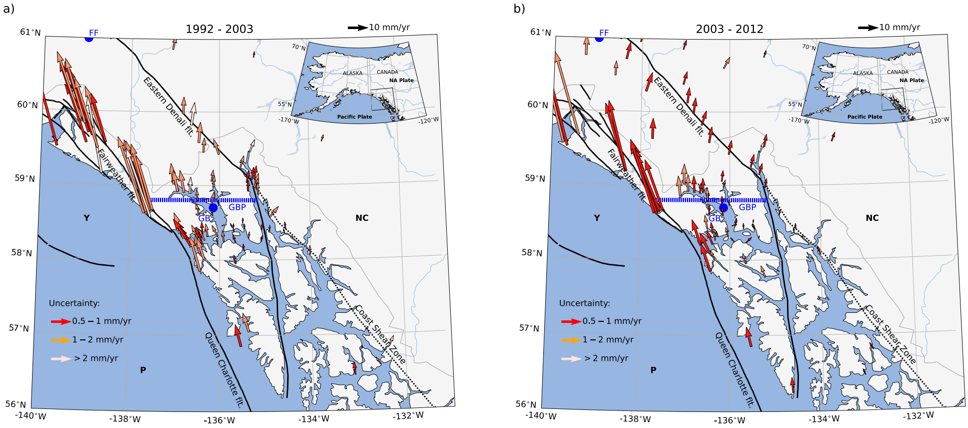

Figure 5.1: Observed horizontal motions in Southeast Alaska as determined by *Hu and Freymueller* (2019) for the periods 1992-2003 and 2003-2012. Abbreviations are P = Pacific plate, Y = Yukatat block, NC = Northern Cordillera, GBP = Glacier Bay Partition, GB = Glacier Bay, FF = Far Field, NA plate = North American Plate. The faults shown are from the Alaska Quaternary Fault and Folds database (*Koehler et al.*, 2012). The postulated fault of the coast shear zone is exhibited by a black dashed line. The dashed blue line denotes the Glacier Bay Partition as proposed by *Elliott et al.* (2010).

ure 5.1, further corroborates the idea that lateral variations in Earth's structure exist in this region. *Marsman et al.* (2021) found that 3D variations in Alaska do not significantly influence the vertical, but this might be different for horizontal motion which is found to be very sensitive to lateral Earth structure variations (e.g., *Gasperini et al.*, 1990; *Kaufmann et al.*, 2005; *Latychev et al.*, 2005; *O'Keefe and Wu*, 2002; *Steffen et al.*, 2006). In this study, I adapt the recently developed compressible Cartesian Finite Element model of *Reusen et al.* (2023), this thesis, for the region of Southeast Alaska. This compressible non self-gravitating Cartesian model can simulate the horizontal deformation of small loads (<200 km in radius) more accurately than incompressible self-gravitating spherical models (*Reusen et al.* (2023), this thesis). Moreover, it can incorporate 3D variations in Earth structure.

Following the arguments given in the previous paragraph, it is likely that lateral viscosity variations exist in Southeast Alaska. I start by investigating the effect of a schematic viscosity contrast in order to fundamentally understand the effect of lateral Earth structure variations on the horizontal GIA motions in Southeast Alaska. The findings of this schematic study help us understand the horizontal GIA deformation in Southeast Alaska due to more realistic 3D Earth structures. Last, I test the effect of 3D GIA on horizontal motion using a selection of the more realistic 3D Earth structures.

I aim to answer the following research questions:

1. What impact does a schematic contrast of the asthenosphere viscosity and lithosphere thickness in a GIA model have on the modelled horizontal motions in Southeast Alaska?
2. How sensitive are the modelled horizontal motions to realistic lateral variations in

the Earth's structure?

3. How important is the inclusion of 3D Earth structure in a GIA model that is used for tectonic block motion estimates of Southeast Alaska?

Observed horizontal motion should be corrected for GIA to obtain tectonically driven motion. If the observed motion is corrected by a GIA model that is too simplified, some GIA signal might be left or introduced in our corrected velocities. This leads to errors in the inferred tectonic motion. By exploring the sensitivity of horizontal motion in Southeast Alaska to 3D GIA, the importance of 3D GIA for inferring tectonic motion in Southeast Alaska is investigated. Therefore, the study connects the fields of GIA research with research on tectonics. Constraints from tectonic studies may even yield information on the lateral variability in the Earth, provided that the tectonic motion is found to be sensitive to the 3D GIA model correction.

The chapter is structured as follows. In Section 5.2, I describe the GPS data used. After, I explain the methodology, with Section 5.2.2 describing the GIA model utilised, Section 5.2.4 the ice model, and Section 5.2.3 the setup for the Earth model, focusing on the configuration of the lateral variations in the viscosity. Section 5.2.5 explains the reasoning behind the selected locations, and Section 5.2.6 describes the setup of the block models. Section 5.3 describes the results, starting with the sensitivity analysis to address research question 1 and after that focusing on the more realistic 3D models. In Section 5.4 I provide a discussion, and in Section 5.5 formulate the conclusions.

5.2. DATA AND METHODS

5.2.1. GPS DATA

The horizontal GPS data employed in this study is the set from *Hu and Freymueller* (2019) for the periods 1992-2003 and 2003-2012. Two different periods are selected since the uplift differs markedly before and after 2003 as observed by continuous sites and by campaign sites with many repeated surveys (*Hu and Freymueller*, 2019). Observations after 2012 are not used because interpreting these motions is complicated by the 2012 Haida Gwaii and 2013 Craig earthquakes (*Aiken et al.*, 2015; *Ding et al.*, 2015; *Lay et al.*, 2013). The data before 2003 have a larger uncertainty (Figure 5.1), but nevertheless aid in understanding the tectonic setting. The 1992-2003 period contains 136 GPS points, while the 2003-2012 period consists of only 89 GPS points because less campaign sites were employed in the later period. The GIA model results are averaged only over the period 2003-2012, and I acknowledge that this slightly biases tectonic model findings of Section 5.3.3, which also use data before 2003.

The largest motions are found near the Fairweather fault, with values of up to 50 mm/yr (Figure 5.1). Further inland, the horizontal velocities are mostly less than 10 mm/yr indicating that most of the relative motion is indeed accommodated by the Fairweather and Queen Charlotte faults (*Mazzotti et al.*, 2003). Horizontal motions near the coast are directed to the Northwest, but rotate clockwise further inland (*Elliott et al.*, 2010).

5.2.2. MODEL SETUP

The GIA simulations are performed with the non self-gravitating compressible Cartesian model of *Reusen et al.* (2023), this thesis, which uses the Finite Element (FE) software Abaqus (*Hibbitt et al.*, 2016). The model includes gravity, and solves the governing FE equations using a stiffness matrix that depends on prior deformation (*Hampel et al.* (2019); *Reusen et al.* (2023), this thesis). This is different from most earlier GIA studies performed with FE software Abaqus which use elastic foundations at layer boundaries to include buoyancy forces (e.g., *Kaufmann et al.*, 2005; *Marsman et al.*, 2021; *Nield et al.*, 2018). The models employing elastic foundations to simulate the buoyancy forces cannot be made compressible (*Bängtsson and Lund*, 2008). Therefore I opt to use the method described in *Hampel et al.* (2019) for which the compressible version provides a minor improvement in simulated horizontal deformation caused by small ice sheets (*Reusen et al.* (2023), this thesis).

Wong and Wu (2019) describe a solution to include compressibility in GIA models which is more complicated than with the previously mentioned models. It is adapted by *Huang et al.* (2023) so that it is now applicable to more realistic loading scenarios. However, these models can not yet be run with the same resolution as the compressible Cartesian model utilised in this study.

This study employs a Cartesian model due to its short computation time as compared to that of spherical models, allowing us to simulate small regions like Southeast Alaska with high resolution (15 km by 15 km). The model is applicable for simulating horizontal deformation due to small ice sheets (<200 km in radius) (*Reusen et al.* (2023), this thesis), so I briefly compare this ice sheet area to the area covered by glaciers in Alaska. The glaciers in Alaska are estimated to cover 86,715 km^2 (*Pfeffer et al.*, 2014), which is less than the area covered by a hypothetical circular disc of 200 km in radius that covers just over 125,000 km^2. Therefore, I also deem Alaska to be suitable for modelling using cartesian models.

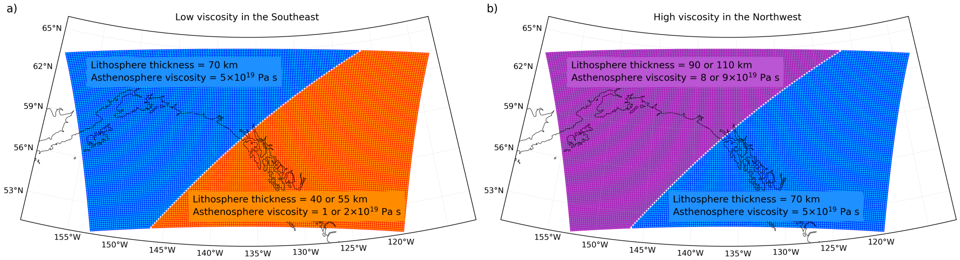

Figure 5.2: Top layer mesh projected over Alaska for a) the 3D Earth model where the lithospheric thickness and viscosity are lowered in Southeast Alaska with respect to the 1D reference, and b) the 3D Earth model where the lithospheric thickness and viscosity are increased in the Northwest.

The model geometry is very similar to that of *Marsman et al.* (2021), which is based on *Schotman et al.* (2008) and *Barnhoorn et al.* (2011). The mesh consists of a finely meshed region surrounded by a coarser region. The finely meshed region has a resolution of 15

× 15 km in the upper 90 km, and 75 × 75 km for elements below 90 km depth (Figure 2 in *Marsman et al.*, 2021). The total model width is 20,000 × 20,000 km to minimize possible boundary effects. The only geometrical difference between our model and that of *Marsman et al.* (2021) is in the vertical direction. A depth of 10,000 km is used by *Marsman et al.* (2021), whereas our model extends to 2,891 km depth (i.e., until the core-mantle boundary). The top layer of the mesh in the finely meshed region is exhibited in Figure 5.2. I validate the model to that of *Marsman et al.* (2021) in Appendix A of this chapter (Figure 5.10). Differences in simulated uplift rates are less than 0.2 mm/yr everywhere in the model domain.

5.2.3. EARTH MODELS

EARTH MODEL FOR SENSITIVITY TESTS

I start by explaining the Earth model used for the sensitivity tests. With these sensitivity tests we investigate how much a 3D Earth structure changes the GIA model output in Glacier Bay and the surrounding area.

For the sensitivity tests I have divided the model domain in two regions divided by a sharp boundary that runs through the Glacier Bay ice field. The orientation of the boundary is based on the gradient in the shear wave velocity anomalies of seismic models SL2013sv and SAVANI-US. Shear wave velocities of SL2013sv are lowest in the Southeast of the model domain (Figure 5.3a). I assume that temperature variations are the main cause of shear wave velocity anomalies. A negative shear wave velocity anomalies is related to a higher temperature, which in turn translates to a lower viscosity. The viscosity in the Southeast is hence expected to be lower than in the Northwest. In addition, the lithospheric thickness in the Southeast is also expected to be smaller than average (*Fullea et al.*, 2021).

To investigate the sensitivity to the lateral variations in the Earth model, I need a reference model that is representative for the area. The lithosphere thickness estimates are 42-85 km for Alaska, with a low viscosity asthenosphere ($1.5 \times 10^{18} - 7 \times 10^{19}$ Pa s) below the elastic lithosphere (*Elliott et al.*, 2010; *Hu and Freymueller*, 2019; *Larsen et al.*, 2005; *Marsman et al.*, 2021; *Sato et al.*, 2011). I therefore opt for a 70 km thick lithosphere in the reference model, with an asthenosphere thickness of 230 km and an asthenosphere viscosity of 5×10^{19} Pa s. The layers and viscosity of the reference model are shown in Table 5.1. The density, Young's modulus and Poisson's ratio are taken from Table 2 of *Marsman et al.* (2021), which uses the same layering.

The mesh of the model, containing the two model domains, is illustrated in Figure 5.2. I change the lithosphere thickness and viscosity only in one of the model domains, and assign the values of the reference model to the other half. The range in abovementioned estimates of the lithosphere thickness and asthenosphere viscosity determines the magnitude of the lateral variations that I implement. For the Southeast region, this means that I set the lithosphere thickness to 40, 55 or 70 km, and the asthenosphere viscosity to 1, 2 or 5 $\times 10^{19}$ Pa s. In the Northwest of the domain, the Earth model is assigned a lithosphere thickness 70, 90 or 110 km, and an asthenosphere viscosity of 5, 8 or 9 $\times 10^{19}$

Pa s. I focus only on viscosities on the order of 10^{19} Pa s as these higher range of values are found by the more recent studies of *Hu and Freymueller* (2019) and *Marsman et al.* (2021). Moreover, I am limited in the choice of lithosphere thickness by the layering in the model, and therefore have to employ a lithosphere thickness of 110 km. This is larger than found by earlier studies, and might slightly exaggerate the effect of the lithospheric thickness.

	Layer	From (km)	To (km)	Viscosity (Pa s)
Lithosphere	1	0	12	–
	2	12	26	–
	3	26	40	–
	4	40	55	–
	5	55	70	–
Asthenosphere	6	70	90	5×10^{19}
	7	90	110	5×10^{19}
	8	110	130	5×10^{19}
	9	130	150	5×10^{19}
	10	150	170	5×10^{19}
	11	170	190	5×10^{19}
	12	190	210	5×10^{19}
	13	210	230	5×10^{19}
	14	230	250	5×10^{19}
	15	250	290	5×10^{19}
UM	16	290	340	5×10^{20}
	17	340	400	5×10^{20}
	18	400	535	5×10^{20}
	19	535	670	5×10^{20}
LM	20	670	920	1.6×10^{21}
	21	920	1170	1.6×10^{21}
	22	1170	1600	3.2×10^{21}
	23	1600	2030	3.2×10^{21}
	24	2030	2460	3.2×10^{21}
	25	2460	2891	3.2×10^{21}

Table 5.1: The viscosity and gravity in each layer of our reference model. UM = upper mantle, LM = lower mantle. The viscosity below the asthenosphere in the upper and lower mantle is from VM5a (*Peltier et al.*, 2015), and the gravity is calculated from the densities.

REALISTIC 3D EARTH MODELS

Several 3D GIA studies derive a viscosity perturbation from seismic shear wave velocity anomalies through the assumption that these seismic anomalies are caused by temperature variations which are directly related to the viscosity (e.g., *Latychev et al.*, 2005; *Li et al.*, 2018; *Steffen et al.*, 2006). Other studies have used flow laws to convert absolute temperatures to viscosity (e.g., *Blank et al.*, 2021; *van der Wal et al.*, 2013, 2015). I will implement both techniques, as there is no agreement on the accuracy of either technique (*Ivins et al.*, 2023), and the modelled horizontal motions of GIA are very sensitive to lateral variations in the Earth structure (e.g., *Gasperini et al.*, 1990; *Latychev et al.*, 2005; *Steffen et al.*, 2006). Utilising more 3D models helps us to better capture the scatter in the GIA signal. I elaborate on how the 3D Earth structures are derived from shear wave anomalies and temperatures in Section 5.2.3 and 5.2.3, respectively.

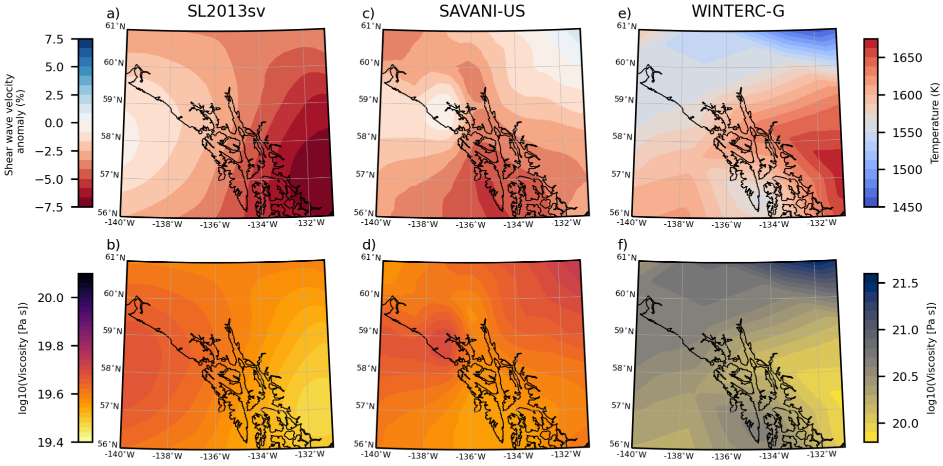

Figure 5.3: subplot a), c), and e) show the input from which the viscosities in b), d) and f) are determined. b) is the viscosity profile that is derived from shear wave velocity anomalies for SL2013SV in a). Similarly, d) shows the viscosity profile that is determined from shear wave velocity anomalies of SAVANI-US in c). f) exhibits the viscosity profile that is converted from the WINTERC-G temperatures of e). The parameters used to convert the seismic anomalies to viscosities are a background viscosity of 5×10^{19} Pa s and $\beta = 0.1$. The WINTERC-G temperatures are converted to viscosity using a grain size of 8 mm combined with a water content of 400 ppm. All parameter values are taken from *Marsman et al.* (2021) for the best fit model of each respective method. The values are shown at a depth of 80 km.

The first set of 37 realistic 3D Earth structures in this study is based on shear wave velocity anomalies of seismic model SL2013sv (*Schaeffer and Lebedev*, 2013), and another 37 are derived from shear wave velocity anomalies in SAVANI-US (*Porritt et al.*, 2021). The sets are constructed by varying parameters for the background viscosity and for β, which denotes the fraction of the seismic velocity anomaly that is related to temperature anomalies (*Wu et al.*, 2013). The β parameter is explained in more detail in Section 5.2.3. The third set contains 31 realisations from absolute temperatures determined by lithosphere and upper mantle model WINTERC-G (*Fullea et al.*, 2021). WINTERC-G is a thermochemical model of the lithosphere and upper mantle constrained by inverting seismic waveform data together with data on heat flow, surface elevation, and satellite gravity (*Fullea et al.*, 2021). WINTERC-G provides temperatures up to a depth of 400 km. By assuming that the main constituent of the mantle is olivine, these temperatures can be translated to viscosities using the flow law from *Hirth and Kohlstedt* (2003). In this flow law, the water content and the grain size can be varied to generate different viscosity profiles. With in total 105 model runs, I exhibit the scatter in the GIA signal due to lateral variations in the structure of the Earth. A selection of the realistic 3D Earth models is applied as correction on the observed GNSS velocities to arrive at the tectonic block models of *Elliott et al.* (2010) and *Elliott and Freymueller* (2020), and investigate the effect of 3D GIA models on the tectonics in the area.

3D EARTH MODELS FROM SHEAR WAVE VELOCITY ANOMALIES

This method derives lateral variations in the Earth model from shear wave velocity anomalies of seismic models SL2013sv (*Schaeffer and Lebedev*, 2013) and SAVANI-US (*Porritt et al.*, 2021). SAVANI-US is an extension of SAVANI (*Auer et al.*, 2014) with increased data density over continental United States (US) using body wave phases from the USArray Array Network Facility and *Lai et al.* (2019), together with ambient noise tomography from *Ekström* (2017).

The seismic shear wave velocity anomalies are predominantly negative in the study domain (Figure 5.3). This is in agreement with regional shear wave velocity studies, who also found negative anomalies in the Glacier Bay area (*Jiang et al.*, 2018; *Mercier et al.*, 2009). Negative shear wave velocity anomalies correspond to higher temperatures and to viscosities that are lower than the background viscosity. In general the seismic shear wave velocities of SL2013sv and SAVANI-US agree, but SL2013sv has a more distinct trend of increasingly negative anomalies from the Northwest of the domain to the Southeast (Figures 5.3a, c). Moreover, the maximum shear wave velocity anomalies are mostly below 6% in SAVANI-US, while velocity anomalies can be up to 7.5% for SL2013sv.

A scaling between seismic velocity anomalies and Newtonian viscosity anomalies is presented by *Ivins and Sammis* (1995). This relationship assumes a thermal contribution to the shear wave velocity anomalies. As a fraction of the seismic velocity anomaly can also be related to chemical composition rather than temperature, *Wu et al.* (2013) introduced the β parameter ($\beta \, \epsilon$ [0,1]). A value close to 0 implies that the shear wave velocity anomalies are due to composition and not temperature, and a value of 1 means that all of the shear wave velocity anomalies are explained by temperature. The formula for the scaling relationship is as follows:

$$log_{10}(\Delta\eta) = \frac{-log_{10}(e)\,\beta}{[\partial ln v_s/\partial T]_{tot}} \frac{E+PV}{RT_0^2} \frac{\partial v_s}{v_{s,0}}. \tag{5.1}$$

Here, $\Delta\eta$ is the viscosity anomaly, e is Euler's number, $[\partial ln v_s/\partial T]_{tot}$ is the derivative of the shear wave velocity, v_s, with respect to the temperature, thereby acounting for both anelastic and anharmonic effects. Values of this derivative are taken from Table 20.2 in *Karato* (2008). E is the activation energy, P the pressure, V the activation volume, R the gas constant, T_0 the background temperature profile, and $\frac{\partial v_s}{v_{s,0}}$ the shear wave velocity perturbation with respect to the reference seismic velocity that is provided by seismic models.

The effective viscosity is calculated as $log_{10}(\eta_{eff}) = log_{10}(\eta_0) + log_{10}(\Delta\eta)$, where η_0 is the background viscosity. I consider η_0 and β as unknown parameters that capture most uncertainty in addition to the uncertainty from the seismic velocities. By varying η_0 or β I can generate different viscosity profiles. *Marsman et al.* (2021) ran several realistic 3D GIA models, and inferred the parameters that best fit the GNSS uplift rate data. Based on findings in their study, I vary η_0 between 3×10^{19} Pa s and 10×10^{19} Pa s. Figure 5.3b and d display the resulting viscosity profile at 80 km depth for the best fit model parameters, which are a background viscosity of 5×10^{19} Pa s and a β value of 0.1 (*Marsman et al.*, 2021). In this scenario, shear wave velocity anomalies are for a large part explained by compositional changes. Usually, the seismic velocity anomalies are mostly determined by upper mantle temperature, with compositional effects being of lesser importance (*Cammarano et al.*, 2003; *Goes et al.*, 2000). However, Southeast Alaska has a long geologic history of subduction, and it is therefore probable that the mantle is significantly hydrated (*Dixon et al.*, 2004).

In Abaqus one can use a flow law with an equation for the uniaxial equivalent of strain increments, $\Delta\tilde{\epsilon}$, (*Blank et al.*, 2021):

$$\Delta\tilde{\epsilon} = B_{diff}\tilde{q}^n \Delta t. \tag{5.2}$$

Here, n is the stress exponent and Δt are the time increments. I consider diffusion creep, for which the stress exponent is 1 implying a linear relation between stress and strain. The diffusion creep parameter B_{diff} is calculated from the effective viscosity η_{eff} using the following relationship:

$$B_{\text{diff}} = \frac{1}{3\eta_{\text{eff}}}. \tag{5.3}$$

Here, η_{eff} is calculated using Equation 5.1. The only remaining unknown in Equation 5.2 is $\tilde{q}$, which is the Von Mises stress, calculated as

$$\tilde{q} = \sqrt{\frac{3}{2} q_{ij} q_{ij}}, \tag{5.4}$$

where q_{ij} are the components of the deviatoric stress tensor, and are calculated by Abaqus during runtime.

3D EARTH MODELS FROM ABSOLUTE TEMPERATURES

Next, I explain the method to calculate the viscosity from WINTERC-G temperatures (*Fullea et al.*, 2021). WINTERC-G provides temperature fields up to a depth of 400 km, and a slice of these temperatures is exhibited at a depth of 80 km in Figure 5.3e. The spatial temperature pattern bears some resemblance to the shear wave anomalies of SL2013sv and SAVANI-US, with higher temperatures in the Southeast of the domain and lower temperatures in the Northwest. In the first approach, lateral viscosity variations are imposed on a background viscosity. In the approach described here, there is no such constraint, and some of the resulting viscosity maps/profiles give more unrealistic GIA predictions.

For the conversion from temperature to viscosity, I assume that the mantle is composed mainly of olivine and examine variations in water content and grain size. I did not consider the effect of background stress as the magnitude and direction are hard to quantify. The flow law for olivine is described in *Hirth and Kohlstedt* (2003):

$$\dot{\epsilon} = A\sigma^n d^{-p} fH_2O^r exp\left(-\frac{E+PV}{RT}\right). \tag{5.5}$$

Here, $\dot{\epsilon}$ is the strain rate, A is a constant, σ is the differential stress, d is the grain size, and fH_2O is the water content in ppm H_2O. n, p, r are the exponents for the stress, grain size, and water content, respectively. Finally, E is the activation energy, P the pressure, V the activation volume, R the gas constant and T the absolute temperature. In Equation 5.5, I have assumed that there is no melt. The values for A, E, and V, r, n, and p are taken from *Hirth and Kohlstedt* (2003) and are listed in Table 5.2.

A	E (kJ/mol)	V (10^{-6} m^3/mol)	r	n	p
3.33×10^5	335	4	1	1	3

Table 5.2: Rheological parameters for calculation of the diffusion creep when using the flow law of *Hirth and Kohlstedt* (2003). These parameters are the same as in Table S3 of *Marsman et al.* (2021).

The strain increments in Abaqus are still computed using Equation 5.2. I only consider diffusion creep, for which the relationship between stress and strain is linear. I could in principle also include dislocation creep, which considers a nonlinear relationship between stress and strain, but the stress in the mantle is not well known and it is therefore difficult to infer the exact importance of dislocation creep. Alaska has a complex tectonic setting, and large tectonic stresses might be present. If large tectonic background stresses are indeed present, then the stress changes of GIA are small compared to the background stress. The stress changes are in that case not as important (*van der Wal et al.*, 2013). I therefore consider a linear relation between stress and strain (*Schmidt et al.*, 2012b). The diffusion creep, B_{diff}, is calculated as

$$B_{diff} = Ad^{-p} fH_2O^r exp\left(-\frac{E+PV}{RT}\right). \tag{5.6}$$

For comparing with the first approach, I calculate the effective viscosity using $\eta_{eff} = 1/3B_{diff}$.

Figure 5.3f exhibits the viscosity converted from the temperature using the best fit parameters of *Marsman et al.* (2021) for the WINTERC-G model, which are a grain size of 8 mm and a water content of 400 ppm. However, the absolute value of the temperature is too low, resulting in viscosities of WINTERC-G that are at least an order of magnitude larger at 80 km depth compared to models generated from SL2013sv and SAVANI-US. This was also found by *Marsman et al.* (2021), and points to a lithosphere that is too thick in the WINTERC-G models. At 140 km depth, the viscosity of all models are the same order of magnitude again (Figure 5.11). There might be better agreement between viscosities generated from WINTERC-G and those resulting from seismic anomalies if dislocation creep is included when calculating the effective viscosity, but further research is needed to investigate this.

5.2.4. ICE MODEL

The regional ice model for Alaska is constructed by *Hu and Freymueller* (2019), and it includes cycles of ice growth and decay during the Little Ice Age (LIA), as well as the ice evolution during several centuries leading up to the LIA. It spans from 0 AD until 2012 AD, and consists of a regional model for Alaska and of models specific for Glacier Bay and Yakutat. The latter two regions are separate from the regional model, as Glacier Bay experienced significant ice loss since the LIA (*Larsen et al.*, 2004), while the Yakutat Ice field has been subject to substantial thinning between 2000 and 2010 (*Trüssel et al.*, 2013).

The time evolution of all three regions is exhibited in Figure 5 of *Hu and Freymueller* (2019), and is briefly summarised here. In the early centuries, between 0 AD and 300 AD, hardly any ice is present in the regional model because of the absence of observations as the advance of the LIA wiped out any evidence on Holocene glaciations before 300 AD (*Larsen et al.*, 2004). The glaciation cycle from 300 AD to 900 AD is crudely approximated, and the LIA is simulated using three cycles of ice growth and decay between roughly 1200 AD and 1900 AD (*Wiles et al.*, 1999).

The evolution of the Yakutat ice field follows that of the regional model, but unpublished laser altimetry data found that this region experiences ice loss roughly three times as fast as in the regional model (*Larsen et al.*, 2004). The model for Glacier Bay estimates a constant ice height starting at 0 AD until 1500 AD, until ice in the lower part of Glacier Bay extended between 1500 AD and 1650 AD (*Goodwin*, 1988; *Monteith et al.*, 2004). The decay of ice at the end of the LIA starts after 1770 AD, and follows observations of temperate tidewater glacier retreats (*Larsen et al.*, 2005).

The ice model of *Hu and Freymueller* (2019) differs from that used by *Larsen et al.* (2005) from the twentieth century onwards, for which the ice history has been based on the ice rates as determined by *Berthier et al.* (2010). *Berthier et al.* (2010) calculated an ice loss rate using observations that are performed between 1962 and 2006, and I assume their inferred ice loss rate for the period 1900-1995. The ice loss rates for the recent periods 1995-2003 and 2003-2012 are then extrapolated and multiplied by 1.8 and 2.2, respectively. All ice heights are given as discs with a uniform thickness, which are interpolated to a rectangular FE grid by *Marsman et al.* (2021).

I do not model the ice decay over the Last Glacial Maximum (LGM) such as the deglaciation of the Laurentide ice sheet, and assume isostatic equilibrium as the starting point for the simulations. As the asthenosphere viscosities are low below Alaska ($\sim 10^{19}$ Pa s), the Earth responds to ice load variations on time scales of years to decades, and I expect the effect of LGM ice melt to be small. The tectonic model studies of *Elliott et al.* (2010) and *Elliott and Freymueller* (2020) did not include the LGM deglaciation either, based on the conclusion that the LGM ice melt does not have a significant impact on the uplift in Alaska (*Larsen et al.*, 2005). Nevertheless, *Sella et al.* (2007) show a great variation in modelled horizontal GIA from the melting of the Laurentide ice sheet, with horizontal velocities of ~ 1 mm a^{-1} in Southeast Alaska either pointing away or towards the former Laurentide ice sheet depending on the underlying viscosity. However, its exact contribution is very difficult to quantify as exhibited by the large scatter in the results of *Sella et al.* (2007), and I therefore do not include this contribution in this study.

5.2.5. SELECTED LOCATIONS

The observed velocities need to be corrected for the effect of GIA before they can be used in tectonic block model studies. The observed velocities close to Glacier Bay are directed North while observed velocities at a distance of about 300 km from Glacier Bay are directed more Northeast (Figure 5.1). I need these velocities to be more similar in order to place them on a single tectonic block. Previous tectonic block model studies corrected these observed velocities for the effect of GIA, but found that this correction does not make the velocities more similar (*Elliott and Freymueller*, 2020; *Elliott et al.*, 2010). I investigate if a 3D GIA model would be able to do so.

I have chosen two locations at which I exhibit the modelled horizontal motion due to GIA (Figure 5.1). The first location is in Glacier Bay (GB), close to the proposed fault of *Elliott et al.* (2010) and *Elliott and Freymueller* (2020). This is our near field location due to its proximity to the Glacier Bay ice fields. I also select a location in the Far Field (FF), as the horizontal motions due to GIA are still roughly 2 mm a^{-1} at a distance of 400 km even for a small ice sheet of just 200 km in radius (*Reusen et al.* (2023), this thesis). The chosen far field location is at the edge of our study domain (Figure 5.1). It is located in the region where observed horizontal motions are more directed Northeast rather than North as in the Glacier Bay area.

5.2.6. BLOCK MODEL SETUP

To answer research question 3, I apply 3D GIA model output as correction to the observed GNSS velocities, and forward the corrected velocities to existing tectonic block models from *Elliott et al.* (2010) and *Elliott and Freymueller* (2020). I forward multiple GIA simulations to sample the scatter caused by variations in the 3D structure. I investigate if the estimated tectonic velocities are affected by the GIA model correction and if this could change the interpretation of tectonics in the area.

Four different tectonic block models have been combined with the GIA simulations. The first block model is the block model for Southeast Alaska from *Elliott et al.* (2010) with the

Glacier Bay Partition (GBP), and the second uses the same block model but without the GBP. These models consist of 10 and 9 blocks, respectively. The third and fourth block models are from *Elliott and Freymueller* (2020) which are for the whole of Alaska, again with and without the GBP. They include 17 and 16 blocks, respectively.

The model from *Elliott et al.* (2010) is designed specifically for Southeast Alaska, while the model from *Elliott and Freymueller* (2020) is applicable for the whole of Alaska and Western Canada. The study of *Elliott and Freymueller* (2020) uses an updated GPS data set, a different version of the North American reference frame, and a Yakutat block which contains part at the surface and a flat subducting slab, as opposed to only the surface extension in the model of *Elliott et al.* (2010). By utilising block models from two different studies, I capture the scatter caused by choices in the block model, which we can compare to the effect of a GIA model with 3D Earth structure.

These block models have been tested with output of two GIA model runs from the group of best fitting models in *Marsman et al.* (2021), as these were the models that we had available at the time of performing this part of the research. All results using the block models have therefore been generated using the selected GIA models of *Marsman et al.* (2021), instead of the newly developed GIA models that are introduced earlier in this study. Of the selected GIA models, one run does not contain lateral variations, and a second run contains maximum lateral variations, in order to isolate the effect of 3D Earth structure. The 1D GIA run has parameter values $\beta = 0.0$ (all velocity anomalies are explained by compositional changes) and $\nu = 3.7 \times 10^{19}$ Pa s, while the 3D GIA run contains $\beta = 0.2$ and $\nu = 7 \times 10^{19}$ Pa s. I compare block model velocities generated using these new GIA runs with the block velocities of the original 2010 and 2020 studies.

The methodology to answer research question 3 is as follows. First, I subtract the GIA model output from the GNSS observations. The corrected velocities are then used in the block models to estimate new block velocities, while the geometry of the block models is unchanged with respect to their respective studies. These steps have been performed by Dr. Julie Elliot, Ohio State University.

5.3. RESULTS

5.3.1. SENSITIVITY STUDY

Figure 5.4 shows the horizontal deformation for the 1D reference model, and also for two 3D models where the viscosity has been changed in the Southeast and in the Northwest. Horizontal velocities in the 1D model are maximum close to the former ice edge and at most 4.2 mm a^{-1}, a bit less than the maximum modelled horizontal deformation rates of 5-7 mm a^{-1} (*Elliott et al.*, 2010; *Larsen et al.*, 2005), which uses a thinner lithosphere, a thicker asthenosphere and a lower asthenosphere viscosity. In the far field, horizontal velocities slowly decrease in magnitude with increasing distance to the ice load.

The 3D model with a lower viscosity and lithosphere thickness in the Southeast produces significantly larger velocities of at most 9.3 mm a^{-1}, and also a pattern that is greatly altered spatially with respect to the 1D reference run (Figure 5.4b). For the 3D model with a higher viscosity and lithosphere thickness in the Northwest, the simulated horizontal motions in the vicinity of Glacier Bay are smaller than those of the 1D reference run, and are at most 3.3 mm/yr (Figure 5.4c).

The last column of Figure 5.4 shows the difference between the 1D and 3D model runs. A model with a lower asthenosphere viscosity and a lower lithosphere thickness employed in the Southeast area leads to differences in horizontal velocities that mostly point from the Southeast to the Northwest. The net effect of the 3D Earth structure is thus a flow from the low viscosity area to the high viscosity area, in contrast to findings by *Kaufmann et al.* (2005), who model horizontal velocities directed from stiffer East Antarctica to the weaker West Antarctica. The net effect in the 3D run with lateral changes in the Northwest is a flow towards Glacier Bay (Figure 5.4e), as a result of the smaller outward velocities in that area. A 3D Earth structure can thereby control the direction and the magnitude of the resulting GIA signal.

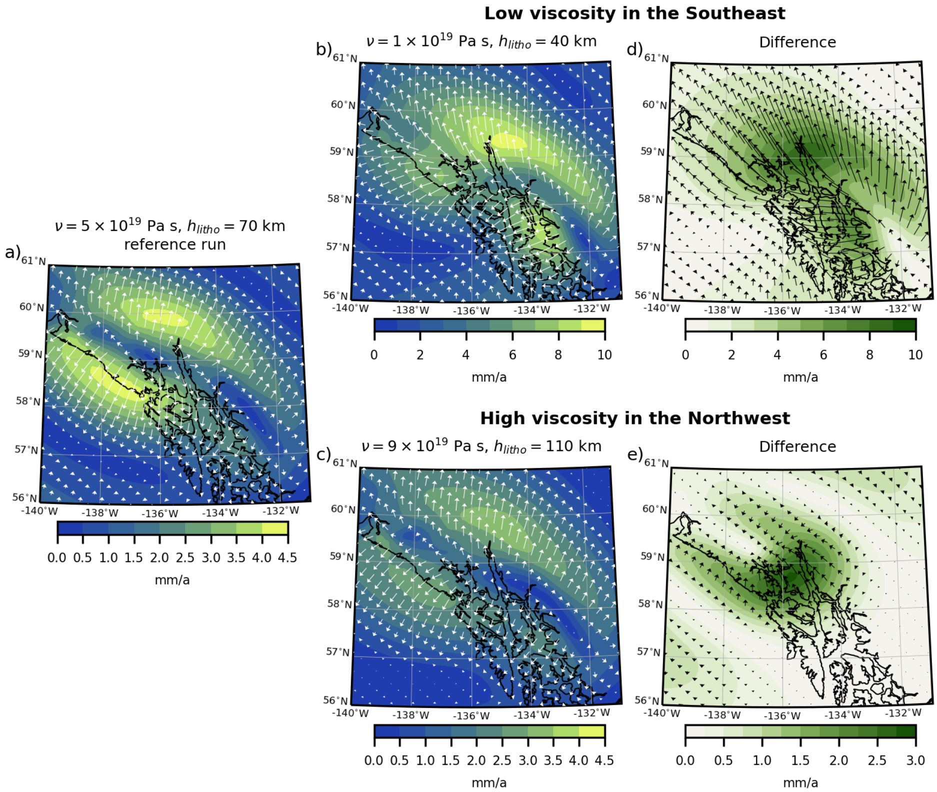

Figure 5.4: Modelled horizontal velocities in Southeast Alaska for a) the reference 1D GIA model, b) the 3D GIA model with low viscosities in the Southeast, and c) the 3D GIA model with high viscosities in the Northwest of the domain. The color fill shows the magnitude of the horizontal velocities. Subplots d) and e) exhibit the differences of the respective 3D GIA models with the 1D GIA reference model. Note that the colorbar range is larger in subplots b) and d) than in the other subplots.

The observed velocities in Southeast Alaska are directed North close to Glacier Bay, but Northeast further away at a distance of roughly 300 km from Glacier Bay (Figure 5.1). Because of this, these velocities are placed on two different tectonic blocks (*Elliott and Freymueller*, 2020; *Elliott et al.*, 2010). A 3D GIA model could in theory make these velocities more similar, thereby allowing the use of only a single tectonic block. For this reason, I interpolate the velocities at Glacier Bay (GB) and also at a location in the Far Field (FF). The exact position of these locations is exhibited in Figure 5.1.

Figure 5.5 exhibits these interpolated velocities. In the 1D reference model, the flow is directed southward at GB and just less than 2.5 mm a^{-1} (top right arrow of Figure 5.5a and b). The horizontal velocity in the FF is pointing Northeast in the 1D reference model and is only 2.1 mm a^{-1} in magnitude.

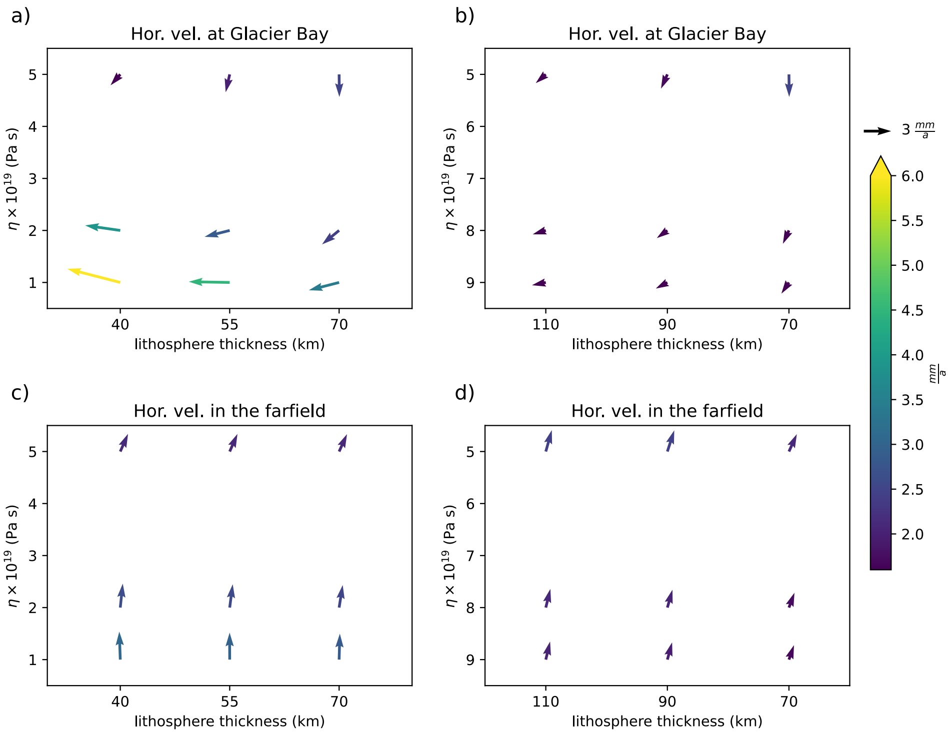

Figure 5.5: Modelled horizontal velocities interpolated at Glacier Bay (a,b), and at the far field location (c,d) as depicted by Figure 5.1. Subplots a) and c) exhibit the horizontal velocities when lateral variations are implemented in the Southeast of the domain, and subplots b) and d) show the horizontal velocities for variations in the Northwest of the domain. The x and y axis denote the lithosphere thickness and asthenosphere viscosity in the respective area of the domain. The axes of b) and d) are inverted so that all subplots show the reference model in the top right, and the most dramatic changes are shown in the bottom left.

The horizontal velocity at GB becomes more westward-directed for increasing lateral variations in 3D Earth structure, from the low viscosity area in the Southeast to the region with higher viscosity in the Northwest, in agreement with earlier findings in this chapter. The magnitude of the horizontal motions is only increased if a lower viscosity is imposed in the Southeast, and not when the lithosphere thickness or asthenosphere are increased in the Northwest. For the 3D model runs with a higher viscosity and lithosphere thickness, the magnitude of the modelled horizontal motion is 0.7-1.1 mm/yr less than in the 1D reference model.

The effect of a 3D Earth structure is less important in the FF than in GB. Lowering the viscosity in the southeast causes the FF velocities to be directed more Northward, but in general the direction of the FF motion is not affected by a 3D viscosity. The magnitude of the simulated horizontal motions at FF is relatively similar in all models, with most values between 2 and 3 mm a^{-1}.

A laterally varying lithosphere thickness has a similar effect to the direction of the modelled horizontal motion as a 3D viscosity. The effect of a different lithosphere thickness is strongest when a low viscosity is employed. In the FF, the direction of the horizontal velocities is found to be insensitive to variations in lithospheric thickness, and the magnitude of the velocities in the FF is only weakly sensitive (<0.4 mm/yr) to lithospheric thickness variations.

5.3.2. REALISTIC 3D MODELS

In this Section, I discuss horizontal motion generated by three realistic 3D models. First, 3D Earth structures derived from seismic models SL2013sv (*Schaeffer and Lebedev*, 2013) and SAVANI-US (*Porritt et al.*, 2021) are analysed. The magnitude of the lateral viscosity variations in these models is determined by the beta parameter. I also examine 3D models generated from WINTERC-G temperatures (*Fullea et al.*, 2021), in which the magnitude of the lateral viscosity variations is determined by the water content and the grain size.

Figure 5.6 shows the modelled horizontal velocities at Glacier Bay and at our chosen far field location. Velocities for SL2013sv and SAVANI-US are a little larger in Glacier Bay (1.8-4 mm/yr) than in the far field (1.4-3.8 mm/yr), but for WINTERC-G I find smaller velocities at Glacier Bay (mostly < 1 mm/yr) and significantly larger velocities at the far field location (1.5-5.5 mm/yr). All models do agree on the direction of the simulated horizontal motion at our two chosen locations, with horizontal velocities pointing South at Glacier Bay, and North/Northwest at the far field location.

Changing the beta parameter in models that are derived from seismic velocity anomalies like SL2013sv or SAVANI-US only has a minor influence on the direction and magnitude of the horizontal velocity at Glacier Bay (Figure 5.6a,c). I conclude that horizontal velocities at Glacier Bay, as modelled by 3D GIA models derived from seismic shear wave velocity anomalies such as SL2013sv or SAVANI-US, are not significantly different from 1D models. In the far field, I notice that increasing the value of beta does not change the direction, but it does enhance the horizontal velocities between 0 and 0.7 mm a^{-1} for a 0.1 increase in β, possibly due to slightly larger underlying shear wave anomalies in this area. Nevertheless, the magnitude of the horizontal velocities at both locations is still mostly determined by the imposed background viscosity η_0.

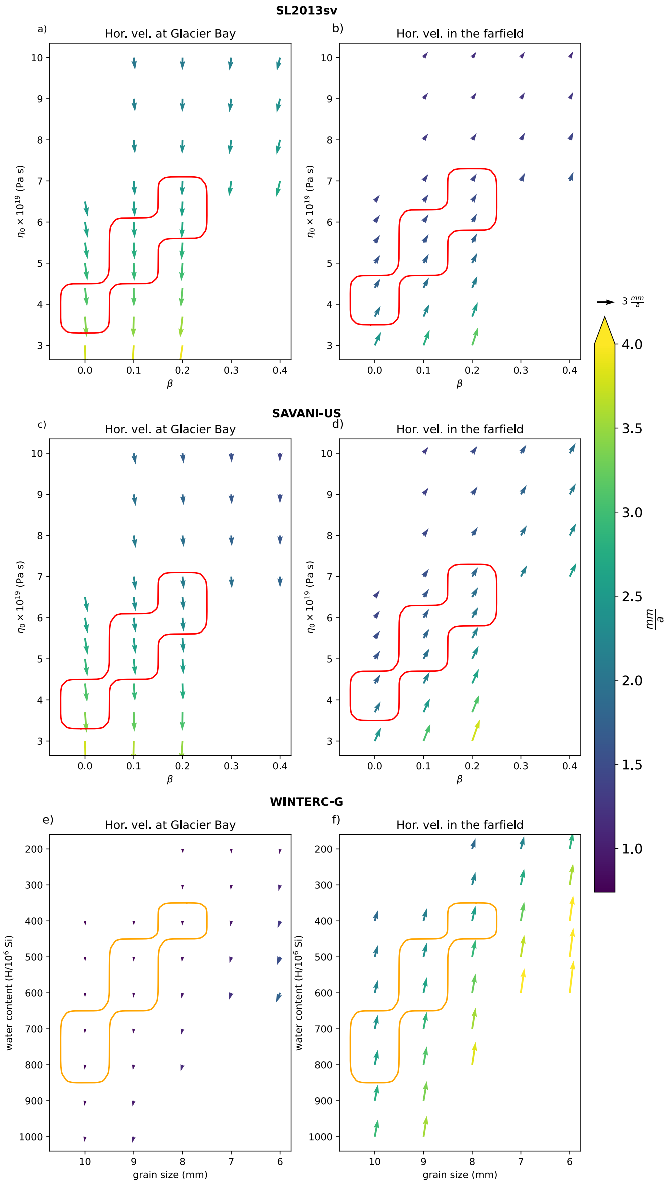

Figure 5.6: Modelled horizontal velocities at Glacier Bay and at a far field point for 3D Earth structures based on SL2013sv (a,b), SAVANI-US (c,d), and as derived from WINTERC-G temperatures(e,f). Circled in red and orange are models that best fit the uplift rate in *Marsman et al.* (2021). The x and y axis for subplots a-d denote the beta parameter and the background asthenosphere viscosity η_0. For subplots e and f, the x and y axis represent the grain size and the water content, respectively.

The smaller GB velocities in models derived from WINTERC-G temperatures are likely caused by the thicker lithosphere in this model (Figure 5.3f), as was noted by *Marsman* *et al.* (2021). A thicker lithosphere tends to smooth out the signal at the surface (*Wolstencroft et al.*, 2015), resulting in small values close to the base of the ice sheet where Glacier Bay is located (Figure 5.12). The region with the largest horizontal velocities, which is commonly around the ice edge, is now extended outwards. This explains why the far field velocities are larger in models generated from WINTERC-G temperatures than in models that are derived from seismic velocity anomalies.

The viscosity variations in models derived from WINTERC-G temperatures are unfortunately not determined by a single parameter, but by both the water content and the grain size. While this makes it difficult to isolate the effect of viscosity variations, I can still examine the effect of both parameters. A higher water content and a lower grain size both lead to lower viscosities. I find that horizontal velocities in both Glacier Bay and the far field are largest when the viscosity is low, i.e. when the water content is high or when the grain size is low. I moreover notice that the magnitudes of the horizontal velocities in the far field are more affected by the free parameters than those in Glacier Bay. This is in agreement with findings using SL2013sv and SAVANI-US models, where sensitivity to lateral variations is also larger in the far field than at Glacier Bay.

Next, I focus on the horizontal velocities of the realistic 3D models that best fit the GNSS uplift observations as determined by *Marsman et al.* (2021). Those best fit model runs are circled in red for models generated by SL2013sv and SAVANI-US (first two rows of Figure 5.6), and circled in orange for models that are derived from WINTERC-G (bottom row of Figure 5.6). For SL2013sv and SAVANI-US, I use the models that are explicitly denoted as best fit models in Figure 6a of *Marsman et al.* (2021), while the five best fit models for WINTERC-G are visually determined from Figure 6b of *Marsman et al.* (2021).

At Glacier Bay, the scatter in simulated horizontal motion is more than 1 mm a^{-1} among the best fit models derived by SL2013sv and SAVANI-US, with velocities between 2.1 and 3.4 mm a^{-1}. In the far field, the differences are smaller, and modelled horizontal GIA velocities vary between 1.4 and 2.0 mm a^{-1}. This indicates that the models that fit the uplift well can still differ in their simulated horizontal velocity, which means that horizontal GIA velocities can not simply be simulated using a single model that best fits observations of vertical motions.

The best fit models derived from WINTERC-G temperatures all simulate very small velocities in Hudson Bay ($\approx$ 0.8 mm/yr) and are also consistent in the magnitude and direction of the horizontal velocity in the far field (2.40-2.65 mm/yr in the Northwest direction). I conclude that the selection of best fit models that use 3D Earth structures derived from WINTERC-G do not result in significantly different simulated horizontal velocities.

5.3.3. APPLICATION OF 3D GIA MODELS TO TECTONIC BLOCK MODELS

In this section, I correct the GNSS velocities using 3D GIA model output, and investigate the effect of a 3D GIA model in existing tectonic block models (i.e. those from *Elliott and Freymueller*, 2020; *Elliott et al.*, 2010). I test the tectonic block models of both *Elliott et al.* (2010) and *Elliott and Freymueller* (2020) in order to infer the scatter caused by changes in the tectonic block model geometry. I run both block models with and without the

Glacier Bay Partition (GBP) so that I can compare this choice to the effect of 3D Earth structure variations in the GIA model. I utilise output from two GIA runs by *Marsman et al.* (2021) with Earth models that are generated using seismic velocity anomalies of SL2013sv. These are a 1D GIA run with $\beta = 0.0$ and $\nu = 3.7 \times 10^{19}$ Pa s, and a 3D GIA run with $\beta = 0.2$ and $\nu = 7 \times 10^{19}$ Pa s. I draw conclusions based on the assumption that both studies are equally relevant.

MODEL FITS

I assess how well the models fit the GNSS observations by calculating the reduced χ^2 value, χ^2_r, as done in *Elliott et al.* (2010) and *Elliott and Freymueller* (2020). This is not a straightforward comparison between models and data as usual, because the GIA models explain very little of the data and the mismatch can probably be absorbed by a change in block velocities. So looking at the best fit is a less than ideal way of assessing the models, but still the best I can do.

In these comparisons, a value of χ^2_r close to 1 means that the model is able to describe nearly all of the observations at the level of the measurement error, and a larger value shows that the models deviate from the observations more than can be explained based on the measurement errors. I exhibit χ^2_r for simulations using the 2010 block model (Figure 5.7a), and for runs using the more extensive 2020 block model (Figure 5.7b).

An important choice in the estimation of tectonic block velocities is whether or not to include the Glacier Bay Partition (GBP). *Elliott et al.* (2010) included the GBP for the first time, and showed that this inclusion improved the fit by ~ 10%. This agrees with findings in this study, which also show that the fit is improved for all models when including the GBP. F-tests showed that in all cases the inclusion of the GBP leads to a significantly improved fit, above the 99% confidence level. I investigate how this improvement compares to the effect of a 3D Earth structure in the GIA model next.

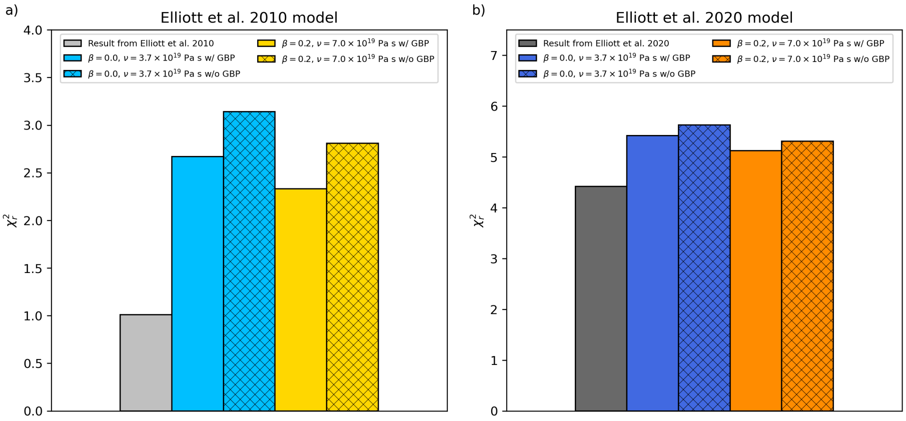

Figure 5.7: χ^2_r when combining GIA runs with a) the block model of *Elliott et al.* (2010), and b) the block model from *Elliott and Freymueller* (2020). The χ^2_r of the original 2010 and 2020 studies is shown in grey.

Applying the 3D model of *Marsman et al.* (2021) does improve the fit with respect to simulations performed using the 1D GIA model of *Marsman et al.* (2021). The effect of a 3D Earth structure can even be as important as the inclusion of the GBP for the block model from *Elliott and Freymueller* (2020). With this block model, similar fits are generated using a 1D model with the GBP and a 3D model without the GBP (Figure 5.7b). However, both 2010 and 2020 block models still results in a smaller misfit with the original studies' GIA model, rather than the GIA models of *Marsman et al.* (2021).

STRIKE-SLIP AND NORMAL MOTION

To infer if the effect of a 3D Earth structure within the GIA model is important, I investigate the tectonic interpretation of the resulting block model velocities. I examine the strike-slip motion and the normal motion as these define how the blocks within the plate model move with respect to each other. This relative movement determines the stress, which in turn regulates when faulting can occur. I conclude by assessing to what extent a 3D GIA model alters the tectonic setting.

The strike-slip motion and the normal motion are evaluated at four boundaries in the block models: Southern Fairweather, The Glacier Bay Partition (GBP), the Eastern Denali fault and at the Coast Shear zone (Figure 5.1). The Fairweather boundary accommodates most of the relative motion between the Pacific and North America plate (*Mazzotti et al.*, 2003). The GBP is interesting due to its proximity to the Glacier Bay ice fields, as well as being a proposed fault, but not an established one. The Eastern Denali fault and the fault at the Coast Shear zone are located further inland (Figure 5.1). Investigating the relative motion along those faults helps us to describe how crustal motion is propagated inland.

Previous estimates of the strike-slip and normal motion along those boundaries are listed in Table 2 of *Elliott and Freymueller* (2020), and exhibited in grey in Figures 5.8 and 5.9. In this study, I focus on results that use the GIA models from *Marsman et al.* (2021). I have selected two GIA simulations from this study: a 1D GIA model with β=0.0 and $\nu = 3.7 \times 10^{19}$ Pa s, and a 3D GIA model where β=0.2 and $\nu = 7 \times 10^{19}$ Pa s. Both models provide a reasonable fit to uplift observations (*Marsman et al.*, 2021).

Strike-slip motion at the Southern Fairweather fault is fairly similar among all models, with slip around 45 mm/yr (Figure 5.8). This large value is expected as the Fairweather fault accommodates the majority of the relative motion between the Pacific plate and the North America plate (*Mazzotti et al.*, 2003). Models without the Glacier Bay Partition (GBP) simulate a little more slip than those with the GBP (< 2 mm a^{-1}). The Fairweather fault is insensitive to lateral variations in the GIA model.

For the other three locations, the slip is significantly smaller and depends on the location and the model. Strike-slip motion at GBP is roughly 2.5 mm/yr for all models that contain this partition, with only the 2010 reference model simulating less slip (1.5 mm/yr). Eastern Denali is very sensitive to the specific GIA and block models employed. The slip may be as low as 0.5 mm/yr for the 2010 block model with GBP combined with the 1D GIA model from *Marsman et al.* (2021) (light blue bar in top row of Figure 5.8), but it can also be as high as 3.5 mm/yr for the 2020 block model without GBP together with the

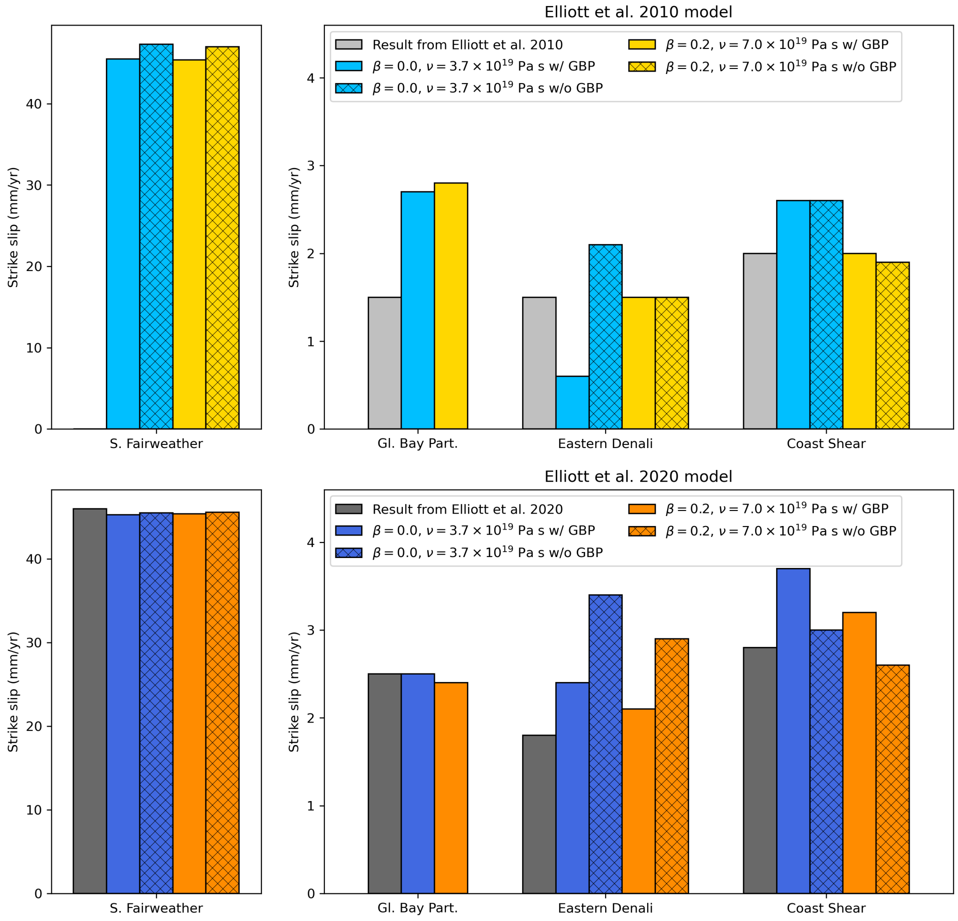

Figure 5.8: Strike-slip velocity at four faults in Southeast Alaska. The locations of these faults are indicated in Figure 5.1. The top row shows results using the 2010 block model of *Elliott et al.* (2010), and the bottom row exhibits results using the 2020 block model of *Elliott and Freymueller* (2020). The block models are run with a 1D model of *Marsman et al.* (2021) where β=0.0 and $\nu = 3.7 \times 10^{19}$ Pa s, and with a 3D GIA model of *Marsman et al.* (2021) where β=0.2 and $\nu = 7 \times 10^{19}$ Pa s. The GIA models of *Marsman et al.* (2021) are run using the block models with the Glacier Bay Partition (GBP), and then another time without the GBP. The results using the reference GIA models of *Elliott et al.* (2010) and *Elliott and Freymueller* (2020) are shown in grey.

same 1D GIA model from *Marsman et al.* (2021) (dark blue bar with crosses in bottom row of Figure 5.8). The slip at the coast shear zone is smaller when the 2010 block model is used (roughly 2.0-2.5 mm/yr) than when the 2020 block model is employed (around 3.0 mm/yr).

This strike-slip at GBP is not sensitive to 3D Earth structure variations in the GIA model. When utilising the 2020 block model, I find that for Eastern Danali the effect of 3D GIA is less important than the inclusion of the GBP. Employing a 3D GIA model reduces strike-slip at the Coast Shear zone.

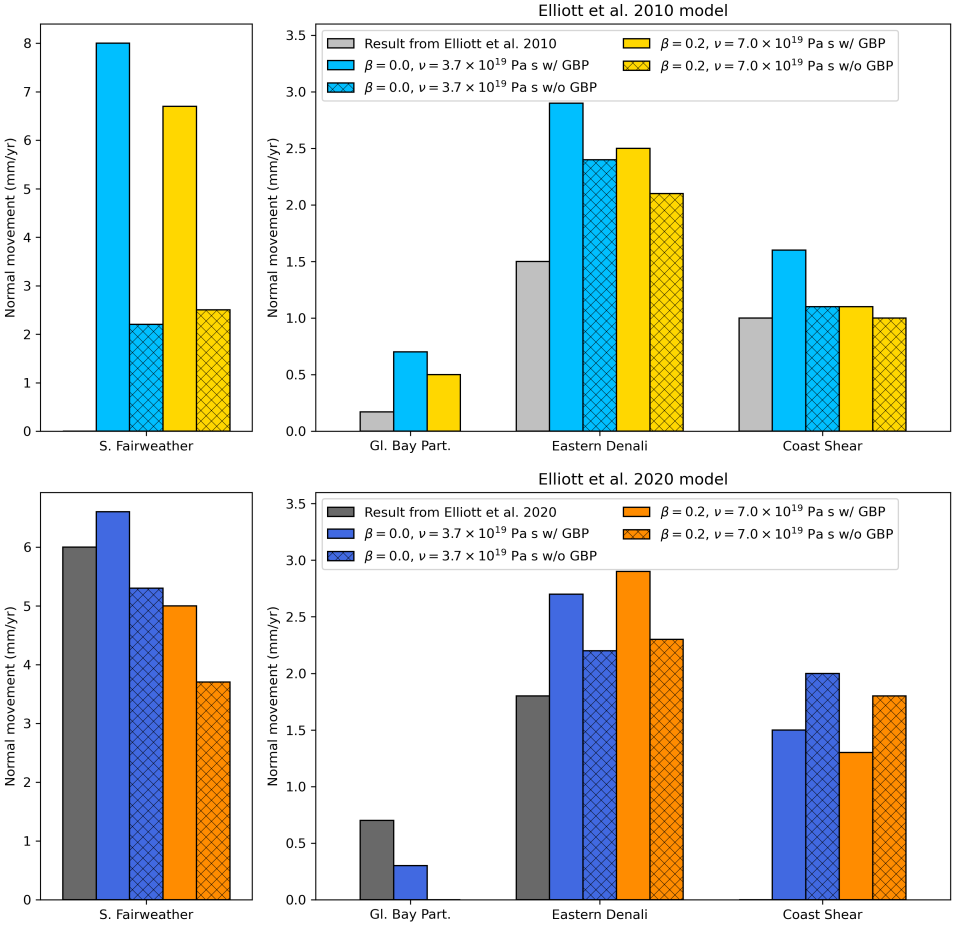

Figure 5.9: Normal motion at four faults in Southeast Alaska. The locations of these faults are indicated in Figure 5.1. The top row shows results using the 2010 block model of *Elliott et al.* (2010), and the bottom row exhibits results using the 2020 block model of *Elliott and Freymueller* (2020). The block models are run with a 1D model of *Marsman et al.* (2021) where β=0.0 and $\nu = 3.7 \times 10^{19}$ Pa s, and with a 3D GIA model of *Marsman et al.* (2021) where β=0.2 and $\nu = 7 \times 10^{19}$ Pa s. The GIA models of *Marsman et al.* (2021) are run using the block models with the Glacier Bay Partition (GBP), and then another time without the GBP. The results using the reference GIA models of *Elliott et al.* (2010) and *Elliott and Freymueller* (2020) are shown in grey.

The normal motion at the Southern portion of the Fairweather fault varies between roughly 2.0 mm/yr and 8.0 mm/yr depending on the model employed (Figure 5.9). Here, block models without the GBP estimate a lower normal movement than those same models that include the GBP, so I conclude that employing a GBP reduces the normal movement at the Southern Fairweather fault. 3D variations in the GIA model also reduce the normal movement at Fairweather, but only with the 2020 block model 3D GIA is found to be as important as the inclusion of the GBP.

At the GBP location itself, the normal movement is very small in all models (less than 1.0 mm/yr). At Eastern Denali, the new GIA models give larger amounts of normal movement (2.0 - 3.0 mm/yr) than the 2010 and 2020 reference models which simulate less than 2.0 mm/yr of normal motion. Excluding the GBP is found to be more important than the effect of 3D GIA, when 3D GIA models are selected based on their fit to uplift data, and reduces the normal movement at Eastern Denali. The normal motion at the Coast Shear zone is between 1.0 and 2.0 mm/yr in all models. I find the effect of 3D GIA variations to be less important than the inclusion of the GBP when using the 2020 block model. With the 2010 block model results are less conclusive.

5.4. DISCUSSION

The 3D Earth structures discussed in this study are derived from seismic velocity anomalies and absolute temperatures, and result in a viscosity gradient from Southeast to Northwest. I have investigated the schematic effect of such a viscosity gradient with a sensitivity study. The lateral Earth structures incorporated here promote a more Northward GIA movement in the far field. However, an extra eastward GIA component appears to better resolve differences in observed velocities. Such an eastward GIA component may be generated using a 3D GIA model that employs a 3D Earth structure based on oceanic-continental differences.

The expected lateral changes are smaller with depth, which makes large viscosity changes less likely. While the shear wave anomalies are up to 7.5% at 80 km depth (Figure 5.3), they are not larger than 4.5% at a depth of 140 km (Figure 5.11). The sensitivity study employs lateral Earth structure variations which do not diminish with depth in the 230 km thick asthenosphere, and therefore shows an exaggerated version of what lateral variations in Earth structure can do. It nevertheless helps us to understand the effect of a 3D Earth structure on the GIA in Alaska.

The GIA model could furthermore be improved by including the effect of the deglaciation of the Laurentide ice sheet, something that is currently not done by this study or by the studies of *Elliott et al.* (2010) and *Elliott and Freymueller* (2020). *Sella et al.* (2007) show that this deglaciation may have a significant effect in Alaska, but they also find a large variability in the modelled horizontal motion resulting from GIA depending on the viscosity beneath North America. This large variability inhibits us to include and constrain the contribution of the Laurentide ice sheet.

The tectonic block models consistently fit worse when the new GIA models by *Marsman et al.* (2021) are used instead of the more simple GIA models in *Elliott et al.* (2010) and *Elliott and Freymueller* (2020). A possible reason for this is that most sites with large residuals have time series that are short (i.e. not resurveyed after 2007). In order to pinpoint the importance of this for the fit, I need longer timeseries and therefore also a way to deal with the post-seismic effects of the 2012 Haida Gwaii and 2013 Craig earthquakes (*Aiken et al.*, 2015; *Ding et al.*, 2015; *Lay et al.*, 2013).

For testing the fit against the tectonic block models, I have used two GIA models of *Marsman et al.* (2021). These GIA models simulate deformation on a material compressible

Cartesian Earth. As can be seen in *Reusen et al.* (2023), this thesis, the simulated horizontal displacement rate of material compressible cartesian models is smaller than that of fully compressible cartesian models. Adding full compressibility to a GIA model does however not change the direction of the GIA signal, meaning that an east-west GIA component is not created if it is not already present in the material compressible model.

Another possibility for why the observed horizontal GNSS points North in Glacier Bay and Northeast in the far field is the collision of the Yakutat block with North America. This block is situated in the corner of the Gulf of Alaska, but its collision with North America may have effects far away from its collisional boundary (*Leonard et al.*, 2007). This collision could therefore introduce an eastward component of the GNSS velocities at the far field. Nevertheless, this study shows that the incompatibility of the velocities can also be caused by the simplistic GIA correction utilised in current tectonic block model studies.

The Glacier Bay Partition (GBP) is the only block boundary that is not tied to a known fault. *Elliott et al.* (2010) suggest that the GBP represents internal deformation, rather than an existing fault. This would agree with the hypothesis that the eastward component of the GNSS velocities north of Glacier Bay is due to strain transferred by the collision of the Yakutat block (*Leonard et al.*, 2007). A small shift in location of the GBP seems plausible, as altering the orientation of this boundary did not change the fit a lot (Jeffrey Freymueller, personal communication).

5.5. CONCLUSION

I have investigated the effect of a 3D Earth structure on horizontal motion due to GIA in Southeast Alaska. Sensitivity tests showed that the effect of a low viscosity area in the Southeast of the domain is a net movement from the region of low viscosity to that of higher viscosity. However, *Kaufmann et al.* (2005) found the opposite for Antarctica, with horizontal motion from high viscosities in East Antarctica to lower viscosities in West Antarctica. Antarctica covers a larger area than Southeast Alaska, and also experienced more recent ice melt events, which both could explain the difference.

More realistic 3D Earth structures show that GIA model results are heavily dependent on the approach taken to derive the lateral Earth structure variations. Horizontal velocities at Glacier Bay are considerable (1.8 - 4 mm a^{-1}) in 3D GIA models derived from seismic anomalies, but small ($<$ 1 mm a^{-1}) using 3D Earth structures deduced from WINTERC-G temperatures. Moreover, the best fit models derived from seismic anomalies differ more than 1 mm a^{-1} in Glacier Bay. This means that even when GIA models are selected based on their fit to uplift rate data, a scatter in horizontal velocities remains.

Using a GIA model with 3D Earth structure improves the block model fit as compared to the 1D GIA models of *Marsman et al.* (2021). This improvement is however less important than the inclusion of the Glacier Bay Partition (GBP). Including the GBP also improved the fit when using the new GIA models of this study.

Future research could be done on several aspects discussed here. First, a 3D Earth structure based on ocean-continent differences can be generated. Second, the effect of the deglaciation of the Laurentide ice sheet on GIA in Alaska should be quantified as this can clearly be significant (*Sella et al.*, 2007). Another investigation that can be done is to test the sensitivity to different block model geometries, and investigate how much a block model fit can be improved when the geometry is tailored to each individual GIA model.

5.6. APPENDIX A: BENCHMARK TO THE MODEL USED IN MARSMAN ET AL. (2021)

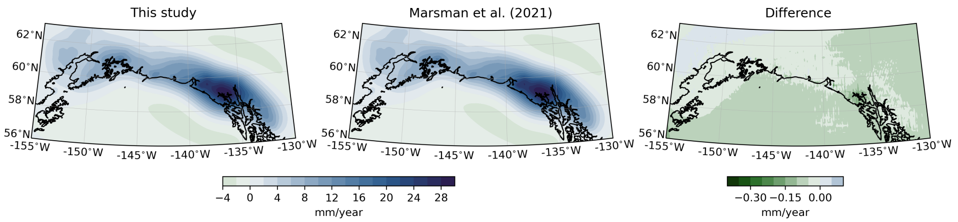

Figure 5.10: Uplift rates between 2003 and 2012 for a) the model of this study, b) the model of *Marsman et al.* (2021), and c) the difference. For this benchmark, I have taken the Earth model values and the layer configuration from Table S1 and Table S2 of *Marsman et al.* (2021), respectively. The benchmark runs have been performed using the incompressible versions of both models.

5.7. APPENDIX B: LATERAL VISCOSITY AT A DEPTH OF 140 KM

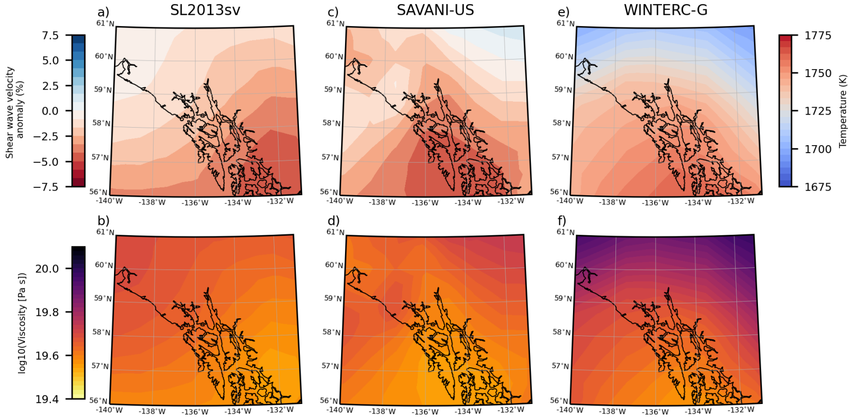

Figure 5.11: The input values as in Figure 5.3, but not at a depth of 140 km. The top row subplots show the input from which the viscosity profile is determined, and in the bottom row the resulting viscosity profile is exhibited for the best fit model parameters according to *Marsman et al.* (2021). The viscosity profiles for SL2013SV (a,b) and Savani (c,d) are determined from seismic shear wave velocity anomalies, and temperatures are used as input for the WINTERC model (e,f).

5.8. APPENDIX C: 3D DEFORMATION

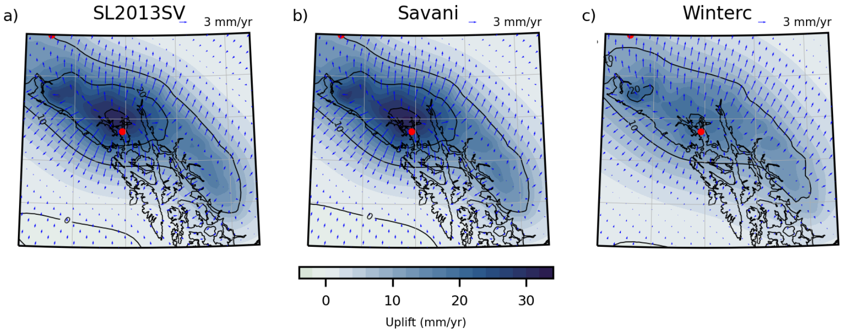

Figure 5.12: Modelled 3D deformation using the best fit model parameters as found by *Marsman et al.* (2021). GIA model results of SL2013SV (a) and Savani (b) generate higher peak uplift than the model that is based on WINTERC temperatures (c). The deformation in WINTERC appears to be more widespread than the signal resulting from SL2013SV and Savani.

6

CONCLUSION AND RECOMMENDATIONS

With improved computational techniques and resources, I was able to improve models for the gravity field and horizontal motion due to Glacial Isostatic Adjustment (GIA). Several effects have been studied, such as mantle flow, compressibility, and 3D structure of the lithosphere and mantle. Improving current models increases the validity of the simulations, but also increases the complexity. To better understand these effects, I have formulated key questions pertaining to Chapter 3, 4, and 5 of this thesis. In Section 6.1, I answer these key questions. Section 6.2 provides recommendations for the future of numerical modelling of GIA with regards to horizontal velocities and static gravity.

6.1. ANSWER TO RESEARCH QUESTIONS

RS1:How can the long-wavelength gravity field of North America be modelled best?

Accurate modelling of the gravity field requires the inclusion of contributions of the crust (*Root et al.*, 2015), mantle convection, and Glacial Isostatic Adjustment (GIA). Mantle convection and GIA are not considered in the force balance of previous gravity field studies for North America (e.g., *Métivier et al.*, 2016). However, in this thesis, the forces of mantle convection and GIA are included in the force balance, and are applied at the bottom of the crustal model. In Chapter 3, I use this force balance to determine the density in the lithosphere. The calculated lithosphere density and all other structures and densities in the crustal model are then used to generate the gravity field.

Crustal model uncertainties were found to be too large to simulate the gravity field over Fennoscandia (*Root et al.*, 2015). Therefore, I investigated the imprint of the GIA signal on the gravity field for an even larger area, namely North America (Chapter 3). I found that the location and amplitude of the GIA imprint on the gravity field are retained for wavelengths of more than 600 km. I then tested the sensitivity of the gravity field to uncertainties in the crustal model. I did so by changing 1) the crustal density profile, 2) the crustal thickness, and 3) the depth of the Lithosphere-Asthenosphere Boundary (LAB). Crustal model uncertainties were found to be small compared to the magnitude of the observed signal, which is about 50 mGal over Hudson Bay. Sensitivity to the adopted crustal density is < 7 mGal, and the uncertainties due to the crustal thickness and the depth of the LAB are found to be < 5 mGal. The calculated lithosphere density below Hudson Bay is between 3300 $\mathrm{kg/m^3}$ and 3340 $\mathrm{kg/m^3}$. I concluded that the crustal model uncertainty is small enough for simulating wavelength signals of more than 600 km over North America.

The processes of mantle convection and GIA are both controlled by the viscosity of the Earth's mantle. By being consistent with the mantle viscosity in our mantle convection and GIA models and accounting for the effects of these processes on the force balance, I could obtain a robust value of the viscosity. Model results match gravity field observations best for lower mantle viscosities larger than 10^{22} Pa s, independent of the adopted ice model. These results agree with global geodynamic modelling studies (e.g., *Bower et al.*, 2013; *Perry et al.*, 2003; *Steinberger and Calderwood*, 2006). For such high values of the lower mantle viscosity, the relaxation time is longer and the remaining uplift is larger. This translates to a larger contribution of GIA to the gravity field. In this preferred scenario, GIA has a contribution to the observed gravity field anomaly over North America of more than 60%. Previous estimates of the relative GIA contribution to this gravity field anomaly range from 15% to 80% (e.g., *James*, 1992; *Métivier et al.*, 2016; *Tamisiea et al.*, 2007), so our estimate is at the higher end of these values. Lower mantle viscosities $> 10^{22}$Pa s are also preferred in ice reconstruction studies that aim to match sea level observations (*Gowan et al.*, 2021). However, the widely used ice-history model ICE-6G is generated using a lower mantle viscosity of less than 10^{22} Pa s (*Argus et al.*, 2014; *Peltier et al.*, 2015), although the viscosity underlying the newer ICE-7G_NA model does increase to values around 10^{22} deeper in the lower mantle (*Roy and Peltier*, 2017). Ice sheet histories based on a viscosity profile with viscosities $>10^{22}$ Pa s do exist, such as ice sheet model LW-6 by *Lambeck et al.* (2017). Based on the conclusions of Chapter 3, the combination of ice sheet histories such as LW-6 with an Earth model containing larger lower mantle viscosity is preferred over North America.

> *RS2: How can the horizontal motions of GIA be modelled using 3D finite element models based on Abaqus?*

Horizontal motions of GIA are modelled routinely, but interpreting observed horizontal motions in terms of GIA is difficult for three reasons. First, horizontal motions are very sensitive to the compressibility of mantle rock which in some cases enhances these motions by a factor two (*Tanaka et al.*, 2011). Including compressibility requires including the internal buoyancy force in the equation of motion, and this is known to lead to instabilities over time (*Hanyk et al.*, 1999; *Plag and Jüttner*, 1995; *Vermeersen and Mitrovica*, 2000). Therefore, compressibility is not included in most models. Second, observations of horizontal motions are often dominated by tectonic motions, so small errors in tectonic motion estimates could be interpreted as GIA motions. The third problem is that horizontal motion related to GIA is very sensitive to lateral variations in viscosity (e.g., *Gasperini et al.*, 1990; *Kaufmann et al.*, 2005; *Latychev et al.*, 2005; *O'Keefe and Wu*, 2002; *Steffen et al.*, 2006). Therefore, it is important to employ a GIA model that allows for lateral Earth structure variations.

In this thesis, compressible deformation is simulated with commercial Finite-Element (FE) software Abaqus. The addition of the internal buoyancy force to FE models of Abaqus is not trivial (*Bängtsson and Lund*, 2008; *Wong and Wu*, 2019). I include compressibility using the approach outlined by *Hampel et al.* (2019). In this approach, the force of gravity is explicitly applied to the model and the effect of prior deformation on the forcing is included. I found that the method of *Hampel et al.* (2019) can only be applied to Cartesian models and not to spherical models, as gravity can not be applied in the radial direction within the FE software. Therefore, I focused on the implementation of this method in Cartesian GIA models. I was able to simulate the effect of compressibility better than models that employ material compressibility, which is the form of compressibility currently employed in several GIA models of Abaqus (e.g., *Auriac et al.*, 2013; *Kaufmann et al.*, 2005; *Lund et al.*, 2009; *Marsman et al.*, 2021; *Nield et al.*, 2018; *Steffen et al.*, 2006). With material compressibility, the material is allowed to compress, but the internal buoyancy force is not present (*Klemann et al.*, 2003). Material compressibility does not lead to instabilities, and is a reasonable approximation of compressibility for small ice sheets (Chapter 4). The effect of the internal buoyancy force becomes increasingly important for larger ice sheets as the density changes due to deformation are larger. Cartesian GIA models are not able to simulate the horizontal motion of ice sheets with radii larger than 200 km well, so the increasingly important buoyancy force is not a problem for Cartesian models that aim to model horizontal motion.

In Chapter 4 (Section 4.4.2), I used 1D spherical normal mode models and Cartesian FE models to simulate horizontal displacement rates due to GIA for an ice load with a radius just over 200 km and a constant thickness of 200 m. The magnitude of the simulated horizontal displacement rates was 5-7 mm/yr, in agreement with values modelled by *Elliott et al.* (2010). The largest horizontal displacement rates are simulated by the compressible spherical model. The horizontal displacement rates simulated by the incompressible spherical model are 1.5 mm/yr smaller. The Cartesian models also simulate smaller displacement rates than the compressible spherical model. The horizontal displacement rates are 0.63 mm/yr smaller with the compressible Cartesian model and 0.93 mm/yr smaller with the material compressible Cartesian model. The global GNSS measurement uncertainty is typically 0.5 mm/yr for horizontal displacement rates (*Vardić et al.*, 2022), and can be less than 0.35 mm/yr for regional GNSS measurements depending on the chosen noise model (*Kierulf et al.*, 2021; *Lahtinen et al.*, 2019). The effect of compressibility (1.5 mm/yr) is therefore significant with respect to the current measurement uncertainty (0.35-0.5 mm/yr). Even the effect of sphericity (0.63 mm/yr) is above the measurement accuracy. The inclusion of full compressibility in Cartesian models only provides a minor improvement of 0.3 mm/yr with respect to Cartesian GIA models employing material compressibility.

Furthermore, Cartesian models generally do not include self-gravity. For simulations of vertical deformation the lack of self-gravity is compensated by the lack of sphericity (*Amelung and Wolf*, 1994). This compensation mechanism allows Cartesian models to be reasonably accurate for simulating vertical movement due to ice sheets up to the size of the Fennoscandian ice sheet (*Amelung and Wolf*, 1994; *Wu and Johnston*, 1998). I found that, unfortunately, this degree of compensation does not take place for horizontal motion. Consequently, Cartesian GIA models are only applicable for simulations of horizontal GIA deformation in small-scale areas like Iceland or Alaska. Simulating large ice sheets, like those in North America and Scandinavia, requires spherical models in order to accurately model the horizontal motion of GIA. In these large areas, it is also important that the model is coupled to the Sea Level Equation. A compressible global spherical FE model coupled to the Sea Level Equation is recently realised in Abaqus by *Huang et al.* (2023).

> *RS3: What is the effect of compressible 3D GIA models on the block model predictions in Southeast Alaska?*

Alaska is a tectonically complex region that has been subject to several seismic events in the past century (*Doser and Lomas*, 2000). With improved understanding of the tectonic motion in the area, the observed topography and seismic activity can be explained better. The tectonic motion in Alaska has been studied using GNSS observations (e.g., *Elliott and Freymueller*, 2020; *Elliott et al.*, 2010). These studies divided the region in tectonic blocks with boundaries that are either based on seismic and geologic evidence of recognised faults or are previously postulated faults or fault zones. For each block, an Euler pole and angular velocity are estimated from the observed velocities. These block models exist for the whole of Alaska (*Elliott and Freymueller*, 2020), but also specifically for Southeast Alaska (*Elliott et al.*, 2010).

Southeast Alaska contains many ice fields and glaciers, and experiences significant glacial isostatic adjustment of about 30 mm/yr in the vertical (*Larsen et al.*, 2005) and up to 7 mm/yr in the horizontal (*Elliott et al.*, 2010). The horizontal crustal movement of GIA needs to be removed before any tectonic motion can be deduced. In previous tectonic block model studies, a 1D GIA model has been used to correct the observed GNSS velocities (*Elliott and Freymueller*, 2020; *Elliott et al.*, 2010). The interior of Alaska is not homogeneous and, as discussed, horizontal motion of GIA is very sensitive to lateral Earth structure. This raises the question (RS3) whether a more accurate GIA model with 3D Earth structures would improve our understanding of the tectonic motion in Alaska.

In Chapter 5, I have generated GIA models for three sets of 3D viscosity distributions. Two sets of these are derived from seismic shear wave velocity anomalies which are assumed to be at least partly caused by temperature anomalies, a technique applied by several previous studies (e.g., *Latychev et al.*, 2005; *Li et al.*, 2018; *Steffen et al.*, 2006). The magnitude of the lateral viscosity variations in these sets is determined by the β parameter, which determines the portion of the seismic velocity anomalies that is related to anomalies in temperature. These two sets differ in underlying seismic model from which the shear wave velocity anomalies are generated, but the technique to calculate the 3D viscosity distributions is the same. The other set is determined from absolute temperatures using olivine flow laws for the upper mantle (as in *Blank et al.*, 2021; *van der Wal et al.*, 2013, 2015). The absolute temperatures used in this method are obtained from WINTERC-G (*Fullea et al.*, 2021), which combines satellite gravity with seismic data and data on heat flow and surface elevation. For each set, I determined a subset of model runs that best fit the uplift data using χ^2 misfits as in *Marsman et al.* (2021). I found that horizontal motion of best fit GIA models with 3D Earth structures derived from seismic shear wave velocity anomalies are 1.8-4 mm/yr in Glacier Bay. The magnitude of the horizontal velocity in Glacier Bay can consequently differ by more than 1 mm/yr within the best fit models derived from seismic shear wave velocity anomalies. However, the simulated horizontal motion for these sets is not sensitive to the value of the β parameter, but more to the value of the background viscosity. Therefore, the simulated horizontal motion at Glacier Bay is not that different in 3D and 1D GIA models. Nevertheless, even when GIA models are selected based on the fit to uplift data, a scatter in simulated horizontal motion remains. This scatter is not visible in best fit 3D models derived from absolute temperature using flow laws. In these models, the simulated horizontal motion in Glacier Bay is small (< 1 mm/yr), presumably due to the thicker lithosphere of these models, which stems from the underlying upper mantle model WINTERC-G.

To finally assess the effect of 3D GIA models on block model predictions in Alaska, I estimated tectonic block motion with two material compressible GIA models from *Marsman et al.* (2021), one with 1D Earth properties and the other with 3D Earth structure. Using the 3D GIA model reduced the χ^2_r misfit of the tectonic block model to GNSS observations, as compared to the fit using the 1D GIA model. However, other choices made in the processing were found to be as important for the value of χ^2_r. For example, including or excluding a tectonic block boundary through Glacier Bay was at least as important for the fit. Therefore, I concluded that tectonic block motion estimates obtained with 1D GIA models are still valid.

The main conclusions of this thesis can be summarised as follows:

- Models for the long-wavelength gravity field of North America can be improved by including both GIA and mantle convection in the force balance. Using this improved force balance in our gravity field model, I match the observed gravity field anomaly best for lower mantle viscosities of more than 10^{22} Pa s.
- Compressibility can be included in Abaqus in a straightforward manner for multilayer Cartesian models. Horizontal GIA motion can be simulated with sufficient accuracy using such models for ice sheets with radii smaller than 200 km. For such small ice sheets, I found that Cartesian models that correctly implement compressibility are somewhat more accurate than Cartesian models employing material compressiblity.
- Lateral Earth structure in the GIA model affects tectonic block model predictions in Southeast Alaska, but is not more important than the configuration of the faults in the area. For tectonic model predictions in Southeast Alaska, both the tectonic block model configuration and the GIA model should be varied simultaneously to find the best fitting combination. This best fitting combination teaches us not only about the magnitude of lateral Earth structure variations in Southeast Alaska, but also about the configuration of the faults.

This thesis provides novel ways to model or investigate the gravity anomalies and horizontal motion induced by GIA. Future research building on our findings and other applications of the modelling frameworks presented in this thesis are discussed in the following section.

6.2. RECOMMENDATIONS

This Section describes recommendations for future research. First, I list a few recommendations for future research on the static gravity field. After, I focus on horizontal crustal motions due to GIA. I end by listing some research suggestions specifically for Southeast Alaska. For each of these topics, I start by mentioning recommendations that are directly linked to research of this thesis, and can be considered as improvements that can readily be made. After, I zoom out and suggest more general future research possibilities for each topic.

COUPLE MORE COMPLICATED MANTLE CONVECTION AND GIA MODELS TO THE CRUSTAL MODEL

A straightforward improvement in the gravity modelling framework would be to couple more complicated mantle convection and GIA models to the crustal model of Chapter 3. At the moment, both codes allow only for radial variations in mantle viscosity. The Earth's interior properties are inhomogeneous, and it would be interesting to investigate the effect of Lateral Viscosity Variations (LVVs) on the modelled gravity field. Previous mantle convection studies found that the effect of LVVs in the upper mantle on the geoid can be significant (e.g., *Čadek and Fleitout*, 2003). LVVs in the lower mantle do affect the geoid when created from slab models, but have an insignificant effect on geoids generated by tomography models (*Ghosh et al.*, 2010). A low viscosity zone in the Earth's crust induces geoid changes up to 1 meter on spatial scales of more than a few hundred km (*Van der Wal et al.*, 2004).

LINKING OBSERVATIONS OF THE LONG-WAVELENGTH GRAVITY FIELD TO MANTLE CONVECTION OR GIA IN AREAS ON EARTH OTHER THAN HUDSON BAY

Long-wavelength gravity field anomalies are caused by crustal inhomogeneities, mantle convection and GIA. In Chapter 3, I have combined these contributions in order to generate a combined model which is able to explain the observed gravity field. Due to the current resolution of the crustal density and structures, the uncertainty in the crustal model component increases for smaller scale signals. This uncertainty is even found to be too large to explain the long-wavelength gravity field of Fennoscandia (*Root et al.*, 2015). Nevertheless, based on our results for North America, the combined model should be applicable in all areas where gravity anomalies with wavelengths > 600 km exist. Observations of the gravity field are accurate and provide an excellent way to constrain and improve models for crustal inhomogeneities, GIA or mantle convection. In areas where GIA is not expected to play a role, this part of the combined model can be omitted, and mantle convection can be used together with crustal models to investigate the area. Figure 1.2 highlights global gravity field for wavelength of > 600 km or more. Based on Figure 1.2, potentially interesting future research areas are Greenland, India, and Indonesia, provided that the crustal model in those areas is sufficiently accurate.

APPLY THE COMPRESSIBLE CARTESIAN GIA MODEL TO INVESTIGATE HORIZONTAL MOTIONS IN ICELAND

The compressible Cartesian GIA model allows for investigating the effect of 3D Earth structure on horizontal motion in other small-scale areas like Iceland. Previous research already identified that horizontal motions are sensitive to lateral variations in Earth structure, but it is particularly interesting to investigate the importance of these lateral variations in Iceland. Iceland is located on a spreading ridge, and observed velocities are small (up to 3 mm/yr), but show a coherent pattern away from Vatnajökull and the smaller glaciers, presumably due to GIA (*Árnadóttir et al.*, 2009). A 3D Earth structure could be implemented in the form of a lithospheric cooling model due to Iceland's location on a spreading ridge. Using a 3D GIA model may reduce residual horizontal and vertical velocities in the area. Furthermore, the effect of a 3D GIA model on deformation data can be investigated to improve the monitoring of subglacial volcanoes on Iceland by obtaining more information on the stresses within the crust.

APPLY A 3D COMPRESSIBLE SPHERICAL FINITE ELEMENT MODEL TO OBSERVATIONS OF HORIZONTAL MOTION IN NORTH AMERICA

Huang et al. (2023) developed a 3D compressible spherical Finite Element model for GIA research that is applicable to realistic loads. This model can now be used for several locations on Earth experiencing GIA, such as North America. Such a model enables a systematic investigation on the effect of lateral Earth structure and power law rheology for horizontal GIA motions on a larger scale than done in this thesis. *Sella et al.* (2007) show a wide range of modelled horizontal GIA velocities in North America, depending on the mantle viscosity, but none of their modelled horizontal GIA velocities fit the GPS data. With the model of *Huang et al.* (2023), modelled horizontal velocities can be compared to observed horizontal GNSS velocities. Since horizontal velocities have a depth sensitivity that is different from other GIA observables like vertical motion and sea level (*Wu*, 2006), such a study has to potential to reveal more of the structure of the Earth's interior.

If I want to implement compressiblity in spherical models using the method of *Hampel et al.* (2019), I encounter two problems. First, gravity can not be applied radially in a straightforward manner within the FE software. This can be partly circumvented by applying a radial body force using subroutines. Second, the non-linear geometry as described in Chapter 4 and *Hampel et al.* (2019) is only available when the gravitational force is set within the FE software. With this non-linear geometry setting, the internal buoyancy force for compressible models is included. As gravity is now set as a body force outside the FE software, the internal buoyancy force is not automatically calculated, because the density change due to deformation is not considered. This density change needs to be calculated outside of the FE software using the dilatation of the elements, which is effectively what is done by *Huang et al.* (2023). So as long as gravity can not be directed radially within the FE software, compressible deformation on a sphere with Abaqus might as well be simulated using the model of *Huang et al.* (2023).

In case it becomes possible to direct the gravity radially inwards with this method, then gravity needs to be compensated by applying an initial stress (Chapter 4). The theoretical equations for the stresses in a homogenous sphere under gravity are given by *Yoffe* (1996) in case Poisson's ratio ν is equal to 0.25. The more general equations for these stresses are shown below, derived from §98 of *Love* (1927):

$$\sigma_{rr} = \frac{4}{3}\pi \frac{\rho_0 G (3-\nu)}{10(1-\nu)} \left(R^2 - a^2\right) \tag{6.1}$$

$$\sigma_{\theta\theta} = \sigma_{\phi\phi} = \frac{4}{3}\pi \frac{\rho_0 G (3-\nu)}{10(1-\nu)} \left[(3\nu+1) R^2 - (3-\nu) a^2\right] \tag{6.2}$$

In these equations, ρ_0 is the background density, G is the gravitational constant, ν is Poisson's ratio, R is the radial coordinate of the element in the model, and a is the radius of the Earth. I briefly validated these Equations with the help of Abaqus. Using subroutines, I applied a radial body force to a fictional homogeneous elastic sphere with a density of 5510 $\mathrm{kg/m^3}$, Poisson's ratio of 0.33, and a gravitational constant of $6.67408 \times 10^{-11}\ \mathrm{N \cdot m^2/kg^2}$. The resulting stresses in Abaqus match with the theoretical stresses described by Equations 6.1 and 6.2 (Figure 6.1). Moreover, equations 6.1 and 6.2 are easily extendable to layered Earths. I conclude that these initial stresses can indeed be applied to a spherical Abaqus model under gravity loading.

MODEL TECTONIC BLOCK MODELS TOGETHER WITH GIA

Lateral Earth structure in the GIA model affects tectonic block model velocities (Chapter 5). In existing studies, the observed GNSS velocities are corrected for GIA independently of the applied tectonic block model (e.g., *Elliott and Freymueller*, 2020; *Elliott et al.*, 2010). However, the ideal scenario is that small adjustments are made to the block model and these are estimated together with several 3D GIA models, to infer the combination that best explains observations. This requires generating a number of 3D GIA models that are then used together with several block model geometries to generate the best combination. This can help further identify boundaries that are sensitive to the adopted GIA model.

DETERMINE OPTIMAL LOCATIONS FOR FUTURE GPS MEASUREMENTS IN ALASKA

There are two ways in which optimal locations for future GPS measurements in Alaska can be determined. The first way is to investigate the large residuals in current studies

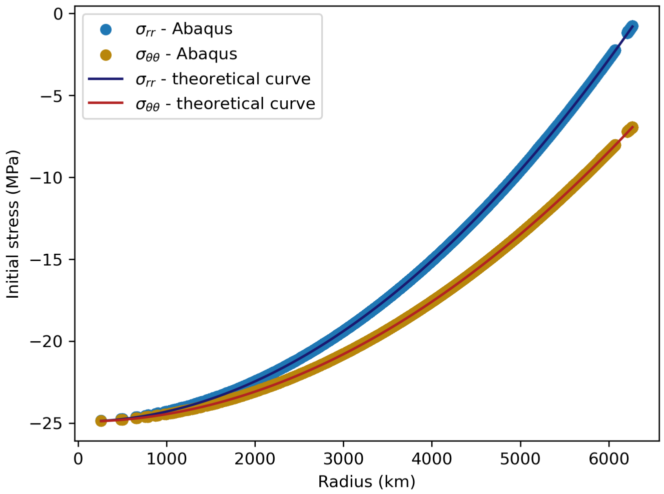

Figure 6.1: Theoretical stresses in a homogeneous elastic Earth, and those calculated by Abaqus after applying a radial body force.

comparing model results to GNSS observations in Alaska (e.g., *Elliott and Freymueller*, 2020; *Elliott et al.*, 2010). Even though *Elliott et al.* (2010) did not find a pattern in the residuals, the current models are not able to fit the observations in areas with significant residuals. It would be interesting to see if a pattern emerges in the residual velocities with a 3D GIA model. The second option is to study the sensitivity of tectonic block model velocities to the block geometry and the applied (3D) GIA model and identify areas that are very sensitive to choices herein. Areas that exhibit a large spread in modelled block velocities can be constrained using new GPS measurements in those areas. A similar analysis has been performed by *Wu et al.* (2010) for North America and Europe. In this study, future measurement locations are determined based on the criterium that the sensitivity of perturbations in ice model, lithosphere thickness, background viscosity and lateral viscosity variations is larger than the current accuracy of GPS measurements. Such analysis can also be performed specifically for Alaska by investigating the block model velocities while varying the Earth structure of the GIA model and the geometry of the block model.

REFERENCES

A, G., J. Wahr, and S. Zhong (2013), Computations of the viscoelastic response of a 3-D compressible Earth to surface loading: an application to Glacial Isostatic Adjustment in Antarctica and Canada, *Geophysical Journal International*, *192*(2), 557–572, doi:10.1093/gji/ggs030.

Afonso, J. C., F. Salajegheh, W. Szwillus, J. Ebbing, and C. Gaina (2019), A global reference model of the lithosphere and upper mantle from joint inversion and analysis of multiple data sets, *Geophysical Journal International*, *217*(3), 1602–1628.

Aiken, C., J. P. Zimmerman, Z. Peng, and J. I. Walter (2015), Triggered seismic events along the eastern denali fault in northwest canada following the 2012 mw 7.8 haida gwaii, 2013 mw 7.5 craig, and two mw> 8.5 teleseismic earthquakes, *Bulletin of the Seismological Society of America*, *105*(2B), 1165–1177.

Airy, G. B. (1855), Iii. on the computation of the effect of the attraction of mountain-masses, as disturbing the apparent astronomical latitude of stations in geodetic surveys, *Philosophical Transactions of the Royal Society of London*, (145), 101–104.

Amelung, F., and D. Wolf (1994), Viscoelastic perturbations of the earth: significance of the incremental gravitational force in models of glacial isostasy, *Geophysical Journal International*, *117*(3), 864–879.

Argus, D. F., W. Peltier, R. Drummond, and A. W. Moore (2014), The Antarctica component of postglacial rebound model ICE-6G_C (VM5a) based on GPS positioning, exposure age dating of ice thicknesses, and relative sea level histories, *Geophysical Journal International*, *198*(1), 537–563.

Árnadóttir, T., B. Lund, W. Jiang, H. Geirsson, H. Björnsson, P. Einarsson, and T. Sigurdsson (2009), Glacial rebound and plate spreading: results from the first countrywide GPS observations in Iceland, *Geophysical Journal International*, *177*(2), 691–716.

Auer, L., L. Boschi, T. Becker, T. Nissen-Meyer, and D. Giardini (2014), Savani: A variable resolution whole-mantle model of anisotropic shear velocity variations based on multiple data sets, *Journal of Geophysical Research: Solid Earth*, *119*(4), 3006–3034.

Auriac, A., K. Spaans, F. Sigmundsson, A. Hooper, P. Schmidt, and B. Lund (2013), Iceland rising: Solid Earth response to ice retreat inferred from satellite radar interferometry and visocelastic modeling, *Journal of Geophysical Research: Solid Earth*, *118*(4), 1331–1344.

Backus, G. E. (1967), Converting vector and tensor equations to scalar equations in spherical coordinates, *Geophysical Journal International*, *13*(1-3), 71–101.

Bagge, M., V. Klemann, B. Steinberger, M. Latinović, and M. Thomas (2021), Glacial-isostatic adjustment models using geodynamically constrained 3d earth structures, *Geochemistry, Geophysics, Geosystems*, *22*(11), e2021GC009,853.

Bängtsson, E., and B. Lund (2008), A comparison between two solution techniques to solve the equations of glacially induced deformation of an elastic Earth, *International journal for numerical methods in engineering*, *75*(4), 479–502.

Barnhoorn, A., W. Van der Wal, and M. R. Drury (2011), Upper mantle viscosity and lithospheric thickness under iceland, *Journal of Geodynamics*, *52*(3-4), 260–270.

Becker, T. W., and L. Boschi (2002), A comparison of tomographic and geodynamic mantle models, *Geochemistry, Geophysics, Geosystems*, *3*(1).

Berthier, E., E. Schiefer, G. K. Clarke, B. Menounos, and F. Rémy (2010), Contribution of alaskan glaciers to sea-level rise derived from satellite imagery, *Nature Geoscience*, *3*(2), 92–95.

Blank, B., V. Barletta, H. Hu, F. Pappa, and W. van der Wal (2021), Effect of lateral and stress-dependent viscosity variations on gia induced uplift rates in the amundsen sea embayment, *Geochemistry, Geophysics, Geosystems*, *22*(9), e2021GC009,807.

Bower, D. J., M. Gurnis, and M. Seton (2013), Lower mantle structure from paleogeographically constrained dynamic earth models, *Geochemistry, Geophysics, Geosystems*, *14*(1), 44–63.

Čadek, O., and L. Fleitout (2003), Effect of lateral viscosity variations in the top 300 km on the geoid and dynamic topography, *Geophysical Journal International*, *152*(3), 566–580.

Cammarano, F., S. Goes, P. Vacher, and D. Giardini (2003), Inferring upper-mantle temperatures from seismic velocities, *Physics of the Earth and Planetary Interiors*, *138*(3-4), 197–222.

Caron, L., L. Métivier, M. Greff-Lefftz, L. Fleitout, and H. Rouby (2017), Inverting Glacial Isostatic Adjustment signal using Bayesian framework and two linearly relaxing rheologies, *Geophysical Journal International*, *209*(2), 1126–1147.

Cathles, L. (1975), The viscosity of the earth's mantle princeton university press, *New Jersey*, *390*.

Christeson, G. L., S. P. Gulick, H. J. van Avendonk, L. L. Worthington, R. S. Reece, and T. L. Pavlis (2010), The yakutat terrane: Dramatic change in crustal thickness across the transition fault, alaska, *Geology*, *38*(10), 895–898.

Cianetti, S., C. Giunchi, and G. Spada (2002), Mantle viscosity beneath the Hudson Bay: an inversion based on the Metropolis algorithm, *Journal of Geophysical Research: Solid Earth*, *107*(B12), ETG–12.

Čížková, H., A. P. van den Berg, W. Spakman, and C. Matyska (2012), The viscosity of earth's lower mantle inferred from sinking speed of subducted lithosphere, *Physics of the earth and Planetary Interiors*, *200*, 56–62.

Ding, K., J. T. Freymueller, Q. Wang, and R. Zou (2015), Coseismic and early postseismic deformation of the 5 january 2013 m w 7.5 craig earthquake from static and kinematic gps solutions, *Bulletin of the Seismological Society of America*, *105*(2B), 1153–1164.

Dixon, J. E., T. H. Dixon, D. Bell, and R. Malservisi (2004), Lateral variation in upper mantle viscosity: role of water, *Earth and Planetary Science Letters*, *222*(2), 451–467.

Doser, D. I., and R. Lomas (2000), The transition from strike–slip to oblique subduction in southeastern alaska from seismological studies, *Tectonophysics*, *316*(1-2), 45–65.

Drinkwater, M., R. Floberghagen, R. Haagmans, D. Muzi, and A. Popescu (2003), Vii: Closing session: Goce: Esa's first earth explorer core mission, *Space science reviews*, *108*(1-2), 419–432.

Dziewonski, A. M., and D. L. Anderson (1981), Preliminary reference Earth model, *Physics of the earth and planetary interiors*, *25*(4), 297–356.

Eaton, D. W., and F. Darbyshire (2010), Lithospheric architecture and tectonic evolution of the hudson bay region, *Tectonophysics*, *480*(1-4), 1–22.

Eaton, D. W., F. Darbyshire, R. L. Evans, H. Grütter, A. G. Jones, and X. Yuan (2009), The elusive lithosphere–asthenosphere boundary (lab) beneath cratons, *Lithos*, *109*(1-2), 1–22.

Ekström, G. (2017), Short-period surface-wave phase velocities across the conterminous united states, *Physics of the Earth and Planetary Interiors*, *270*, 168–175.

Elliott, J., and J. T. Freymueller (2020), A block model of present-day kinematics of alaska and western canada, *Journal of Geophysical Research: Solid Earth*, *125*(7), e2019JB018,378.

Elliott, J. L., C. F. Larsen, J. T. Freymueller, and R. J. Motyka (2010), Tectonic block motion and glacial isostatic adjustment in southeast alaska and adjacent canada constrained by gps measurements, *Journal of Geophysical Research: Solid Earth*, *115*(B9).

Engelhart, S., W. R. Peltier, and B. Horton (2011), Holocene relative sea-level changes and glacial isostatic adjustment of the us atlantic coast, *Geology*, *39*(8), 751–754.

Farrell, W., and J. A. Clark (1976), On postglacial sea level, *Geophysical Journal International*, *46*(3), 647–667.

Fecher, T., R. Pail, and T. Gruber (2017), Goco05c: a new combined gravity field model based on full normal equations and regionally varying weighting, *Surveys in geophysics*, *38*(3), 571–590.

Fischer, K. M., H. A. Ford, D. L. Abt, and C. A. Rychert (2010), The lithosphere-asthenosphere boundary, *Annual Review of Earth and Planetary Sciences*, *38*, 551–575.

Flament, N., M. Gurnis, and R. D. Müller (2013), A review of observations and models of dynamic topography, *Lithosphere*, *5*(2), 189–210.

Fleming, K., Z. Martinec, and D. Wolf (2007), Glacial-isostatic adjustment and the viscosity structure underlying the Vatnajökull Ice Cap, Iceland, in *Deformation and Gravity Change: Indicators of Isostasy, Tectonics, Volcanism, and Climate Change*, pp. 751–768, Springer.

Forte, A., and J. X. Mitrovica (1996), New inferences of mantle viscosity from joint inversion of long-wavelength mantle convection and post-glacial rebound data, *Geophysical Research Letters*, *23*(10), 1147–1150.

Freed, A. M., B. C. Johnson, D. M. Blair, H. Melosh, G. A. Neumann, R. J. Phillips, S. C. Solomon, M. A. Wieczorek, and M. T. Zuber (2014), The formation of lunar mascon basins from impact to contemporary form, *Journal of Geophysical Research: Planets*, *119*(11), 2378–2397.

Freymueller, J. T., H. Woodard, S. C. Cohen, R. Cross, J. Elliott, C. F. Larsen, S. Hreinsdóttir, C. Zweck, P. Haeussler, R. Wesson, et al. (2008), Active deformation processes in alaska, based on 15 years of gps measurements, *Active tectonics and seismic potential of Alaska*, *179*, 1–42.

Fullea, J., S. Lebedev, Z. Martinec, and N. Celli (2021), Winterc-g: mapping the upper mantle thermochemical heterogeneity from coupled geophysical–petrological inversion of seismic waveforms, heat flow, surface elevation and gravity satellite data, *Geophysical Journal International*, *226*(1), 146–191.

Gasperini, P., D. A. Yuen, and R. Sabadini (1990), Effects of lateral viscosity variations on postglacial rebound: Implications for recent sea-level trends, *Geophysical Research Letters*, *17*(1), 5–8.

Ghosh, A., T. Becker, and S. Zhong (2010), Effects of lateral viscosity variations on the geoid, *Geophysical Research Letters*, *37*(1).

Goes, S., R. Govers, and P. Vacher (2000), Shallow mantle temperatures under europe from p and s wave tomography, *Journal of Geophysical Research: Solid Earth*, *105*(B5), 11,153–11,169.

Goodwin, R. G. (1988), Holocene glaciolacustrine sedimentation in muir inlet and ice advance in glacier bay, alaska, usa, *Arctic and Alpine Research*, *20*(1), 55–69.

Gowan, E. J., X. Zhang, S. Khosravi, A. Rovere, P. Stocchi, A. L. Hughes, R. Gyllencreutz, J. Mangerud, J.-I. Svendsen, and G. Lohmann (2021), A new global ice sheet reconstruction for the past 80 000 years, *Nature communications*, *12*(1), 1199.

Greff-Lefftz, M., and H. Legros (1997), Some remarks about the degree-one deformation of the earth, *Geophysical Journal International*, *131*(3), 699–723.

Gu, Y. J., A. M. Dziewonski, W. Su, and G. Ekström (2001), Models of the mantle shear velocity and discontinuities in the pattern of lateral heterogeneities, *Journal of Geophysical Research: Solid Earth*, *106*(B6), 11,169–11,199.

Gvirtzman, Z., C. Faccenna, and T. W. Becker (2016), Isostasy, flexure, and dynamic topography, *Tectonophysics*, *683*, 255–271.

Hager, B. H., R. W. Clayton, M. A. Richards, R. P. Comer, and A. M. Dziewonski (1985), Lower mantle heterogeneity, dynamic topography and the geoid, *Nature*, *313*(6003), 541.

Hampel, A., and R. Hetzel (2006), Response of normal faults to glacial-interglacial fluctuations of ice and water masses on Earth's surface, *Journal of Geophysical Research: Solid Earth*, *111*(B6).

Hampel, A., R. Hetzel, G. Maniatis, and T. Karow (2009), Three-dimensional numerical modeling of slip rate variations on normal and thrust fault arrays during ice cap growth and melting, *Journal of Geophysical Research: Solid Earth*, *114*(B8).

Hampel, A., J. Lüke, T. Krause, and R. Hetzel (2019), Finite-element modelling of glacial isostatic adjustment (GIA): Use of elastic foundations at material boundaries versus the geometrically non-linear formulation, *Computers & geosciences*, *122*, 1–14.

Hamza, V., and F. Vieira (2012), Global distribution of the lithosphere-asthenosphere boundary: a new look, *Solid Earth*, *3*(2), 199–212.

Hanyk, L., C. Matyska, and D. A. Yuen (1999), Secular gravitational instability of a compressible viscoelastic sphere, *Geophysical research letters*, *26*(5), 557–560.

Hermans, T., W. van der Wal, and T. Broerse (2018), Reversal of the direction of horizontal velocities induced by GIA as a function of mantle viscosity, *Geophysical Research Letters*, *45*(18), 9597–9604.

Hibbitt, D., B. Karlsson, and P. Sorensen (2016), Getting started with ABAQUS, version (6.14), *Hibbit, Karlsson & Sorensen, Inc.*

Hirth, G., and D. Kohlstedt (2003), Rheology of the upper mantle and the mantle wedge: A view from the experimentalists, *Geophysical monograph-american geophysical union*, *138*, 83–106.

Hu, Y., and J. T. Freymueller (2019), Geodetic observations of time-variable glacial isostatic adjustment in southeast alaska and its implications for earth rheology, *Journal of Geophysical Research: Solid Earth*, *124*(9), 9870–9889.

Huang, P., R. Steffen, H. Steffen, V. Klemann, P. Wu, W. van der Wal, Z. Martinec, and Y. Tanaka (2023), A commercial finite element approach to modelling glacial isostatic adjustment on spherical self-gravitating compressible earth models, *Geophysical Journal International*, *235*(3), 2231–2256.

Hüttl, R. F. (2011), Der blick aus dem all in das system erde, in *Ein Planet voller Überraschungen/Our Surprising Planet*, pp. 17–40, Springer.

Ivins, E., W. van der Wal, D. Wiens, A. Lloyd, and L. Caron (2023), Antarctic upper mantle rheology.

Ivins, E. R., and T. S. James (1999), Simple models for late Holocene and present-day Patagonian glacier fluctuations and predictions of a geodetically detectable isostatic response, *Geophysical Journal International*, *138*(3), 601–624.

Ivins, E. R., and C. G. Sammis (1995), On lateral viscosity contrast in the mantle and the rheology of low-frequency geodynamics, *Geophysical Journal International*, *123*(2), 305–322.

James, T. S. (1992), The hudson bay free-air gravity anomaly and glacial rebound, *Geophysical Research Letters*, *19*(9), 861–864.

James, T. S., and A. Lambert (1993), A comparison of VLBI data with the ICE-3G glacial rebound model, *Geophysical Research Letters*, *20*(9), 871–874.

James, T. S., and W. J. Morgan (1990), Horizontal motions due to post-glacial rebound, *Geophysical Research Letters*, *17*(7), 957–960.

Jiang, C., B. Schmandt, K. M. Ward, F.-C. Lin, and L. L. Worthington (2018), Upper mantle seismic structure of alaska from rayleigh and s wave tomography, *Geophysical Research Letters*, *45*(19), 10–350.

Johnston, P., K. Lambeck, and D. Wolf (1997), Material versus isobaric internal boundaries in the earth and their influence on postglacial rebound, *Geophysical Journal International*, *129*(2), 252–268.

Karato, S.-i. (1993), Importance of anelasticity in the interpretation of seismic tomography, *Geophysical Research Letters*, *20*(15), 1623–1626.

Karato, S.-i. (2008), Deformation of earth materials, *An Introduction to the Rheology of Solid Earth*, *463*.

Kaufmann, G. (2004), Program Package ICEAGE, Version 2004., Manuscript. Institut für Geophysik der Universität Göttingen.

Kaufmann, G., and K. Lambeck (2000), Mantle dynamics, postglacial rebound and the radial viscosity profile, *Physics of the Earth and Planetary Interiors*, *121*(3-4), 301–324.

Kaufmann, G., P. Wu, and E. R. Ivins (2005), Lateral viscosity variations beneath Antarctica and their implications on regional rebound motions and seismotectonics, *Journal of Geodynamics*, *39*(2), 165–181.

Kaula, W. M. (1972), Global gravity and tectonics, *The nature of the solid Earth*, pp. 385–405.

Kierulf, H. P., H. Steffen, V. R. Barletta, M. Lidberg, J. Johansson, O. Kristiansen, and L. Tarasov (2021), A gnss velocity field for geophysical applications in fennoscandia, *Journal of Geodynamics*, *146*, 101,845.

King, M. A., P. L. Whitehouse, and W. van der Wal (2016), Incomplete separability of antarctic plate rotation from glacial isostatic adjustment deformation within geodetic observations, *Geophysical Journal International*, *204*(1), 324–330.

King, S. D. (1995), Radial models of mantle viscosity: results from a genetic algorithm, *Geophysical Journal International*, *122*(3), 725–734.

Klemann, V., P. Wu, and D. Wolf (2003), Compressible viscoelasticity: stability of solutions for homogeneous plane-Earth models, *Geophysical Journal International*, *153*(3), 569–585.

Klemann, V., Z. Martinec, and E. R. Ivins (2008), Glacial isostasy and plate motion, *Journal of Geodynamics*, *46*(3-5), 95–103.

Koehler, R., R.-E. Farrell, P. Burns, and R. Combellick (2012), Quaternary faults and folds in alaska: A digital database, doi:https://doi.org/10.14509/24956.

Kreemer, C., W. C. Hammond, and G. Blewitt (2018), A robust estimation of the 3-D intraplate deformation of the North American plate from GPS, *Journal of Geophysical Research: Solid Earth*, *123*(5), 4388–4412.

Kuchar, J., G. Milne, and K. Latychev (2019), The importance of lateral earth structure for north american glacial isostatic adjustment, *Earth and Planetary Science Letters*, *512*, 236–245.

Lachenbruch, A. H., and P. Morgan (1990), Continental extension, magmatism and elevation; formal relations and rules of thumb, *Tectonophysics*, *174*(1-2), 39–62.

Lahr, J. C., and G. Plafker (1980), Holocene pacific–north american plate interaction in southern alaska: Implications for the yakataga seismic gap, *Geology*, *8*(10), 483–486.

Lahtinen, S., L. Jivall, P. Häkli, T. Kall, K. Kollo, K. Kosenko, K. Galinauskas, D. Prizginiene, O. Tangen, M. Weber, et al. (2019), Densification of the itrf2014 position and velocity solution in the nordic and baltic countries, *GPS solutions*, *23*, 1–13.

Lai, H., E. J. Garnero, S. P. Grand, R. W. Porritt, and T. W. Becker (2019), Global travel time data set from adaptive empirical wavelet construction, *Geochemistry, Geophysics, Geosystems*, *20*(5), 2175–2198.

Lambeck, K., H. Rouby, A. Purcell, Y. Sun, and M. Sambridge (2014), Sea level and global ice volumes from the Last Glacial Maximum to the Holocene, *Proceedings of the National Academy of Sciences*, *111*(43), 15,296–15,303.

Lambeck, K., A. Purcell, and S. Zhao (2017), The North American Late Wisconsin ice sheet and mantle viscosity from glacial rebound analyses, *Quaternary Science Reviews*, *158*, 172–210.

Landerer, F. W., F. M. Flechtner, H. Save, F. H. Webb, T. Bandikova, W. I. Bertiger, S. V. Bettadpur, S. H. Byun, C. Dahle, H. Dobslaw, et al. (2020), Extending the global mass change data record: Grace follow-on instrument and science data performance, *Geophysical Research Letters, 47*(12), e2020GL088,306.

Larsen, C. F., K. A. Echelmeyer, J. T. Freymueller, and R. J. Motyka (2003), Tide gauge records of uplift along the northern Pacific-North American plate boundary, 1937 to 2001, *Journal of Geophysical Research: Solid Earth, 108*(B4).

Larsen, C. F., R. J. Motyka, J. T. Freymueller, K. A. Echelmeyer, and E. R. Ivins (2004), Rapid uplift of southern Alaska caused by recent ice loss, *Geophysical Journal International, 158*(3), 1118–1133.

Larsen, C. F., R. J. Motyka, J. T. Freymueller, K. A. Echelmeyer, and E. R. Ivins (2005), Rapid viscoelastic uplift in southeast alaska caused by post-little ice age glacial retreat, *Earth and planetary Science letters, 237*(3-4), 548–560.

Laske, G., G. Masters, Z. Ma, and M. Pasyanos (2013), Update on CRUST1. 0—A 1-degree global model of Earth's crust, in *Geophys. Res. Abstr*, vol. 15, p. 2658, EGU General Assembly Vienna, Austria.

Latychev, K., J. X. Mitrovica, J. Tromp, M. E. Tamisiea, D. Komatitsch, and C. C. Christara (2005), Glacial isostatic adjustment on 3-D Earth models: a finite-volume formulation, *Geophysical Journal International, 161*(2), 421–444.

Lau, H. C., J. X. Mitrovica, J. Austermann, O. Crawford, D. Al-Attar, and K. Latychev (2016), Inferences of mantle viscosity based on ice age data sets: Radial structure, *Journal of Geophysical Research: Solid Earth, 121*(10), 6991–7012.

Lay, T., L. Ye, H. Kanamori, Y. Yamazaki, K. F. Cheung, K. Kwong, and K. D. Koper (2013), The october 28, 2012 mw 7.8 haida gwaii underthrusting earthquake and tsunami: Slip partitioning along the queen charlotte fault transpressional plate boundary, *Earth and Planetary Science Letters, 375*, 57–70.

Leonard, L. J., R. D. Hyndman, S. Mazzotti, L. Nykolaishen, M. Schmidt, and S. Hippchen (2007), Current deformation in the northern canadian cordillera inferred from gps measurements, *Journal of Geophysical Research: Solid Earth, 112*(B11).

Li, T., P. Wu, H. Steffen, and H. Wang (2018), In search of laterally heterogeneous viscosity models of glacial isostatic adjustment with the ice-6g_c global ice history model, *Geophysical Journal International, 214*(2), 1191–1205.

Li, T., P. Wu, H. Wang, H. Steffen, N. S. Khan, S. E. Engelhart, M. Vacchi, T. A. Shaw, W. R. Peltier, and B. P. Horton (2020), Uncertainties of glacial isostatic adjustment model predictions in north america associated with 3d structure, *Geophysical Research Letters, 47*(10), e2020GL087,944.

Liu, X., and S. Zhong (2016), Constraining mantle viscosity structure for a thermochemical mantle using the geoid observation, *Geochemistry, Geophysics, Geosystems, 17*(3), 895–913.

Love, A. E. H. (1927), *A treatise on the mathematical theory of elasticity (4^{th} edition)*, Cambridge university press.

Love, R., G. A. Milne, L. Tarasov, S. E. Engelhart, M. P. Hijma, K. Latychev, B. P. Horton, and T. E. Törnqvist (2016), The contribution of glacial isostatic adjustment to projections of sea-level change along the atlantic and gulf coasts of north america, *Earth's Future*, *4*(10), 440–464.

Lund, B., P. Schmidt, and C. Hieronymus (2009), Stress evolution and fault stability during the Weichselian glacial cycle.

Marsman, C. P., W. van der Wal, R. E. Riva, and J. T. Freymueller (2021), The Impact of a 3-D Earth Structure on Glacial Isostatic Adjustment in Southeast Alaska Following the Little Ice Age, *Journal of Geophysical Research: Solid Earth*, *126*(12), e2021JB022,312.

Martinec, Z. (2000), Spectral–finite element approach to three-dimensional viscoelastic relaxation in a spherical earth, *Geophysical Journal International*, *142*(1), 117–141.

Martinec, Z., V. Klemann, W. van der Wal, R. Riva, G. Spada, Y. Sun, D. Melini, S. Kachuck, V. Barletta, K. Simon, et al. (2018), A benchmark study of numerical implementations of the sea level equation in gia modelling, *Geophysical Journal International*, *215*(1), 389–414.

Mayer-Guerr, T. (2015), The combined satellite gravity field model goco05s, in *EGU general assembly conference abstracts*, p. 12364.

Mazzotti, S., R. D. Hyndman, P. Flück, A. J. Smith, and M. Schmidt (2003), Distribution of the pacific/north america motion in the queen charlotte islands-s. alaska plate boundary zone, *Geophysical Research Letters*, *30*(14).

Mercier, J.-P., M. Bostock, J. Cassidy, K. Dueker, J. Gaherty, E. Garnero, J. Revenaugh, and G. Zandt (2009), Body-wave tomography of western canada, *Tectonophysics*, *475*(3-4), 480–492.

Métivier, L., L. Caron, M. Greff-Lefftz, G. Pajot-Métivier, L. Fleitout, and H. Rouby (2016), Evidence for postglacial signatures in gravity gradients: A clue in lower mantle viscosity, *Earth and Planetary Science Letters*, *452*, 146–156.

Milne, G. A., and J. X. Mitrovica (1998), Postglacial sea-level change on a rotating earth, *Geophysical Journal International*, *133*(1), 1–19.

Mitrovica, J., and A. Forte (2004), A new inference of mantle viscosity based upon joint inversion of convection and glacial isostatic adjustment data, *Earth and Planetary Science Letters*, *225*(1-2), 177–189.

Mitrovica, J., and W. Peltier (1989), Pleistocene deglaciation and the global gravity field, *Journal of Geophysical Research: Solid Earth*, *94*(B10), 13,651–13,671.

Mitrovica, J., and W. Peltier (1991a), On postglacial geoid subsidence over the equatorial oceans, *Journal of Geophysical Research: Solid Earth*, *96*(B12), 20,053–20,071.

Mitrovica, J., and W. Peltier (1991b), Free air gravity anomalies associated with glacial isostatic disequilibriu: Load history effects on the inference of deep mantle viscosity, *Geophysical Research Letters*, *18*(2), 235–238.

Mitrovica, J., and W. Peltier (1991c), A complete formalism for the inversion of post-glacial rebound data: resolving power analysis, *Geophysical Journal International*, *104*(2), 267–288.

Mitrovica, J., J. Davis, and I. Shapiro (1994a), A spectral formalism for computing three-dimensional deformations due to surface loads: 2. Present-day glacial isostatic adjustment, *Journal of Geophysical Research: Solid Earth*, *99*(B4), 7075–7101.

Mitrovica, J., J. Davis, and I. Shapiro (1994b), A spectral formalism for computing three-dimensional deformations due to surface loads: 2. present-day glacial isostatic adjustment, *Journal of Geophysical Research: Solid Earth*, *99*(B4), 7075–7101.

Molnar, P., P. C. England, and C. H. Jones (2015), Mantle dynamics, isostasy, and the support of high terrain, *Journal of Geophysical Research: Solid Earth*, *120*(3), 1932–1957.

Monteith, D., C. Connor, G. Streveler, and W. Howell (2004), Geology and oral history—complementary views of a former glacier bay landscape, in *Proceedings of the Fourth Glacier Bay Science Symposium*, pp. 50–53.

Nakada, M., and J. Okuno (2016), Inference of mantle viscosity for depth resolutions of gia observations, *Geophysical Supplements to the Monthly Notices of the Royal Astronomical Society*, *207*(2), 719–740.

Nguyen, N., and A. M. Waas (2016), Nonlinear, finite deformation, finite element analysis, *Zeitschrift für angewandte Mathematik und Physik*, *67*(3), 1–24.

Nield, G. A., V. R. Barletta, A. Bordoni, M. A. King, P. L. Whitehouse, P. J. Clarke, E. Domack, T. A. Scambos, and E. Berthier (2014), Rapid bedrock uplift in the antarctic peninsula explained by viscoelastic response to recent ice unloading, *Earth and Planetary Science Letters*, *397*, 32–41.

Nield, G. A., P. L. Whitehouse, W. van der Wal, B. Blank, J. P. O'Donnell, and G. W. Stuart (2018), The impact of lateral variations in lithospheric thickness on glacial isostatic adjustment in West Antarctica, *Geophysical Journal International*, *214*(2), 811–824.

Nield, G. A., M. A. King, R. Steffen, and B. Blank (2022), A global, spherical finite-element model for post-seismic deformation using Abaqus, *Geoscientific Model Development*, *15*(6), 2489–2503.

O'Keefe, K., and P. Wu (2002), Effect of mantle structure on postglacial induced horizontal displacement, *Ice Sheets, Sea Level and the Dynamic Earth, Geodyn. Ser*, *29*, 109–118.

Pagli, C., F. Sigmundsson, B. Lund, E. Sturkell, H. Geirsson, P. Einarsson, T. Árnadóttir, and S. Hreinsdóttir (2007), Glacio-isostatic deformation around the Vatnajökull ice cap, Iceland, induced by recent climate warming: GPS observations and finite element modeling, *Journal of Geophysical Research: Solid Earth*, *112*(B8).

Pail, R., T. Fecher, D. Barnes, J. Factor, S. Holmes, T. Gruber, and P. Zingerle (2018), Short note: the experimental geopotential model XGM2016, *Journal of Geodesy*, *92*(4), 443–451.

Paulson, A., S. Zhong, and J. Wahr (2005), Modelling post-glacial rebound with lateral viscosity variations, *Geophysical Journal International*, *163*(1), 357–371.

Paulson, A., S. Zhong, and J. Wahr (2007), Inference of mantle viscosity from GRACE and relative sea level data, *Geophysical Journal International*, *171*(2), 497–508.

Peltier, W. (1974), The impulse response of a Maxwell Earth, *Reviews of Geophysics*, *12*(4), 649–669.

Peltier, W. (1998), A space geodetic target for mantle viscosity discrimination: Horizontal motions induced by glacial isostatic adjustment, *Geophysical research letters*, *25*(4), 543–546.

Peltier, W., and R. Drummond (2008), Rheological stratification of the lithosphere: A direct inference based upon the geodetically observed pattern of the glacial isostatic adjustment of the north american continent, *Geophysical Research Letters*, *35*(16).

Peltier, W., A. Forte, J. Mitrovica, and A. Dziewonski (1992), Earth's gravitational field: seismic tomography resolves the enigma of the laurentian anomaly, *Geophysical Research Letters*.

Peltier, W. R., D. Argus, and R. Drummond (2015), Space geodesy constrains ice age terminal deglaciation: The global ice-6g_c (vm5a) model, *Journal of Geophysical Research: Solid Earth*, *120*(1), 450–487.

Perry, H., A. Forte, and D. Eaton (2003), Upper-mantle thermochemical structure below north america from seismic–geodynamic flow models, *Geophysical Journal International*, *154*(2), 279–299.

Pfeffer, W. T., A. A. Arendt, A. Bliss, T. Bolch, J. G. Cogley, A. S. Gardner, J.-O. Hagen, R. Hock, G. Kaser, C. Kienholz, et al. (2014), The Randolph Glacier Inventory: a globally complete inventory of glaciers, *Journal of glaciology*, *60*(221), 537–552.

Plag, H.-P., and H.-U. Jüttner (1995), Rayleigh-Taylor instabilities of a self-gravitating Earth, *Journal of geodynamics*, *20*(3), 267–288.

Pollitz, F. F. (1997), Gravitational viscoelastic postseismic relaxation on a layered spherical Earth, *Journal of Geophysical Research: Solid Earth*, *102*(B8), 17,921–17,941.

Porritt, R. W., T. W. Becker, L. Boschi, and L. Auer (2021), Multiscale, radially anisotropic shear wave imaging of the mantle underneath the contiguous united states through joint inversion of usarray and global data sets, *Geophysical Journal International*, *226*(3), 1730–1746.

Pratt, J. H. (1859), Xxix. on the deflection of the plumb-line in india, caused by the attraction of the himmalaya mountains and of the elevated regions beyond; and its modification by the compensating effect of a deficiency of matter below the mountain mass, *Philosophical Transactions of the Royal Society of London*, (149), 745–778.

Purcell, A. (1998), The significance of pre-stress advection and internal buoyancy in the flat-Earth formulation, *Dynamics of the ice age earth: a modern perspective*, pp. 105–122.

Reigber, C., H. Lühr, and P. Schwintzer (2002), Champ mission status, *Advances in space research*, *30*(2), 129–134.

Reusen, J., R. Steffen, H. Steffen, B. Root, and W. van der Wal (2023), Simulating horizontal crustal motions of glacial isostatic adjustment using compressible cartesian models, *Geophysical Journal International*, *235*(1), 542–553.

Ritsema, J., a. A. Deuss, H. Van Heijst, and J. Woodhouse (2011), S40RTS: a degree-40 shear-velocity model for the mantle from new Rayleigh wave dispersion, teleseismic traveltime and normal-mode splitting function measurements, *Geophysical Journal International*, *184*(3), 1223–1236.

Riva, R., and L. Vermeersen (2002), Approximation method for high-degree harmonics in normal mode modelling, *Geophysical Journal International*, *151*(1), 309–313.

Robin, C., M. Craymer, R. Ferland, T. James, E. Lapelle, M. Piraszewski, and Y. Zhao (2020), *NAD83v70VG: a new national crustal velocity model for Canada*, Natural Resources Canada= Ressources naturelles Canada.

Root, B., W. van der Wal, P. Novák, J. Ebbing, and L. Vermeersen (2015), Glacial isostatic adjustment in the static gravity field of fennoscandia, *Journal of Geophysical Research: Solid Earth*, *120*(1), 503–518.

Root, B., P. Novák, D. Dirkx, M. Kaban, W. van der Wal, and L. Vermeersen (2016), On a spectral method for forward gravity field modelling, *Journal of Geodynamics*, *97*, 22–30.

Root, B., J. Ebbing, W. van der Wal, R. England, and L. Vermeersen (2017), Comparing gravity-based to seismic-derived lithosphere densities: a case study of the british isles and surrounding areas, *Geophysical Journal International*, *208*(3), 1796–1810.

Roy, K., and W. Peltier (2015), Glacial isostatic adjustment, relative sea level history and mantle viscosity: reconciling relative sea level model predictions for the us east coast with geological constraints, *Geophysical Journal International*, *201*(2), 1156–1181.

Roy, K., and W. Peltier (2017), Space-geodetic and water level gauge constraints on continental uplift and tilting over north america: regional convergence of the ice-6g_c (vm5a/vm6) models, *Geophysical Journal International*, *210*(2), 1115–1142.

Rudolph, M. L., V. Lekić, and C. Lithgow-Bertelloni (2015), Viscosity jump in earth's mid-mantle, *Science*, *350*(6266), 1349–1352.

Sabadini, R., B. Vermeersen, and G. Cambiotti (2016), *Global dynamics of the Earth*, Springer.

Samrat, N. H., M. A. King, C. Watson, A. Hooper, X. Chen, V. R. Barletta, and A. Bordoni (2020), Reduced ice mass loss and three-dimensional viscoelastic deformation in northern Antarctic Peninsula inferred from GPS, *Geophysical Journal International*, *222*(2), 1013–1022.

Sasgen, I., V. Klemann, and Z. Martinec (2012), Towards the inversion of GRACE gravity fields for present-day ice-mass changes and glacial-isostatic adjustment in North America and Greenland, *Journal of Geodynamics*, *59*, 49–63.

Sato, T., C. F. Larsen, S. Miura, Y. Ohta, H. Fujimoto, W. Sun, R. J. Motyka, and J. T. Freymueller (2011), Reevaluation of the viscoelastic and elastic responses to the past and present-day ice changes in Southeast Alaska, *Tectonophysics*, *511*(3-4), 79–88.

Schaeffer, A., and S. Lebedev (2013), Global shear speed structure of the upper mantle and transition zone, *Geophysical Journal International*, *194*(1), 417–449.

Schetselaar, E., and D. Snyder (2017), National database of MOHO depth estimates from seismic refraction and teleseismic surveys, *Geological Survey of Canada*, *Open File 8243*(1 .zip file), doi:https://doi.org/10.4095/305396.

Schmidt, P., B. Lund, and C. Hieronymus (2012a), Implementation of the glacial rebound prestress advection correction in general-purpose finite element analysis software: Springs versus foundations, *Computers & Geosciences*, *40*, 97–106.

Schmidt, P., B. Lund, T. Arnadottir, and H. Schmeling (2012b), Glacial isostatic adjustment constrains dehydration stiffening beneath iceland, *Earth and Planetary Science Letters*, *359*, 152–161.

Schotman, H., P. Wu, and L. Vermeersen (2008), Regional perturbations in a global background model of glacial isostasy, *Physics of the Earth and Planetary Interiors*, *171*(1-4), 323–335.

Schotman, H. H. A. (2008), Shallow-earth rheology from glacial isostasy and satellite gravity: a sensitivity analysis for goce, Ph.D. thesis, Delft University of Technology.

Sella, G. F., S. Stein, T. H. Dixon, M. Craymer, T. S. James, S. Mazzotti, and R. K. Dokka (2007), Observation of glacial isostatic adjustment in “stable” north america with gps, *Geophysical Research Letters*, *34*(2).

Sigloch, K. (2011), Mantle provinces under north america from multifrequency p wave tomography, *Geochemistry, Geophysics, Geosystems*, *12*(2).

Simmons, N. A., A. M. Forte, L. Boschi, and S. P. Grand (2010), GyPSuM: A joint tomographic model of mantle density and seismic wave speeds, *Journal of Geophysical Research: Solid Earth*, *115*(B12).

Simon, K., T. James, J. Henton, and A. Dyke (2016), A glacial isostatic adjustment model for the central and northern laurentide ice sheet based on relative sea level and gps measurements, *Geophysical Journal International*, *205*(3), 1618–1636.

Simons, M., and B. H. Hager (1997), Localization of the gravity field and the signature of glacial rebound, *Nature*, *390*(6659), 500–504.

Sleep, N. H. (2005), Evolution of the continental lithosphere, *Annu. Rev. Earth Planet. Sci.*, *33*, 369–393.

Soldati, G., L. Boschi, F. Deschamps, and D. Giardini (2009), Inferring radial models of mantle viscosity from gravity (GRACE) data and an evolutionary algorithm, *Physics of the Earth and Planetary Interiors*, *176*(1-2), 19–32.

Spada, G. (2003), The theory behind TABOO.

Spada, G., R. Sabadini, D. A. Yuen, and Y. Ricard (1992), Effects on post-glacial rebound from the hard rheology in the transition zone, *Geophysical Journal International*, *109*(3), 683–700.

Spada, G., V. R. Barletta, V. Klemann, R. Riva, Z. Martinec, P. Gasperini, B. Lund, D. Wolf, L. Vermeersen, and M. King (2011), A benchmark study for glacial isostatic adjustment codes, *Geophysical Journal International*, *185*(1), 106–132.

Steffen, H., G. Kaufmann, and P. Wu (2006), Three-dimensional finite-element modeling of the glacial isostatic adjustment in Fennoscandia, *Earth and Planetary Science Letters*, *250*(1-2), 358–375.

Steffen, H., J. Müller, and H. Denker (2009), Analysis of mass variations in northern glacial rebound areas from GRACE data, in *Observing Our Changing Earth*, pp. 501–509, Springer.

Steinberger, B. (2007), Effects of latent heat release at phase boundaries on flow in the Earth's mantle, phase boundary topography and dynamic topography at the Earth's surface, *Physics of the Earth and Planetary Interiors*, *164*(1-2), 2–20.

Steinberger, B., and T. W. Becker (2018), A comparison of lithospheric thickness models, *Tectonophysics*, *746*, 325–338.

Steinberger, B., and A. R. Calderwood (2006), Models of large-scale viscous flow in the earth's mantle with constraints from mineral physics and surface observations, *Geophysical Journal International*, *167*(3), 1461–1481.

Steinberger, B., C. P. Conrad, A. O. Tutu, and M. J. Hoggard (2019), On the amplitude of dynamic topography at spherical harmonic degree two, *Tectonophysics*, *760*, 221–228.

Stokes, C. R. (2017), Deglaciation of the laurentide ice sheet from the last glacial maximum, *Cuadernos de investigación geográfica*, *43*(2).

Su, W.-j., and A. M. Dziewonski (1991), Predominance of long-wavelength heterogeneity in the mantle, *Nature*, *352*(6331), 121–126.

Szwillus, W., J. C. Afonso, J. Ebbing, and W. D. Mooney (2019), Global crustal thickness and velocity structure from geostatistical analysis of seismic data, *Journal of Geophysical Research: Solid Earth*, *124*(2), 1626–1652.

Tamisiea, M., J. Mitrovica, and J. Davis (2007), Grace gravity data constrain ancient ice geometries and continental dynamics over laurentia, *Science*, *316*(5826), 881–883.

Tanaka, Y., V. Klemann, Z. Martinec, and R. Riva (2011), Spectral-finite element approach to viscoelastic relaxation in a spherical compressible Earth: application to GIA modelling, *Geophysical Journal International*, *184*(1), 220–234.

Tapley, B. D., S. Bettadpur, M. Watkins, and C. Reigber (2004), The gravity recovery and climate experiment: Mission overview and early results, *Geophysical research letters*, *31*(9).

Tarasov, L., A. S. Dyke, R. M. Neal, and W. R. Peltier (2012), A data-calibrated distribution of deglacial chronologies for the North American ice complex from glaciological modeling, *Earth and Planetary Science Letters*, *315*, 30–40.

Tosi, N. (2008), Numerical modeling of present-day mantle convection, Ph.D. thesis, Univerzita Karlova, Matematicko-fyzikální fakulta.

Trampert, J., F. Deschamps, J. Resovsky, and D. Yuen (2004), Probabilistic tomography maps chemical heterogeneities throughout the lower mantle, *Science*, *306*(5697), 853–856.

Trüssel, B. L., R. J. Motyka, M. Truffer, and C. F. Larsen (2013), Rapid thinning of lake-calving yakutat glacier and the collapse of the yakutat icefield, southeast alaska, usa, *Journal of Glaciology*, *59*(213), 149–161.

Turcotte, D. L., and G. Schubert (2002), *Geodynamics*, Cambridge university press.

Turner, R. J., A. M. Reading, and M. A. King (2020), Separation of tectonic and local components of horizontal gps station velocities: a case study for glacial isostatic adjustment in east antarctica, *Geophysical Journal International*, *222*(3), 1555–1569.

Turpeinen, H., A. Hampel, T. Karow, and G. Maniatis (2008), Effect of ice sheet growth and melting on the slip evolution of thrust faults, *Earth and Planetary Science Letters*, *269*(1-2), 230–241.

Van Calcar, C. J., R. S. Van De Wal, B. Blank, B. De Boer, and W. Van Der Wal (2023), Simulation of a fully coupled 3d glacial isostatic adjustment–ice sheet model for the antarctic ice sheet over a glacial cycle, *Geoscientific Model Development*, *16*(18), 5473–5492.

Van der Meer, D. G., D. J. Van Hinsbergen, and W. Spakman (2018), Atlas of the underworld: Slab remnants in the mantle, their sinking history, and a new outlook on lower mantle viscosity, *Tectonophysics*, *723*, 309–448.

Van der Wal, W., H. Schotman, and L. Vermeersen (2004), Geoid heights due to a crustal low viscosity zone in glacial isostatic adjustment modeling: A sensitivity analysis for goce, *Geophysical Research Letters, 31*(5).

van der Wal, W., P. Wu, M. G. Sideris, and C. Shum (2008), Use of GRACE determined secular gravity rates for glacial isostatic adjustment studies in North-America, *Journal of Geodynamics, 46*(3-5), 144–154.

van der Wal, W., A. Braun, P. Wu, and M. G. Sideris (2009), Prediction of decadal slope changes in Canada by glacial isostatic adjustment modelling, *Canadian Journal of Earth Sciences, 46*(8), 587–595.

van der Wal, W., P. Wu, H. Wang, and M. G. Sideris (2010), Sea levels and uplift rate from composite rheology in glacial isostatic adjustment modeling, *Journal of Geodynamics, 50*(1), 38–48.

van der Wal, W., A. Barnhoorn, P. Stocchi, S. Gradmann, P. Wu, M. Drury, and B. Vermeersen (2013), Glacial isostatic adjustment model with composite 3-d earth rheology for fennoscandia, *Geophysical Journal International, 194*(1), 61–77.

van der Wal, W., P. L. Whitehouse, and E. J. Schrama (2015), Effect of gia models with 3d composite mantle viscosity on grace mass balance estimates for antarctica, *Earth and Planetary Science Letters, 414*, 134–143.

Vardić, K., P. J. Clarke, and P. L. Whitehouse (2022), A gnss velocity field for crustal deformation studies: The influence of glacial isostatic adjustment on plate motion models, *Geophysical Journal International, 231*(1), 426–458.

Vermeersen, L., and J. Mitrovica (2000), Gravitational stability of spherical self-gravitating relaxation models, *Geophysical Journal International, 142*(2), 351–360.

Vermeersen, L., and R. Sabadini (1997), A new class of stratified viscoelastic models by analytical techniques, *Geophysical Journal International, 129*(3), 531–570.

Walcott, R. (1970), Isostatic response to loading of the crust in canada, *Canadian Journal of Earth Sciences, 7*(2), 716–727.

Walcott, R. I. (1973), Structure of the earth from glacio-isostatic rebound, *Annual Review of Earth and Planetary Sciences, 1*(1), 15–37.

Watts, A. B. (2001), *Isostasy and Flexure of the Lithosphere*, Cambridge University Press.

Watts, A. B., and J. D. P. Moore (2017), Flexural isostasy: Constraints from gravity and topography power spectra, *Journal of Geophysical Research: Solid Earth, 122*(10), 8417–8430.

Whitehouse, P., G. Milne, and K. Lambeck (2021), Glacial isostatic adjustment, in *Glaciers and Ice Sheets in the Climate System*, pp. 383–413, Springer.

Wieczorek, M. A., and M. Meschede (2018), Shtools: Tools for working with spherical harmonics, *Geochemistry, Geophysics, Geosystems, 19*(8), 2574–2592.

Wiles, G. C., D. J. Barclay, and P. E. Calkin (1999), Tree-ring-dated 'little ice age'histories of maritime glaciers from western prince william sound, alaska, *The Holocene*, *9*(2), 163–173.

Wolf, D., V. Klemann, J. Wünsch, and F.-p. Zhang (2006), A reanalysis and reinterpretation of geodetic and geological evidence of glacial-isostatic adjustment in the Churchill region, Hudson Bay, *Surveys in Geophysics*, *27*(1), 19–61.

Wolf, D., et al. (1985), The normal modes of a uniform, compressible Maxwell half-space, *Journal of Geophysics*, *56*(1), 100–105.

Wolstencroft, M., M. A. King, P. L. Whitehouse, M. J. Bentley, G. A. Nield, E. C. King, M. McMillan, A. Shepherd, V. Barletta, A. Bordoni, et al. (2015), Uplift rates from a new high-density gps network in palmer land indicate significant late holocene ice loss in the southwestern weddell sea, *Geophysical Journal International*, *203*(1), 737–754.

Wong, M. C., and P. Wu (2019), Using commercial finite-element packages for the study of Glacial Isostatic Adjustment on a compressible self-gravitating spherical earth–1: harmonic loads, *Geophysical Journal International*, *217*(3), 1798–1820.

Worthington, L. L., H. J. Van Avendonk, S. P. Gulick, G. L. Christeson, and T. L. Pavlis (2012), Crustal structure of the yakutat terrane and the evolution of subduction and collision in southern alaska, *Journal of Geophysical Research: Solid Earth*, *117*(B1).

Wu, P. (1992), Viscoelastic versus viscous deformation and the advection of pre-stress, *Geophysical journal international*, *108*(1), 136–142.

Wu, P. (2004), Using commercial finite element packages for the study of earth deformations, sea levels and the state of stress, *Geophysical Journal International*, *158*(2), 401–408.

Wu, P. (2006), Sensitivity of relative sea levels and crustal velocities in laurentide to radial and lateral viscosity variations in the mantle, *Geophysical Journal International*, *165*(2), 401–413.

Wu, P., and P. Johnston (1998), Validity of using flat-earth finite element models in the study of postglacial rebound, *Dynamics of the ice age earth: A modern perspective*, pp. 191–202.

Wu, P., and W. Peltier (1982), Viscous gravitational relaxation, *Geophysical Journal International*, *70*(2), 435–485.

Wu, P., and W. Peltier (1983), Glacial isostatic adjustment and the free air gravity anomaly as a constraint on deep mantle viscosity, *Geophysical Journal International*, *74*(2), 377–449.

Wu, P., and W. Peltier (1984), Pleistocene deglaciation and the earth's rotation: a new analysis, *Geophysical Journal International*, *76*(3), 753–791.

Wu, P., and W. van der Wal (2003), Postglacial sealevels on a spherical, self-gravitating viscoelastic earth: effects of lateral viscosity variations in the upper mantle on the inference of viscosity contrasts in the lower mantle, *Earth and Planetary Science Letters*, *211*(1-2), 57–68.

Wu, P., and H. Wang (2008), Postglacial isostatic adjustment in a self-gravitating spherical earth with power-law rheology, *Journal of Geodynamics*, *46*(3-5), 118–130.

Wu, P., H. Steffen, and H. Wang (2010), Optimal locations for gps measurements in north america and northern europe for constraining glacial isostatic adjustment, *Geophysical Journal International*, *181*(2), 653–664.

Wu, P., H. Wang, and H. Steffen (2013), The role of thermal effect on mantle seismic anomalies under laurentia and fennoscandia from observations of glacial isostatic adjustment, *Geophysical Journal International*, *192*(1), 7–17.

Yoffe, E. (1996), Stress in a gravitating sphere, *Philosophical Magazine A*, *73*(5), 1347–1353.

Yousefi, M., G. A. Milne, R. Love, and L. Tarasov (2018), Glacial isostatic adjustment along the pacific coast of central north america, *Quaternary Science Reviews*, *193*, 288–311.

Yousefi, M., G. A. Milne, and K. Latychev (2021), Glacial isostatic adjustment of the pacific coast of north america: The influence of lateral earth structure, *Geophysical Journal International*, *226*(1), 91–113.

Zhao, S. (2013), Lithosphere thickness and mantle viscosity estimated from joint inversion of GPS and GRACE-derived radial deformation and gravity rates in North America, *Geophysical Journal International*, *194*(3), 1455–1472.

Zhong, S., A. Paulson, and J. Wahr (2003), Three-dimensional finite-element modelling of Earth's viscoelastic deformation: effects of lateral variations in lithospheric thickness, *Geophysical Journal International*, *155*(2), 679–695.

Zwinger, T., G. A. Nield, J. Ruokolainen, and M. A. King (2020), A new open-source viscoelastic solid earth deformation module implemented in Elmer (v8. 4), *Geoscientific Model Development*, *13*(3), 1155–1164.

ACKNOWLEDGEMENTS

More than 7 years ago, on November 1, 2018, I started my PhD. On March 12, 2020, I was presenting at the NAC conference when it was announced that meetings with more than 100 people were not allowed anymore. I could finish my presentation, but it was a very surreal experience. After that, the world went into lockdown which marked the start of a second distinct PhD experience for me. Eventually, I reached the end of the PhD trajectory thanks to many people, listed below.

First of all, thanks to Bert, Wouter and Bart, for gathering the funding for this project [ESA Support to Science Program (3D Earth), NWO User Support for Space Program], and allowing me to start (and end) the PhD project. Bert, I will always remember you as a very kind person who really values the work of the PhD students of the department. In the final stages of the PhD you were very quick in responding to emails and took care of a large portion of the organisational part, thanks for that. Wouter and Bart, I am super happy that I got to discover GIA models with you as my supervisors. Bart, your enthousiasm and positivity about the gravity field, modelling, and research in general really shines through. I am happy to have been able to build upon your crustal density model for the gravity field. And Wouter, thanks for being super supportive throughout the whole process. In moments when I was completely lost, you helped me put things into perspective.

The first 3D Earth meeting I went to was in Dublin in March 2019, and I remember feeling very overwhelmed by all the state-of-the-art research that was being done. However, these days also showed me that professors are also ’just’ people who enjoy a good beer at the end of the day. Even though I was super tired when returning back in NL, I really treasure this experience.

I would also like to thank the other co-authors for their contribution to this thesis: Rebekka, Holger, Javier, and Wolfgang. A special thanks to Rebekka and Holger for their hospitality during my visit to Landmateriet in Gävle (Sweden). I found both of you very kind and understanding. Pingping, thanks for all the useful discussions on implementing compressibility in spherical GIA models. Lev, thanks for sending me the GLAC ice models back in 2019 or 2020. And Jeff, Julie, and Celine, thank you for your help on the Alaska chapter. Celine, it was very nice to already have a GIA model of the area to which I could compare my results. Julie, I am super happy that you were able to run the blocks models with the "more advanced" GIA models.

The many fellow PhD’s of the department during my time as a PhD also deserve a mention, so I’ll try to list them here at the risk of missing one or two: Marc, Bas, Teresa, Gourav, Yuxin, Mao, Tim, Günther, Kartik, Sam (Marie), Caroline, Tara, Rania, Livio, Natalia, Elina, and Vivian. Thanks for sharing your own PhD struggles and listening to mine. You guys are the reason why I have never felt alone in this whole process. I want to especially thank the PhD's that were present in our room 9.03 when I started. Marc, it was an absolute honour to have shared the same room as you. I absolutely loved our football discussions, but also the day-to-day life stories. Teresa, thank you for your kindness. In your eyes, I may always be a "young PhD" even when I have completed it. It made me feel like I still had time to finish stuff, which is a great feeling to have in this busy and stressful world. And Bas, thanks for showing me that, even when things do not go as planned, with enough perseverance you will eventually reach the end. Maybe you did not realise it at the time, but it also gave me the courage to continue when things did not go according to schedule. I would also like to highlight Gourav here, who was not in room 9.03. We had great talks on the ninth floor, and I am happy to say that we are still in touch even years after our PhD contracts ended.

My thanks also goes out to Nils for daring to be the first (and eventually only) master student that I supervised. Credit also goes out to Joanna and Weilun for letting me explain Abaqus to them while they were doing their master studies.

I am very grateful that I have been given the opportunity to start at Deltares and explore the fields of groundwater flows and subsurface systems. Even though both my PhD topic and projects at Deltares can be linked to isostasy, the scale is vastly different. Because of this, I had to learn many "basic" principles about groundwater flows and soil profiles from scratch. However, this challenges me to keep growing, both intellectually and as a person. Special thanks to Roel for allowing me to introduce myself to the company.

Friends of my calisthenics workout group (Bart, Yord and many others), thanks for being the perfect physical distraction for me. Nowadays, I consider our Monday workout sessions as a weekly catch-up, talking about life while also getting a good workout in.

Wouter, Thom en Kevin, ik geniet ontzettend van onze jaarlijkse reizen. Dat er na 10 jaren nog veel mogen volgen.

Ik voel mij erg bevoorrecht dat ik in zo'n fijn en stabiel huishouden heb mogen opgroeien. Bedankt, pap en mam, voor de eeuwige support. Ik kon en kan mijn verhalen altijd bij jullie kwijt en het voelt nog steeds als thuiskomen als ik bij jullie langs ga. Aan mijn schoonouders, bedankt voor alle gastvrijheid in het hoge noorden. Ik vind het altijd erg leuk en ontspannen om bij jullie langs te gaan.

Als laatste natuurlijk Irma, bij jou kan ik echt ontspannen en mijzelf zijn. Je hebt regelmatig mijn diepe zuchten en geklaag aan moeten horen tijdens de PhD en ziet wat elke actie met mij doet op persoonlijk vlak. Maar wat er ook gebeurt, wij vinden een oplossing en pakken het aan. Ik ben echt heel erg blij met jou, nog veel meer dan je je ooit voor zou kunnen stellen.

Odijk, October 2025
Jesse Reusen

CURRICULUM VITÆ

Jesse Milan REUSEN

01-02-1995	Born in Arnhem, the Netherlands

EDUCATION

2007-2013	Secondary Education Arentheem College Thomas a Kempis, Arnhem, the Netherlands
2013–2016	Bachelor of Science in Physics Utrecht University, Utrecht, the Netherlands *Thesis topic*: Simulating a glacier: application to Engabreen
2016–2018	Master of Science in Climate Physics Utrecht University, Utrecht, the Netherlands *Thesis topic*: Arctic Variability in Warm and Cold Climates
2018-2025	PhD Candidate - Astrodynamics and Space Missions Delft University of Technology, Delft, the Netherlands *Thesis topic*: Glacial Isostatic Adjustment in the static gravity field and horizontal motion

WORK EXPERIENCE

2024 - now	Junior Researcher/Advisor Subsurface & Groundwater Systems Deltares, Utrecht, the Netherlands

LIST OF PUBLICATIONS

JOURNAL ARTICLES

5. **Reusen, J. M.**, Steffen, R., Steffen, H., Root, B. C., & van der Wal, W. (2023). Simulating horizontal crustal motions of glacial isostatic adjustment using compressible Cartesian models. *Geophysical Journal International*, 235(1), 542-553.
4. Weerdesteijn, M. F., Naliboff, J. B., Conrad, C. P., **Reusen, J. M.**, Steffen, R., Heister, T., & Zhang, J. (2023). Modeling viscoelastic solid earth deformation due to ice age and contemporary glacial mass changes in ASPECT. *Geochemistry, Geophysics, Geosystems*, 24(3), e2022GC010813.
3. **Reusen, J. M.**, Root, B. C., Szwillus, W., Fullea, J., & van der Wal, W. (2020). Long-wavelength gravity field constraint on the lower mantle viscosity in North America. *Journal of Geophysical Research: Solid Earth*, 125(12), e2020JB020484.
2. Bintanja, R., van der Wiel, K., Van der Linden, E. C., **Reusen, J.**, Bogerd, L., Krikken, F., & Selten, F. M. (2020). Strong future increases in Arctic precipitation variability linked to poleward moisture transport. *Science advances*, 6(7), eaax6869.
1. **Reusen, J.**, van der Linden, E., & Bintanja, R. (2019). Differences between Arctic interannual and decadal variability across climate states. *Journal of Climate*, 32(18), 6035-6050.

SELECTED CONFERENCE CONTRIBUTIONS

6. **Reusen, J.**, Huang, P., Steffen, R., Steffen, H., van Calcar, C., Root, B., & van der Wal, W. (2022). The use of Non-Linear Geometry (NLGEOM) and gravity loading in flat and spherical Finite Element models of Abaqus for Glacial Isostatic Adjustment (GIA). *European Geophysical Union (EGU) General Assembly Conference Abstracts*, pp. EGU22-5146.
5. Huang, P., Steffen, R., Steffen, H., Klemann, V., van der Wal, W., **Reusen, J.**, ... & Thomas, M. (2022). A finite element approach to modelling Glacial Isostatic Adjustment on three-dimensional compressible earth models. *European Geophysical Union (EGU) General Assembly Conference Abstracts*, pp. EGU22-6013.
4. Weerdesteijn, M., Conrad, C., **Reusen, J.**, Steffen, R., & Naliboff, J. (2021). Solid Earth uplift due to contemporary ice melting above low-viscosity regions of Greenlands upper mantle. *American Geophysical Union (AGU) Fall Meeting Abstracts*, Vol. 2021, pp. G31A-05.
3. van der Wal, W., Fullea, J., **Reusen, J.**, & Ebbing, J. (2020). 3D Viscosity affects GIA-induced Uplift Rate Patterns in North America and Greenland. *American Geophysical Union (AGU) Fall Meeting Abstracts*, Vol. 2020, pp. G012-0010.
2. **Reusen, J.**, Root, B., Fullea, J., Martinec, Z., & van der Wal, W. (2020). Constraining dynamic models in North America using the static gravity field. *European Geophysical Union (EGU)*

General Assembly Conference Abstracts, p. 6964.

1. Bintanja, R., **Reusen, J.**, & van der Linden, E. (2019). The dependence of Arctic interannual and decadal variability on the state of the climate. *Geophysical Research Abstracts*, Vol. 21.

DATASETS

2. **Reusen, J. M.**, Steffen, R., Steffen, H., Root, B. C., & van der Wal, W. (2023). Supporting data for Simulating horizontal crustal motions of GIA using compressible cartesian models. *4TU.ResearchData, https://doi.org/10.4121/9a9bdb35-8f65-41f1-be00-4d247722ad48*
1. **Reusen, J. M.** (2020). Gravity North America - complete model and necessary codes. *4TU.ResearchData, https://doi.org/10.4121/uuid:54c182ea-3826-4200-83d6-414dad27b289*